Combustion of Reactive Metal Particles in High-Speed Flow of Detonation Products

by

Vincent Tanguay

Department of Mechanical Engineering
McGill University
Montréal, Québec, Canada

February 2009

A thesis submitted to the
Faculty of Graduate Studies and Research
in partial fulfillment of the requirements for the degree of
Doctor of Philosophy
in
Mechanical Engineering

Abstract

It is common practice to add reactive metal particles to high-explosive formulations in order to increase the total energy output. The present study is an effort to increase the understanding of metal particle combustion in detonation products.

Aluminum and magnesium particles ranging from 2 to 100 μm are subjected to the flow of detonation products of a stoichiometric mixture of hydrogen and oxygen. Luminosity emitted from the reacting particles is used to determine the reaction delay and duration. It is found that the reaction duration increases as d^n with $n \approx 0.5$, more consistent with kinetically controlled reaction rather than the classical diffusion controlled regime. Emission spectroscopy is used to estimate the combustion temperature, which is found to be well below the flow temperature. This fact also suggests combustion in the kinetic regime. Finally, the flow field is modelled with a CFD code and the results are used to model analytically the behaviour of the aluminum particles.

Furthermore, a simple analytical model is developed to predict ignition of magnesium particles in nitromethane detonation products. The flow field is simplified by considering the detonation products as a perfect gas expanding in a vacuum in a planar geometry. This simplification allows the flow field to

be solved analytically. A single particle is then introduced in this flow field. Its trajectory and heating history are computed. It is found that most of the particle heating occurs in the Taylor wave and in the quiescent flow region behind it, shortly after which the particle cools. By considering only these regions, thereby considerably simplifying the problem, the flow field can be solved analytically with a more realistic equation of state (such as JWL) and a spherical geometry. The model is used to compute the minimum charge diameter for particle ignition to occur. It is found that that the critical charge diameter for particle ignition increases with particle size. These results are compared to experimental data and show good agreement.

Résumé

Il est maintenant courant d'ajouter des particules de métaux réactifs aux formulations d'explosifs pour augmenter l'énergie libérée. Cette étude vise une meilleure compréhension de la combustion de métaux dans les produits de détonation.

Des particules d'aluminium et de magnésium de 2 à 100 μm sont exposées à l'écoulement des produits de la détonation d'un mélange d'hydrogène et d'oxygène. La lumière émise par les particules est utilisée pour déterminer le délai et la durée de la réaction. La durée de la réaction augmente selon d^n avec $n \approx 0.5$. Ces résultats suggèrent un régime de combustion cinétique plutôt que le régime diffusif classique. La température de combustion est mesurée à l'aide de spectroscopie d'émission. La température mesurée est plus basse que celle de l'écoulement, ce qui est également cohérent avec un régime de combustion cinétique. Finalement, l'écoulement est modélisé avec un code Euler, dont les résultats sont utilisés pour modéliser analytiquement le comportement des particules.

Dans un deuxième temps, un modèle analytique simple est développé pour prédire l'ignition de particules de magnésium dans les produits de détonation de nitrométhane. L'écoulement est simplifié en traitant les produits comme gaz

parfaits, qui prennent de l'expansion dans le vide dans une géométrie planaire. Ces simplifications permettent de résoudre l'écoulement analytiquement. Ensuite, la trajectoire et la température d'une seule particule introduite dans l'écoulement sont calculées. La particule est chauffée principalement dans le "Taylor wave" et dans la région quiescente derrière celle-ci. En ne considérant que ces deux régions, le problème est grandement simplifié et il devient possible d'utiliser des géométries et des équations d'état plus réalistes. Le modèle est utilisé pour calculer le diamètre de charge minimum pour l'ignition des particules. Les résultats se comparent favorablement aux données expérimentales.

Acknowledgements

Many people have contributed to my development throughout my graduate studies and they all deserve my gratitude. I would first like to thank my supervisor, Andrew Higgins, from whom I have learned a great deal. I would like to thank the entire Shock Wave Physics group, past and present. In particular, Sam, Jorin, Jeremy and Fan who have directly contributed to this work.

I am grateful to the organizations that have financially supported me during my studies. These include NSERC, FCAR and DRDC. I also very much appreciate the latitude I was given by my current employer (DRDC) to help me conclude this work.

I would also like to thank my parents for having always supported me in every enterprise I have undertaken.

Contents

Contents

Contents

List of Figures

List of Figures

List of Figures

List of Tables

Glossary

A	Surface area
	Constant in the JWL equation of state
B	Constant in the JWL equation of state
Bi	Biot number
C	Constant in the JWL equation of state
	Concentration of oxidizer
C_D	Drag coefficient
C_f	Friction factor
c	Speed of sound
	Speed of light
c_p	Specific heat at constant pressure
c_v	Specific heat at constant volume
D	Mass diffusivity
d	Particle diameter
E	Internal energy
E_a	Activation energy
f	Non-dimensional pressure

h	Coefficient of convective heat transfer
	Planck's constant
i	Radiation intensity
k	Chemical kinetic rate
	Thermal conductivity
	Boltzmann's constant
L	Latent heat
m	Mass
n	Power law exponent
Nu	Nusselt number
p	Pressure
Pr	Prandtl number
Q	Chemical heat release
$\dot{Q}$	Rate of heat transfer
R	Universal gas constant
	Radial shock location
$R_{1,2}$	Constants in the JWL equation of state
r	Radial coordinate
Re	Reynolds number
Sh	Sherwood number
T	Temperature
t	Time
u	Flow velocity
v	Velocity
We	Weber number
y	Radial coordinate

Greek symbols

α	Thermal diffusivity
β	Coefficient of mass diffusion
δ	Boundary layer thickness
ϵ	Emissivity
ϕ	Non-dimensional flow velocity
ψ	Non-dimensional density
γ	Ratio of specific heats
λ	Wavelength
ν	Stoichiometric coefficient
ω	Constant in the JWL equation of state
ρ	Density
σ	Stefan-Boltzmann constant
τ	Time
ζ	Non-dimensional radial coordinate

Subscripts

bp	Boiling point
c	Combustion
	Charge
CJ	Chapman-Jouguet
E	Equator
f	Fluid
	Fusion
i	Interface
ign	Ignition
L	Liquid
mp	Melting point
o	Initial condition
p	Particle
r	Reaction
s	Solid
	Shock
v	Vaporization
w	Wall
∞	Free stream

Chapter 1

Introduction

The addition of reactive metals (such as aluminum, magnesium, etc.) to condensed explosives in order to increase the total energy release of the explosive is now common practice. Although the metals (typically in powdered form with diameters ranging from submicron to millimetres) generally do not react quickly enough to contribute to the detonation front itself (Haskins *et al.* [1]), they can react in the products of the condensed phase explosive or in the surrounding atmosphere, significantly contributing to the strength of the blast wave. The energy release of metal combustion with air (20-30 kJ per g of metal) compared to the energy release of typical high-explosives (5 kJ per g of explosive) suggests that a significant increase in the effective energy release of an explosive can be realized if the reaction of the metal particles can be organized to occur sufficiently fast to contribute to the blast wave. Many outstanding questions remain in such systems. For example, it is not clear when and where the particles ignite, whether they react with shock-heated air or detonation products, etc. It is difficult to obtain detailed quantitative

data related to this phenomenon because of the nature of condensed-phase detonations.

Recent experimental results by Frost *et al.* [2], [3], [4] conducted with packed beds of aluminum and magnesium particles saturated with sensitized liquid nitromethane have shown that there exists a critical charge diameter for "prompt" reaction of the expanding metal particle cloud. If the charge is smaller than this critical diameter, then "delayed" reaction is observed (defined by the authors as being of a timescale too long to contribute to the blast wave, typically above 1 ms). With even smaller charges, particles remain completely inert (non-reactive). Sub-critical (delayed reaction) charges produce blast waves approximately one order of magnitude weaker than super-critical charges with prompt uniform reaction throughout the particle cloud. Between the super-critical and sub-critical reaction regime, there exists a transition regime in which prompt reaction occurs at discrete locations of the particle cloud, while the blast strength varies between the two limits. For both spherical and cylindrical charges, the critical diameter for particle ignition (CDPI) is found to depend on the particle size, morphology, mass fraction and material. For spherical magnesium particles the CDPI increases with increasing particle size (Frost *et al.* [2]). The phenomenon is more complex for spherical aluminum particles in which case the CDPI is at a minimum for particles near 30-50 μm (Frost *et al.* [3], [4]). Changing the charge casing material from glass to aluminum and steel also results in a monotonic increase of CDPI with increasing particle diameter (Zhang *et al.* [5]). This indicates that the control of the adiabatic expansion rate of the detonation products plays a significant role. It would be of interest to identify the scaling laws responsible for the CDPI behaviour and understand the parameters that determine if particle reaction

will occur.

To date, multiphase computational fluid dynamics (CFD) models have been used (Frost *et al.* [3], [4], Zhang *et al.* [5], Ripley *et al.* [6], Milne *et al.* [7], Cooper *et al.* [8], Massoni *et al.* [9], Kim *et al.* [10], etc.) to predict the conditions for metal particle reaction in explosives. Mesoscale modelling with hydrocodes is also widely used (Frost *et al.* [11], Ripley *et al.* [12], Zhang *et al.* [13], Milne *et al.* [7], etc.). While such models can, in principle, model a great amount of detail in the phenomena of interest, it would be highly desirable to develop an analytic model that captures the key elements of the problem in a way that makes the dominant features easily discernible.

Two approaches are taken in this study to gain insight into the phenomenon of metallized explosives. The first is to experimentally simulate the high-explosive detonation products with gaseous detonation products. Metal particles are injected into a gas detonation tube and their behaviour can be directly observed. In this way, bench-top experiments can be conducted in the laboratory and more quantitative data (such as combustion time and temperature) can be obtained.

The second approach is to model the high-explosive detonation products without including the effects of the particles on the detonation wave or the subsequent flow of detonation products. The Taylor wave and the subsequent expansion of the products are first modelled in a highly idealized manner: the products are assumed to expand into a vacuum in a planar geometry and to obey the ideal gas law with constant $\gamma = 3$. Due to these approximations, the flow field can be solved completely analytically. Much insight can be gained into the phenomenon in this manner.

1.1 Particles in Gaseous Detonation Products

In this study, aluminum and magnesium particles are placed in a gaseous detonation tube containing a stoichiometric mixture of hydrogen and oxygen. The mixture is detonated and the particles are entrained in the hot flow of detonation products expanding into an optically clear test section. This setup allows the use of optical diagnostics to study the combustion of the metal particles with the detonation products. The time-resolved luminosity emitted by the particles is used to quantify the reaction delay and duration (see Beckstead [14] for example). Also, emission spectroscopy is used to determine the temperature of the burning metal particles (see Goroshin *et al.* [15] for example).

Aluminum combustion has been studied extensively for decades. This large body of experimental results has lead to a good understanding of the classical diffusion flame structure around a particle (Turns [16], Glassman [17], etc.). The classical model of aluminum combustion consists of a thin spherical diffusion flame, located a finite distance away from the particle surface (see Fig. 1.1). Aluminum vapour diffuses from the particle surface to the flame where it is consumed with oxidizer diffusing from the surroundings. Combustion products then diffuse away from the flame. Using the conservation laws, one can solve for the temperature and concentration profiles and therefore the heat flux to the particle surface. The heat flux is related to the evaporation rate which is also the reaction rate. In this combustion regime, the reaction rate-controlling mechanism is the diffusion of oxidizer to the flame surrounding the particle.

It is known that aluminum can react in a kinetic regime (as opposed to

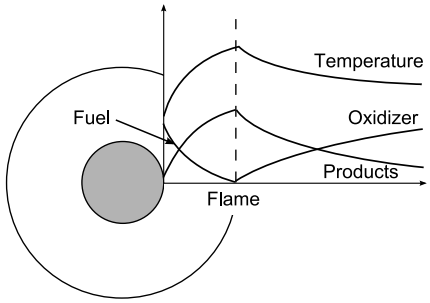

Figure 1.1. Classical model of diffusion-limited flame around metal particle

the above-described diffusive regime; see for example Glassman [17], Bazyn *et al.* [18] and Vulis [19]). Much less experimental data is available for aluminum combustion in the kinetic regime because it occurs when the particles are small (less than approximately 20 μm, Bazyn *et al.* [18]) and are therefore difficult to observe. It is also known that higher relative flow velocities should cause the transition from the kinetic to diffusive regimes to occur at larger particle sizes, i.e., higher flow velocity promotes the kinetic regime (Vulis [19]). This is because the higher flow velocity increases the heat and mass diffusion rates by convection to a point where chemical kinetic rates become the limiting process.

Most experimental techniques to study aluminum combustion (propellants, flat-flame burner, laser ignition, flash tube ignition, reflected shock tube, constant volume explosion bomb, [14], [20]) produce little or no relative flow velocity over the metal particle (typically much less than 10 m/s). These types of experiments reflect the flow velocities encountered in propulsion applications (e.g. solid propellants) where there is little relative motion between the particles and the flow. This is in contrast to metal combustion in detonation products of condensed or gaseous explosives, where the flow velocity can be as high as 1500 m/s.

For all these reasons, it is of interest to study the combustion of aluminum particles in the high-speed flow of detonation products. In the present study, aluminum particle combustion is studied in the flow of detonation products of a hydrogen - oxygen mixture. The use of the highly transient flow field of expanding detonation products means that the particle does not experience steady conditions. If the motivation were to generate a steady environment to study particle reaction, then other types of experimental facilities, such as shock tubes or constant-volume combustion bombs, would be preferable. However, the transient flow field used in this experiment is similar to the actual flow encountered in the detonation of explosives loaded with reactive particles, in that it incorporates the competition between the mechanical and thermal relaxation of the particles with the fact that the flow field itself is undergoing relaxation (Tanguay *et al.* [21]). Note that the timescale over which the detonation products expand in the Taylor wave is on the same order magnitude as the timescale of particle mechanical and thermal equilibration with the flow.

The objective of the present study is to determine the combustion mechanism of aluminum and magnesium particles in the flow of hydrogen - oxygen detonation products. By measuring the reaction delay, duration, and temperature of the burning metal particles, it is hoped that it will be possible to determine whether the particles react in the well-known diffusive regime or in the less-studied kinetic regime. This will allow an assessment of the effect of flow velocity on the combustion of metal particles in the context of metallized high-explosives. The better understanding of the kinetic regime will not only be applicable to metallized high-explosives but also to high-burning rate propellants and combustion of nanometric metal particles.

Chapter 2 is a review of the literature relevant to aluminum and magnesium combustion. This chapter also reviews the various models for metal particle combustion. Chapter 3 is a description of the experimental apparatus and diagnostics that were used in the present study. Chapter 4 describes the experimental results in the context of explosives loaded with reactive metal particles. Finally, Chapter 5 describes CFD modelling of the metal particles in the gaseous detonation products.

1.1.1 Other Relevant Work

Of particular relevance to the subject of particles in the flow of gaseous detonation products is the body of work on pulsed detonation thermal spraying (PDTS). This process consists in coating a substrate with powdered material by the use of gaseous detonations. Essentially, a tube open at one end is filled with detonable gas while a powdered material is injected in the tube. The gaseous mixture is then ignited at or near the closed end of the tube. After a short run-up distance, the combustion wave undergoes a transition and a detonation wave forms and propagates toward the open end of the tube and the substrate. The high-temperature and high-velocity detonation products accelerate and heat the particle. Eventually, the hot particles exit the tube and collide with the substrate and form a high-density coating. The cycle is then repeated with fresh detonable mixture and coating powder.

The coatings achieved with this technique have high density, low porosity, high-hardness, strong adhesion and high wear resistance (Ramadan and Butler [22]). Another important benefit is achieved by the intermittent nature of the process which allows the substrate to be kept at relatively low tempera-

ture [22]. Fauchais *et al.* [23] is a thorough review article that presents the state of current knowledge in thermal spraying technologies.

In PDTS, the quality of the coating depends on several factors, such as geometry, gas composition, particle material, size, temperature and velocity. With so many factors and variables, the need for analytical or numerical modeling is obvious. Since particle loadings are generally small, most of the modelling effort is concerned with a single particle with no effect on the flow field. The flow field is usually solved by one-dimensional Computational Fluid Dynamics (CFD) calculations [23] (see Alkam and Butler [24] for example). However, some studies now include two-dimensional axisymmetric calculations to take into account the diverging flow near the substrate (see Ramadan and Butler [25] for example). These models typically include a single drag term in the momentum equation and convective and radiative heat transfer in the energy equation. Convective heat transfer is modeled by usual engineering correlations. Overall, the approach is very similar to the one adopted in the present work for particles in the products of gaseous detonations. In general, there is no chemical reaction of the particles with the detonation products in PDTS. However, modelling the dynamics and heating of the particles as is done in this thesis is directly relevant to PDTS.

1.2 Model of Particles in Products of High-Explosives

As was mentioned above, the modelling approach taken in the present study is different from what is usually done, i.e., multiphase CFD calculations (Frost *et*

al. [3], [4], Zhang *et al.* [5], Ripley *et al.* [6], Milne *et al.* [7], Cooper *et al.* [8], Massoni *et al.* [9], Kim *et al.* [10], etc.). Instead, the objective here is to develop a highly simplified model that incorporates the minimum details necessary to capture the governing physical processes that determine the basic concept of critical charge diameter for ignition and reaction of the particle cloud in a given explosive dispersal event and essential phenomena for scaling of CDPI. This model is also useful to assess the relative contributions toward particle ignition made by the detonation front itself, the subsequent product expansion, and the shock-heated air the particles will encounter if they leave the detonation products.

First the flow field generated by the high-explosive detonation products is modelled in a highly idealized manner: the products are treated as a perfect gas (with $\gamma = 3$) expanding into a vacuum, in a planar geometry. Due to these approximations, the flow field can be solved completely analytically (see Stanyukovich [26]). Much insight can be gained into the phenomenon of interest in this manner. Metal particles are then introduced in this flow field and their trajectories and convective heating histories can be calculated by solving simple ODE's. The model assumes that the particles do not affect the flow field. This one-way coupling assumption is valid for a small particle loading in the high-explosive (see Rudinger [27] for example). The particles could be viewed as a small perturbation to the flow field that would exist in the case of a homogeneous charge (i.e., a charge without particles). This is not the case for the experimental data obtained by Frost *et al.* [3], [4] used for comparison with this model, which used packed beds of particles. Nevertheless, the simplicity of the model makes the exercise worthwhile.

Subsequently, more realistic models are developed for the Taylor wave [28]

region: spherical geometry, Jones - Wilkins - Lee (JWL) [29] equation of state, etc. Of course, with these more realistic features, a smaller portion of the flow field solution can be computed analytically. Finally, the analytical model results suggest further simplifications of the problem in order to obtain a fully analytical scaling law for the CDPI as a function of particle size.

Chapter 6 describes the model that was developed in the present study. Also discussed in this chapter are the results obtained from the model and comparison with experiments. Finally, Chapter 7 describes the further simplifications that are made to the model in order to obtain an analytical scaling law.

Chapter 2

Theoretical Considerations

In order to better appreciate the results of the present study, it is instructive to review the classical models of particle combustion. The following sections aim to briefly derive these models and highlight their distinctive features in order to gain a better understanding of metal particle combustion. This will place the subsequent results in context. It is also in this chapter that the relevant literature is reviewed.

By placing a metal particle in a hot convective and oxidizing environment, one may expect a number of scenarios to take place. The simplest case is that the particle simply evaporates due to heat transfer from the flow. The metal is either not reacting at all with the flow or, the metal vapour is reacting sufficiently far downstream of the particle that heat produced by the exothermic reaction does not contribute to particle heating. This model is reviewed in Section 2.1 for both quiescent and convective flows.

The second possibility is for the particle to react in the classical diffusion-

limited regime with a thin flame surrounding the particle. This is the regime that is generally observed in usual metal particle combustion experimental conditions (relatively large particles in quiescent flow). The classical diffusion model can be extended to convective flows, as is done for droplet evaporation. This model is reviewed next, in Section 2.2.

Section 2.3 describes a model proposed by Connell [30] for particle film stripping in high-velocity, high-Weber number flows. This model addresses the case where the hydrodynamic forces due to the high-speed flow overcome the stabilizing effect of the surface tension of a molten or melting particle. In this scenario, as the particle melts, the molten film is stripped off of the particle. Again, it is assumed in this model that any heat released by chemical reaction occurs sufficiently far downstream not to influence the particle melting rate.

The next section (2.4) describes a simple kinetic - diffusive model. This model, despite its simplicity, clearly illustrates the differences between combustion in a kinetic-limited and diffusion-limited regime. This model provides a context for interpreting the experimental results.

Finally, Section 2.5 reviews the phenomenon of ignition in relation to metal particle combustion. There are different criteria for metal ignition in the literature and this section attempts to survey the various theories in relation to the present study, for both aluminum and magnesium particles.

2.1 Classical Model of Droplet Evaporation

Consider a molten droplet in a hot convective flow. Once the droplet reaches the metal boiling point, subsequent heat transferred to the droplet contributes to evaporating the metal. The goal here is to determine the rate of metal evaporation. This rate leads to the scaling law for evaporation time. Before elaborating upon the model, consider the following assumptions that are made:

1. The evaporation process is quasi-steady. This assumption eliminates the necessity to use partial differential equations.
2. The liquid metal has zero solubility for gases.
3. The droplet temperature is uniform and equal to the boiling point.
4. Lewis number is equal to unity ($\alpha = D$) which permits the use of the Shvab-Zeldovich energy equation.
5. Thermophysical properties are constant.

The problem then consists of heat and mass transfer across the boundary layer (in quiescent flow, the boundary layer thickness is infinite; see Fig. 2.1). The rate of metal evaporation from the surface is given by an energy balance at the particle surface:

$$\dot{Q}_s = \dot{m} L_v \tag{2.1}$$

One must then evaluate the heat flux at the surface from Fourier's law of heat conduction:

$$\dot{Q}_s = 4\pi k_f r_s^2 \left.\frac{\mathrm{d}T}{\mathrm{d}r}\right|_{r_s} = \dot{m} L_v \tag{2.2}$$

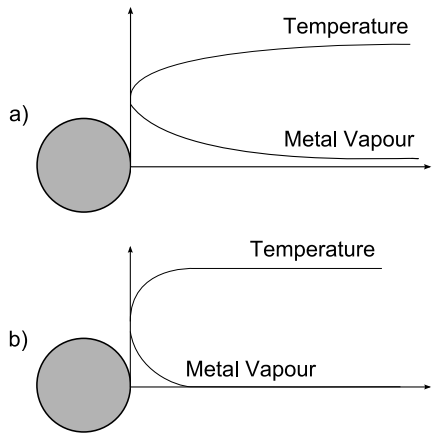

Figure 2.1. Temperature and concentration profiles around evaporating droplets in a) quiescent atmosphere and b) convective flow

The temperature profile needs to be known in order to evaluate the temperature gradient at the particle surface. However, let us first consider the continuity equation. Since the quasi-steady assumption was made (no accumulation of mass occurs), one must then have the mass flow rate of metal to be constant:

$$\dot{m} = 4\pi r^2 \rho v = constant \tag{2.3}$$

One can now use the Shvab-Zeldovich form of the energy equation across the boundary layer (see Turns [16] for example):

$$\frac{1}{r^2}\frac{\mathrm{d}}{\mathrm{d}r}\left[r^2\left(\rho v c_p T - \rho D c_p \frac{\mathrm{d}T}{\mathrm{d}r}\right)\right] = 0 \tag{2.4}$$

where the first and second terms represent advection and diffusion of aluminum vapour, respectively. The right hand side is equal to zero because there is no chemical reaction in the boundary layer. Making use of the assumptions above, the continuity equation (Eq. 2.3) and the fact that ρD is a constant, Eq. 2.4

becomes:

$$\frac{\mathrm{d}}{\mathrm{d}r}\left[r^2\frac{\mathrm{d}T}{\mathrm{d}r}\right] = A\frac{\mathrm{d}T}{\mathrm{d}r} \tag{2.5}$$

where

$$A = \frac{\dot{m}c_p}{4\pi k_f} \tag{2.6}$$

By separation of variables, one can easily integrate twice to obtain:

$$\frac{1}{A}\ln(AT + C_1) = -\frac{1}{r} + C_2 \tag{2.7}$$

or, solving for temperature,

$$T(r) = \frac{1}{A}\exp\left[A\left(C_2 - \frac{1}{r}\right)\right] - \frac{C_1}{A} \tag{2.8}$$

Two boundary conditions are needed to evaluate the two integration constants, C_1 and C_2. The first is at the droplet surface where the temperature is the metal boiling point. The second is at the edge of the thermal boundary layer, where the temperature is the ambient temperature:

$$T(r_s) = T_{bp} \tag{2.9}$$

$$T(r_s + \delta_T) = T_\infty \tag{2.10}$$

One can express the boundary layer thickness in terms of the Nusselt number:

$$r_s + \delta_T = \frac{\mathrm{Nu}}{\mathrm{Nu} - 2}r_s \tag{2.11}$$

Substituting Eq. 2.9 and 2.10 into Eq. 2.7, one obtains two equations for the two integration constants. Solving the two equations simultaneously and substituting back into Eq. 2.8, one obtains the temperature profile:

$$T(r) = \frac{(T_\infty - T_b)\exp\left(\frac{-2A}{\mathrm{Nu}r_s}\right)\exp\left(\frac{A}{r_s} - \frac{A}{r}\right) - T_\infty\exp\left(\frac{-2A}{\mathrm{Nu}r_s}\right) + T_b}{1 - \exp\left(\frac{-2A}{\mathrm{Nu}r_s}\right)} \tag{2.12}$$

Taking the derivative of Eq. 2.12, evaluating at the droplet surface and substituting into Eq. 2.2, one can solve for the evaporation rate (mass flow rate):

$$\dot{m} = \frac{2\pi \mathrm{Nu} k_f r_s}{c_p} \ln(1 + B_q) \tag{2.13}$$

where

$$B_q = \frac{c_p(T_\infty - T_b)}{L_v} \tag{2.14}$$

Note that Eq. 2.13 is very similar to the classical result for droplet evaporation in a quiescent atmosphere, given by:

$$\dot{m} = \frac{4\pi k_f r_s}{c_p} \ln(1 + B_q) \tag{2.15}$$

In fact, the two expressions differ only by the appearance of the Nusselt number. For quiescent conditions, Nu = 2, and Eq. 2.13 becomes exactly Eq. 2.15. It is obvious that convection increases the evaporation rate by increasing the rate of heat transfer from the surrounding gas.

The evaporation time can be determined from the following expression in terms of droplet diameter:

$$\frac{\mathrm{d}d_p}{\mathrm{d}t} = \frac{2\mathrm{Nu} k_f}{\rho_l c_p d_p} \ln(B_q + 1) \tag{2.16}$$

For high Reynolds numbers, the Nusselt number can be correlated to the Reynolds number:

$$\mathrm{Nu} = C\mathrm{Re}^n \tag{2.17}$$

One can integrate Eq. 2.16 and find the evaporation time. One finds the evaporation time to be proportional to the diameter raised to the power $2-n$:

$$\tau_v \sim d_p^{2-n} \tag{2.18}$$

For Reynolds numbers ranging from 100 to 10000, n is approximately equal to 0.55. Therefore, the evaporation time

$$\tau_v \sim d_p^{1.45} \tag{2.19}$$

In the case of no convection, Nu = 2, the evaporation time is proportional to the diameter square (the classical d^2 law).

Note that when the latent heat of vaporization is large compared to the enthalpy difference between ambient and the boiling point, i.e., $B_q << 1$ (which is the case here), a simpler analysis can be made. Essentially, the advection of metal vapour is small compared to its diffusion and the energy equation becomes much simpler:

$$Q = \frac{4\pi r_s^2 \mathrm{Nu} k_f}{d_p}(T_\infty - T_b) = \dot{m} L_v \tag{2.20}$$

Solving for the evaporation rate gives a result nearly identical to Eq. (19) for small B_q.

2.2 Classical Model of Droplet Combustion

In the previous model, it was assumed that chemical reaction of the metal vapour was not coupled with the evaporation process. This would be the case if the chemical reaction were to occur sufficiently far from the particle. If this is not the case, heat released by chemical reaction will contribute to the evaporation of liquid metal and accelerate the evaporation process. Consider the classical diffusion model of droplet combustion: see Fig. 2.2. The model is similar to the previous model for evaporation. The main difference is that the gaseous environment surrounding the droplet is divided into two regions

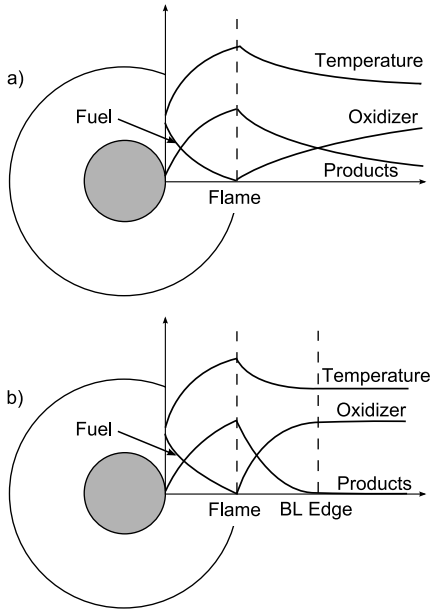

Figure 2.2. Temperature and concentration profiles around particle burning in diffusion-limited mode in a) quiescent atmosphere and b) convective environment

by an infinitesimally thin flame. In the inner region, metal vapour diffuses toward the flame, where it is consumed. In the outer region, oxidizer diffuses from infinity toward the flame where it is consumed. Products also diffuse in the opposite direction.

The solution of the problem then consists of solving the species and energy conservation equations in both regions. Boundary conditions are given at the particle surface and flame front for the inner region and flame front and infinity (or edge of the boundary layer in the presence of convection) for the outer layer. This classical problem (see Turns [16] for example) has the following solution:

$$\dot{m} = \frac{4\pi k_f r_s}{c_p} \ln(1 + B_{o,q}) \tag{2.21}$$

where

$$B_{o,q} = \frac{\frac{\Delta h_c}{\nu} + c_p(T_\infty - T_b)}{L_v} \tag{2.22}$$

This is the same form that was obtained for pure evaporation with the addition of the enthalpy of combustion term appearing in the transfer number. Therefore, we can conclude that the combustion time will also follow the classical d^2 law. This result, however, is for a droplet burning in a quiescent atmosphere. A similar analysis can be performed in a convective environment where the outer region extends only to the edge of the thermal boundary layer. As before, the thermal boundary layer thickness can be expressed as a function of the Nusselt number. As with pure evaporation, the result with convection is identical to the quiescent case except for the explicit appearance of the Nusselt number:

$$\dot{m} = \frac{2\pi \mathrm{Nu} k_f r_s}{c_p} \ln(1 + B_{o,q}) \tag{2.23}$$

Note once more that in the quiescent case, Nu = 2, and the result corresponds exactly to the diffusion case. Also, the combustion time no longer follows the d^2 law. The combustion time is now proportional to d^{2-n} where n is the exponent in the correlation for the Nusselt number (approximately equal to 0.55 in the conditions of interest).

2.3 Droplet Breakup Model - Film Stripping

The classical picture of aluminum combustion involves aluminum evaporating from a molten droplet and reacting in a flame zone around the particle. However, this can only be the case in conditions of relatively low-speed flow. In

high-speed flow, large hydrodynamic forces can overcome the stabilizing effect of surface tension and cause the liquid core to break up, or strip a liquid film off of a melting solid particle (see Connel [30] and Fox *et al.* [31], [32]). One must examine the Weber number, We, to compare the hydrodynamic forces (inertial forces) to the surface tension:

$$\mathrm{We} = \frac{\rho U_\infty^2 d}{\sigma} \tag{2.24}$$

For liquid droplets, there is a critical Weber number ($\mathrm{We}_c = 12$) below which the surface tension dominates and the droplet remains intact [33]. For We $>$ We_c, the droplet becomes unstable and breaks up. In the present experiment of particles in products of gaseous detonations, the Weber number is maximum just behind the detonation, where the relative flow velocity is maximum. At this point, the Weber number ranges from 1.7 to 85 for 2 to 100 μm particles respectively. The critical Weber number is reached for 14 μm particles. Therefore, Weber breakup is possibly an important mechanism in the present experiment, at least for a range of particle sizes. Note that as the particles accelerate, the Weber number decreases.

There are various droplet breakup mechanisms, depending on the magnitude of the Weber number [33]. Droplet breakup is not instantaneous and the breakup time also depends on the Weber number as well as other parameters.

Note that the above applies to liquid droplets. In the case of aluminum particles, a similar process will occur if the time to melt the particle is short compared to the breakup time [30]:

$$t_m << t_b \tag{2.25}$$

However, if the breakup time is short compared to the melt time, film stripping

occurs:

$$t_m >> t_b \tag{2.26}$$

In this case, a liquid film is continuously removed from the particle as the solid core melts. Finally, if the melt time and breakup time are on the same order, a combination of the two processes occurs: a liquid film grows to a critical size, the film becomes unstable, the film is stripped off the particle and the process repeats. To determine which of these limiting mechanisms is predominant, one can estimate the melt and breakup times:

$$t_m = \frac{mL_f}{q} \tag{2.27}$$

$$t_b = \tau \frac{d}{U} \left[\frac{\rho_m}{\rho_f} \right]^{\frac{1}{2}} \tag{2.28}$$

where the non-dimensional characteristic breakup time, τ, can be correlated to the Weber number and depends on the breakup mechanism [33]. However, the characteristic non-dimensional breakup time varies only between 3 and 7. Due to the uncertainty in other parameters, it does not appear worthwhile to model this complex dependence on the Weber number. Instead, an average value of 5 is used here. One can then compute the ratio of the melt time to the breakup time which ranges from:

$$275 \leq \frac{t_m}{t_b} \leq 5200 \tag{2.29}$$

$$\text{for } 2 \leq d \leq 100\mu\text{m}, \tag{2.30}$$

respectively.

In other words, the melt time is always much longer than the breakup time, which means the liquid film is continuously stripped off the solid particle as

it melts. The consequences of this are that the chemical reaction probably occurs in the wake of the particle and the heat released by chemical reaction may never be fed back to the particle. In other words, the rate of chemical reaction is completely decoupled from the heat released and depends only on the rate of particle melting in the hot detonation products.

2.3.1 Liquid Film Stripping Model

Consider Fig. 2.3 to represent the liquid film stripping mechanism, as was done by Connell [30]. The following assumptions are made:

1. The process is quasi-steady.
2. Film removal is at the equator.
3. The film velocity profile is linear.
4. The air-film interface velocity is much less than the free stream velocity.
5. The chemical composition of the film is uniform (pure aluminum).
6. Vaporization from the film surface is negligible.

The quasi-steady assumption implies that the rate at which the metal melts is equal to the rate at which liquid metal is stripped away from the particle. Film removal at the equator is verified experimentally and roughly corresponds to laminar boundary layer separation [34]. The linear velocity profile is assumed simply as a matter of convenience. It has been shown by Lees [35] that the air-liquid interface velocity is small compared to the

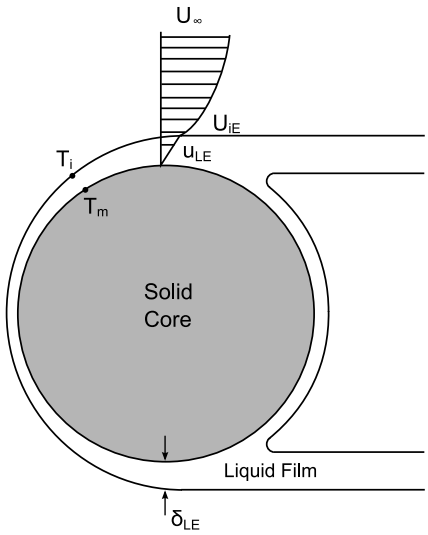

Figure 2.3. Sketch of the film stripping mechanism

free stream velocity; this permits the use of a skin friction coefficient C_f to calculate the shear stress at the interface. The uniform chemical composition of the film allows one to use the thermophysical and transport properties of pure aluminum to represent the film. See Fig. 2.3 for a schematic of the model.

Conservation of mass gives the melt rate equal to the film stripping rate:

$$2\pi r^2 \dot{m}'' = \int_0^{\delta_{LE}} 2\pi r \rho_L u_L(y) dy \tag{2.31}$$

The velocity profile inside the film at the equator is given by:

$$u_{LE}(y) = \frac{U_{iE}}{\delta_{LE}} y \tag{2.32}$$

Substituting Eq. 2.32 into Eq. 2.31 and integrating, one obtains:

$$\delta_{LE} = \frac{2r\dot{m}''}{\rho_L U_{iE}} \tag{2.33}$$

A second equation is obtained by equating the shear stress on both sides of the air-film interface at the equator:

$$\frac{1}{2}\rho_\infty U_\infty^2 C_f = \mu_L \frac{U_{iE}}{\delta_{LE}} \tag{2.34}$$

A third equation is obtained by equating the heat flux at the interface:

$$h(T_\infty - T_{iE}) = \frac{k_L}{\delta_{LE}}(T_{iE} - T_m) \tag{2.35}$$

And finally, assuming the temperature of the molten metal stripped off the particle is simply the arithmetic mean of the melting point and the temperature at the interface, an energy balance on the liquid film provides a fourth equaton:

$$h(T_\infty - T_i) - \dot{m}'' L_f = \frac{1}{2}\dot{m}'' c_{pL}(T_{iE} - T_m) \tag{2.36}$$

The result is a system of 4 equations (Eqs. 2.33, 2.34, 2.35 and 2.36) with 4 unknowns: δ_{LE}, $\dot{m}''$, U_{iE} and T_{iE}. Solving this system gives the rate of metal melting which can be related to the rate of change of particle radius. These equations can then be coupled to Newton's second law and the flow field properties. Note that the "classical" energy balance on the particle must be used until its temperature reaches the melting point. From this point, the above equations replace the energy balance.

The model was integrated with the CFD simulation (see Chapter 5) of the experimental work that will be described in Chapters 3 and 4. Because of a singularity when integrating the model to a particle diameter of zero, the simulation was stopped when the particle mass reached 1% of its original mass. This is when reaction is assumed to stop. The reaction duration is plotted on Fig. 2.4. The reaction time predicted by the model is approximately proportional to d^2. The film stripping model predicts a reaction time approximately

15 times shorter than the Beckstead [14] correlation. It is also in poor agreement with the present experimental data which shows a $d^{0.5}$ dependence on diameter and much longer reaction times (only for the largest particles studied does the film stripping model nearly intersect the experimental data).

It should be noted that the Weber number was calculated based on the relative flow velocity immediately behind the detonation. While this is the initial condition, the relative flow velocity rapidly decreases and therefore, the Weber number also decreases (with the square of velocity). Thus, it is not surprising that the model does not reproduce the experimental data. Much larger particles may be required to show the film stripping mechanism.

2.4 Simple Kinetic - Diffusive Model of Combustion

There are two distinct regimes in which a metal particle can burn: kinetic and diffusive. To illustrate this, consider a particle reacting with a gaseous oxidizer. Suppose the chemical reaction occurs at the particle surface (a more rigorous approach is to assume that chemical reaction occurs at a flame front surrounding the particle but since both these approaches give qualitatively similar results the simpler case is used here to illustrate the difference between the two regimes). Assuming an Arrhenius form, the reaction rate can be expressed in terms of the chemical kinetic rates (dependent upon the concentration and the temperature at the particle surface):

$$\dot{m} = ACk = ACk_o \exp\left[\frac{-E_a}{RT}\right] \tag{2.37}$$

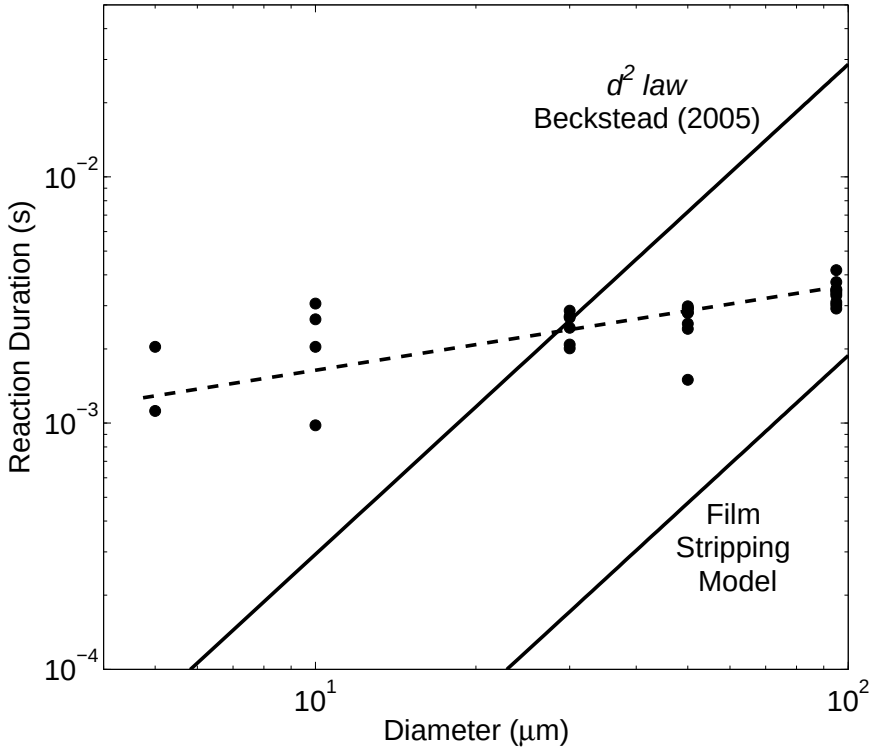

Figure 2.4. Reaction duration as a function of particle size in film stripping mode

equivalently, the reaction rate can be expressed as the mass flux of oxidizer at the particle surface (dependent upon the oxidizer concentration gradient at the surface):

$$\dot{m} = A\beta(C_\infty - C) \tag{2.38}$$

Equating expressions 2.37 and 2.38, one can solve for the oxidizer concentration at the surface, which is *a priori* unknown:

$$C = \left[\frac{\beta}{\beta + k}\right] C_\infty \tag{2.39}$$

Substituting the concentration (Eq. 2.39) back into the expression for the reaction rate (Eqs. 2.37 or 2.38), one obtains:

$$\dot{m} = A\left[\frac{\beta k}{\beta + k}\right] C_\infty \tag{2.40}$$

This expression shows the two different regimes. When $\beta >> k$,

$$\dot{m} = AkC_\infty \tag{2.41}$$

the reaction rate becomes independent of the diffusion rate and only depends on the temperature and the chemical kinetics at the surface of the particle. This is the kinetic regime, illustrated in Fig. 2.5b. In this case, the diffusion of oxidizer is effectively infinitely fast and therefore, the limiting rate is the chemical kinetics. In contrast, when $k >> \beta$,

$$\dot{m} = A\beta C_\infty \tag{2.42}$$

the reaction rate becomes independent of the chemical kinetic rates (and therefore temperature) and only depends on the oxidizer diffusion rate. This is the diffusive regime, illustrated in Fig. 2.5a. In this case, the chemical kinetic rates are effectively infinitely fast, and the limiting rate is the diffusion of oxidizer. In many instances, it is likely that metals react in a mixed regime where both kinetic rates and diffusion influence the combustion rate.

Note that the chemical kinetic rate, k, only depends on temperature:

$$k = k_o \exp\left[\frac{-E_a}{RT}\right] \tag{2.43}$$

and that the oxidizer mass diffusion coefficient can be expressed in terms of the Sherwood number (analogous to the Nusselt number for mass diffusion):

$$\beta = \frac{\mathrm{Sh}D}{d} \tag{2.44}$$

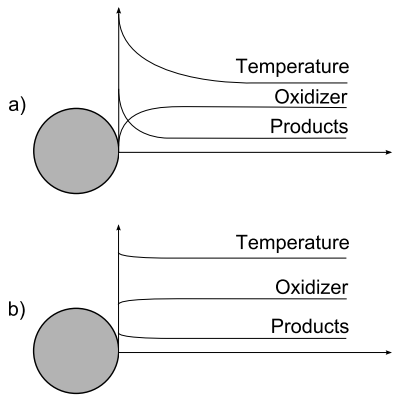

Figure 2.5. Temperature and concentration profiles around particles reacting in the a) diffusion-limited regime and b) kinetically limited regime

2.4.1 Combustion Time

The particle combustion time can be approximated as:

$$\tau_c \approx \frac{m}{\dot{m}} \sim \frac{d^3}{\dot{m}} = \frac{d^3}{d^2 \beta C_\infty} = \frac{d^2}{\mathrm{Sh} D C_\infty} \sim \frac{d^2}{\mathrm{Nu} D C_\infty} \tag{2.45}$$

in the diffusive regime, where one recognizes the classical d^2 law (see Turns [16], Glassman [17] and Vulis [19] for example). However, in the kinetic regime, the combustion time is:

$$\tau_c \approx \frac{m}{\dot{m}} \sim \frac{d^3}{\dot{m}} = \frac{d^3}{d^2 k C_\infty} = \frac{d}{k C_\infty} \tag{2.46}$$

where we find the a linear dependence with d (see Bazyn *et al.* [18], Glassman [17] and Vulis [19] for example).

2.4.2 Effect of Particle Size and Velocity

Note the inverse dependence of β, the oxidizer diffusion coefficient, on the particle diameter, Eq. 2.44. This is the reason why very small particles react

in a kinetic regime, rather than a diffusive regime (see Bazyn *et al.* [18] and Vulis [19]). Because of their small size, the mass diffusion coefficient is very large, and therefore, there is always sufficient oxidizer available and the limiting rate is the chemical kinetics.

In most applications and experiments, the relative velocity between the gas and the particle is less than ∼10 m/s. This means the Nusselt number, which depends on the Reynolds number, is small. However, in some cases (such as the present experiment), the relative flow velocity can be quite large (more than 1 km/s). In this case, the Nusselt number, and therefore β, are quite large, promoting the kinetic regime. In other words, one would expect the particle size at which the transition between the kinetic and diffusive regimes to increase with flow velocity. Increasing flow velocity will also decrease the combustion time in the diffusive regime, but will not affect the kinetic regime. This is illustrated in Fig. 2.6. The curve for diffusion with no flow velocity is a correlation from Beckstead [14]. The experimental data from which it is derived has significant scatter, presumably because it is obtained from various experimental techniques (solid propellant, gas burner, laser, flash and shock) and different oxidizers (oxygen, air, water vapour and carbon dioxide). Beckstead [14] suggests that the combustion time in water vapour is less than twice that in pure oxygen, well within the scatter of the data. The curve for the kinetic regime in Fig. 2.6 assumes that the transition occurs at a particle size of 10 μm. Note that in reality, the transition is presumably not as sharp as illustrated.

With a flow velocity of 1000 m/s, the Nusselt number of a 100-μm particle is approximately 20 (compared to 2 for the quiescent case). In this case, the effect of flow velocity is to reduce the combustion time by a factor of

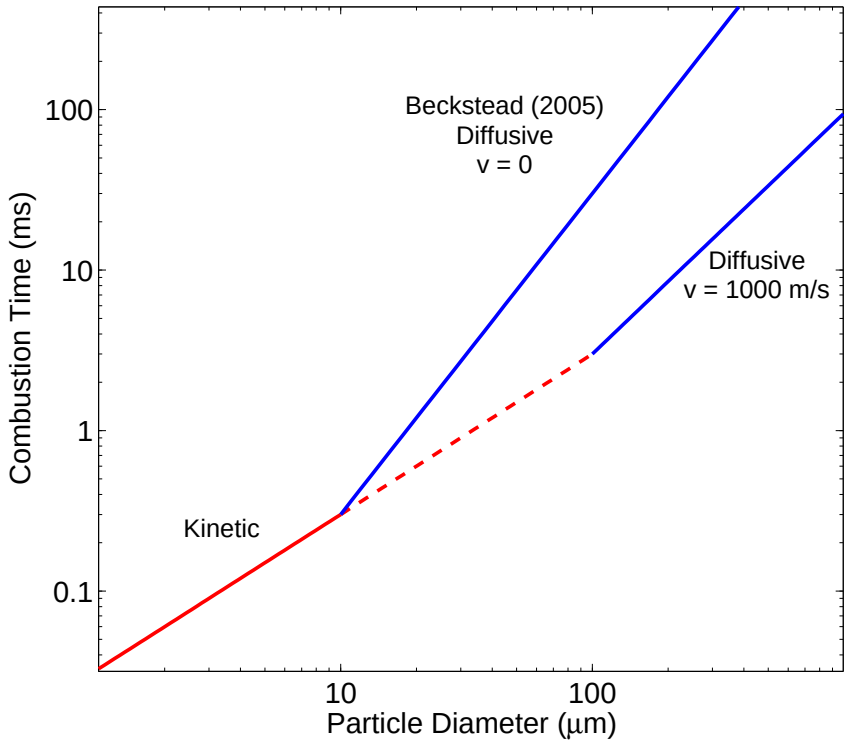

Figure 2.6. Effect of flow velocity on particle combustion time

10. Note that with convection, the diffusive regime no longer follows the d^2 law [16]. This is because the Nusselt number is correlated to the Reynolds number which depends on diameter. Therefore, with convection, one expects the combustion time to be proportional to d^{2-n} (with n ranging from 0.5 to 0.67 [36]).

2.4.3 Particle Temperature

Assuming the reaction process to be quasi-steady, the rate of heat released by the chemical reaction just balances the rate of heat loss to the gas:

$$\frac{\mathrm{d}E}{\mathrm{d}t} = \dot{m}Q - Ah(T_p - T_\infty) \approx 0 \tag{2.47}$$

Solving for the temperature difference between the particle and the gas in the diffusive regime, one obtains:

$$T_p - T_\infty = \frac{\dot{m}Q}{Ah} = \frac{\beta}{h} C_\infty Q \sim C_\infty Q \tag{2.48}$$

because in gases, the Lewis number approaches unity, i.e., diffusion of heat and mass occur at comparable rates (since the mechanism is the same: molecular diffusion). However, in the kinetic regime, the temperature difference is given by:

$$T_p - T_\infty = \frac{\dot{m}Q}{Ah} = \frac{k}{h} C_\infty Q \approx 0 \tag{2.49}$$

since in the kinetic regime $\beta >> k$, and therefore, $h >> k$ also. In the diffusive regime, the particle temperature is significantly higher than the flow temperature, because diffusion rates are small (this causes important gradients in temperature and oxidizer concentration). In the kinetic regime, these gradients are small because, diffusion of heat and oxidizer is fast.

2.5 Ignition

The word *ignition* is often used in a variety of contexts to mean various things. The ignition temperature is not a property of a fuel. Strictly speaking, from

Frank-Kamenetskii [37] thermal ignition theory, the word ignition means thermal run-away. It is the transition between the kinetic and the diffusive regime, or the onset of diffusive combustion. This occurs when heat production dominates the heat loss to the surrounding gas. Consider Fig. 2.7 where both heat production (I) and heat loss (II) are plotted against surface temperature. In general, the two curves intersect at three points (labelled A, B and C). Points A and C are both stable equilibrium points and represent the two possible steady (or quasi-steady solutions). Point A occurs at low temperature and the particle temperature is very near the flow temperature. This is the kinetic regime. Point C is a high-temperature solution, where the particle temperature is significantly higher than the flow temperature. This is the diffusive regime. Point B is an unstable equilibrium point. This is the ignition temperature for this system.

Consider an extreme case where the particle size is very small and/or the flow velocity is very large. In this case, the slope of the heat loss curve (III) may be increased such that the only solution is point A. In this case, the particle will react in the kinetic regime but it cannot be ignited. This does not necessarily mean that the reaction rate must be small.

Consider now, a reactive particle in an oxidizing atmosphere. In general, at any finite temperature, chemical reaction is taking place at a finite rate. This rate may be very small. The particle is said to be reacting in the kinetic regime. As the temperature of the surrounding atmosphere is slowly raised, the heat loss curve of Fig. 2.7 is translated to the right. At some point, the heat production and heat loss curves become tangent: Fig. 2.8. This results in particle ignition or thermal run-away. Note that for the same fuel-oxidizer combination, the ignition temperature depends on flow temperature, velocity,

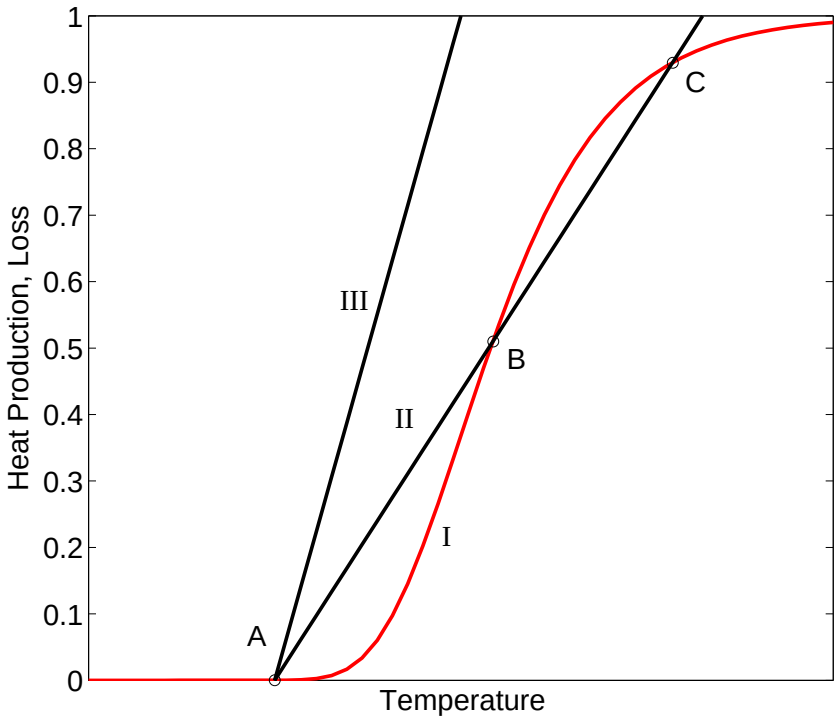

Figure 2.7. Heat production and heat loss as a function of temperature

particle size, etc. Figure 2.9 shows that increasing the particle size lowers the ignition temperature while Fig. 2.10 shows that flow velocity increases the ignition temperature. In other words, ignition occurs more readily (at lower temperatures) for large particle in quiescent gas.

2.5.1 Effective Ignition Temperature

The above considerations only apply in certain cases. In practice, other physical mechanisms can dominate the ignition process (the onset of diffusion-

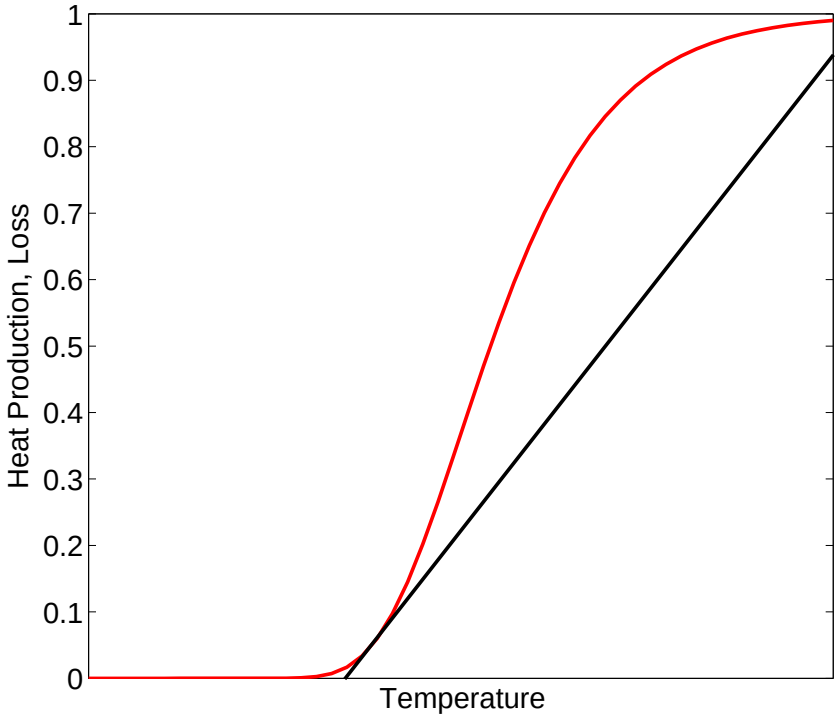

Figure 2.8. Heat production and heat loss are tangent at ignition

limited combustion) such as melting and boiling points. The following sections describe the mechanisms that can lead to an effective ignition temperature.

Aluminum

Oxide Melting Point

The combustion product of aluminum is aluminum oxide, which only exists in the condensed phase. Therefore, as an aluminum particle reacts, an aluminum oxide layer builds on the surface of the particle. Aluminum oxide has

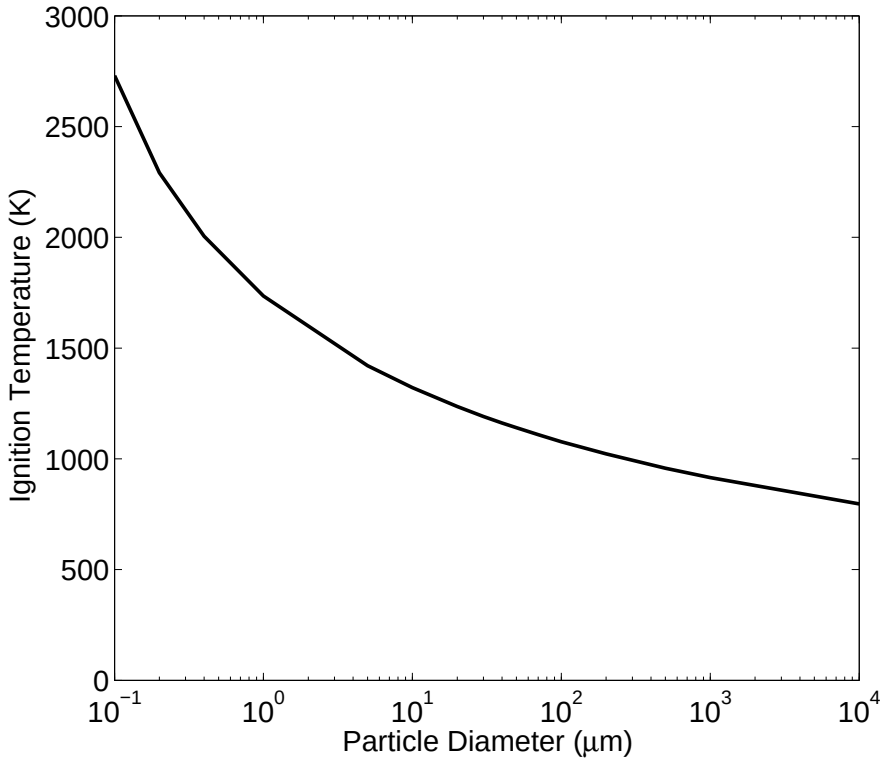

Figure 2.9. Effect of particle size on particle ignition temperature

properties that protect aluminum from further oxidation (Henry *et al.* [38]). Much of the previous work on aluminum combustion has led to the generally accepted concept proposed by Glassman [17] that the onset of diffusive combustion occurs once the oxide layer is removed, in other words, when the oxide layer melts. This mechanism, therefore, leads to an effective ignition temperature that corresponds to the aluminum oxide melting point. While this criterion for ignition of aluminum agrees quite well with many experiments, it does not always apply. In certain experimental conditions, the aluminum particles are found to ignite at much lower temperatures (see Trunov *et al.* [20],

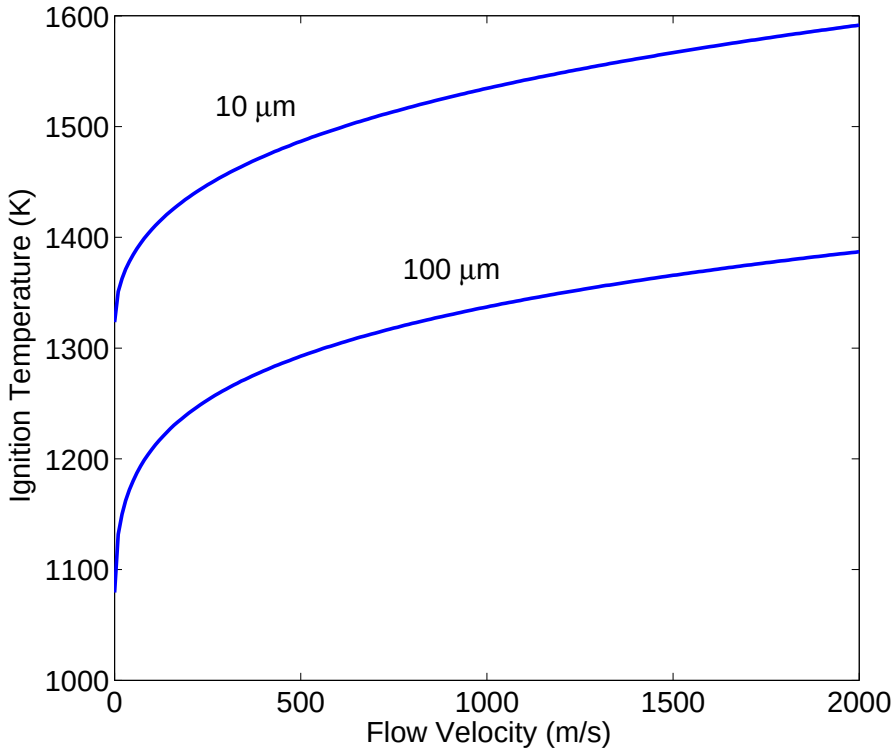

Figure 2.10. Effect of flow velocity on particle ignition temperature

Rozenband *et al.* [39], etc.). Below are some of the theories found in the literature to explain low-temperature ignition of aluminum.

Oxide Mechanical Stress

Rozenband and Vaganova [39], Rosenband *et al.* [40] and Rosenband [41] suggest that in some scenarios, mechanical stresses may break or crack the oxide layer, thereby allowing oxidizer to reach the aluminum. Differences in the coefficients of thermal expansion of aluminum and its oxide can cause these stresses that compromise the oxide layer. Other sources of stress are

metal and oxide phase changes (melting and polymorphic transformations). Thus, the particle may begin to react in a diffusion-limited regime at much lower temperatures than the oxide melting point. This body of work suggests that the rate of particle heating may play an important role in the appearance of the mechanical stresses.

This may be applicable to aluminized explosives, although the stresses produced by the detonation may be much more important than thermal stresses. It is at least an indication that mechanically compromising the oxide layer can result in the onset of diffusion-limited combustion.

Oxide Crystallization

A different theory proposed by Gurevich *et al.* [42] and pursued by Frolov *et al.* [43] and Gurevich *et al.* [44] to explain low-temperature ignition of aluminum particles is based on polymorphic phase transformations in the aluminum oxide layer. Trunov *et al.* [45] also suggest that polymorphic phase transformations need to be considered in ignition of aluminum particles. Aluminum oxide may be amorphous or crystalline. The "natural" oxide that forms on an aluminum particle at room temperature is amorphous [45]. As the temperature of the oxide layer increases, it goes through the following phases:

$$Amorphous \rightarrow \gamma \rightarrow \delta \rightarrow \theta \rightarrow \alpha Al_2O_3$$

The diffusivity of oxidizer through the oxide layer decreases as these polymorphic phase transformations occur. If the temperature is increased slowly, the phase changes have sufficient time to occur and the increasing impermeability of the oxide layer prevents ignition from taking place, until the oxide

layer melts (the classical case). However, if the heating rate is sufficiently fast, the phase changes do not have sufficient time to occur and the particle may begin to react in a diffusion-limited regime below the oxide melting point. This theory was consistent with experimental evidence of smaller particles igniting at lower temperatures (as low as the metal melting point) while larger particles needed to be heated to the oxide melting point (see [44] and [43]).

This phenomenon may be applicable to the metallized explosive environment. The heating rate is the key parameter that governs this phenomenon: the higher the heating rate, the lower the temperature at which ignition occurs. The oxidizing environment produced by high-explosive products probably results in the highest heating rates of all particle combustion experiments. High explosives produce a flow density 3 orders of magnitude higher than gases. Furthermore, the relative flow velocity on the order of 1 km/s, produces a highly convective environment. Finally, the temperatures produced by detonations are also very high. These all contribute to high convective heat transfer rates, and therefore, very high heating rates. It is therefore possible that oxide phase changes may play a role in the combustion of aluminum particles in high-explosive products.

Oxide Integrity Compromised in Detonation

Modelling and simulation studies by Zhang *et al.* [13] and Ripley *et al.* [12] have shown that pressures of tens of GPa in the wake of the detonation cause severe particle deformation. It is therefore quite possible that these large pressures compromise the integrity of the oxide layer and expose aluminum to oxidizer, permitting the aluminum particles to ignite at much lower temperatures than the oxide melting point. This is supported by experimental results

by Gilev [46], and Gilev and Anisichkin [47] where it is found that the electrical conductivity of the detonation products is increased by the presence of aluminum, suggesting that the oxide layer is destroyed by the passage of the detonation wave.

Furthermore, comparison of experiments and multiphase modelling of the detonation of aluminized explosives suggests that in some cases aluminum particles ignite near the aluminum melting point rather than the oxide melting point. Frost *et al.* [4], [3] use the aluminum melting point as an ignition temperature in their multiphase model.

Furthermore, Kim et al. [10] find that the SHAMRC multiphase code [48] agrees better with experiments containing large particles and liquid explosive with a low ignition temperature. In contrast, when the charge contains small particles and significant amount of binder, the code prediction is better with a high ignition temperature. Kim et al. [10] propose that the binder and the smaller particles result in less particle deformation thereby maintaining the the integrity of the protecting oxide layer. The use of larger particles and the absence of binder exposes unreacted metal and leads to particle ignition near the metal melting point.

Magnesium

Magnesium falls in the category of metals for which the oxide layer is loose, porous and does not prevent the diffusion of oxidizer to the metal surface (Breiter *et al.* [49]). Therefore, it is found by most researchers (Markstein [50], Breiter *et al.* [49], Cassel and Liebman [51], etc.) that magnesium particles do not ignite at a specific temperature, but rather behave consistently with Frank-

Kamenetskii [37] thermal ignition theory described in Section 2.5. Ignition in typical conditions is found to occur anywhere between approximately 700 and 1363 K.

However, work done by Fox *et al.* [31], [32] on incident shock wave ignition of magnesium particles, showed consistent ignition near or at the metal melting point. They conclude that near the melting point, particle thermal erosion becomes important and the rapid vaporization of eroded mass leads to ignition in the particle wake.

Chapter 3

Experimental Details

3.1 Experimental Apparatus

The apparatus consisted of a tube separated into two sections by a gate valve (see Figs. 3.1 and 3.2). The first section, the driver, contained the detonable gas. The second section, the test section, was open at the far end and contained ambient air. The pneumatically actuated gate valve was first opened, which triggered the initiation of a detonation that propagated in the driver section of the tube toward the test section. When the detonation reached the interface with air, the detonation products expanded into test section and drove a blast wave toward the open end (see the x-t diagram on Fig. 3.1). Particles near the gate valve were entrained in the flow of expanding detonation products.

The driver was a 6.35-cm-inner-diameter steel tube, 66-cm-long. One end of this tube was closed with a blind flange and equipped with a high-voltage weak spark igniter. The igniter was powered by a 30 kV trigger module. The

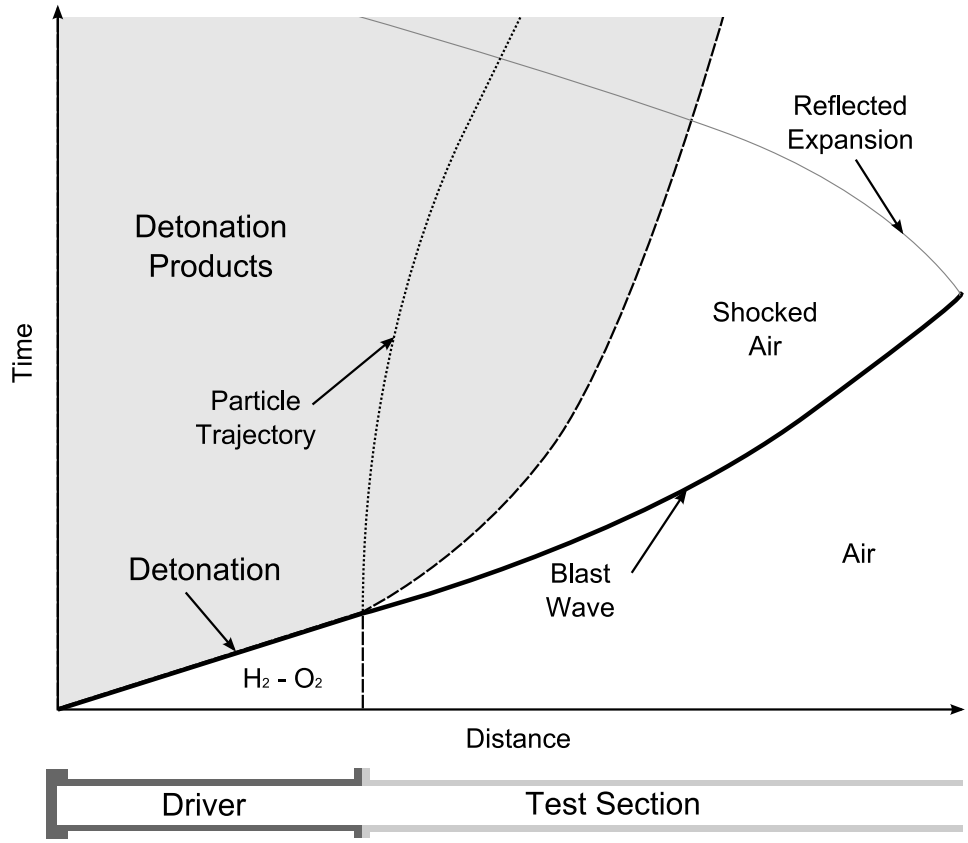

Figure 3.1. Sketch of x-t diagram of flow field

tube was instrumented with two PCB pressure transducers for characterization of the detonation process and determination of time zero. The other end of the tube was sealed by the pneumatically actuated gate valve. The test section was a clear acrylic tube approximately 1.6 m long with its far end open. The driver section was first evacuated and then filled to 1 atmosphere with a stoichiometric mixture of hydrogen and oxygen. The mixture was prepared by an in-line mixing technique with choked orifices to maintain the flow rate constant irrespective of the downstream pressure. The mass flow rates of hydrogen and oxygen were measured with two FVL-1600 mass flow meters

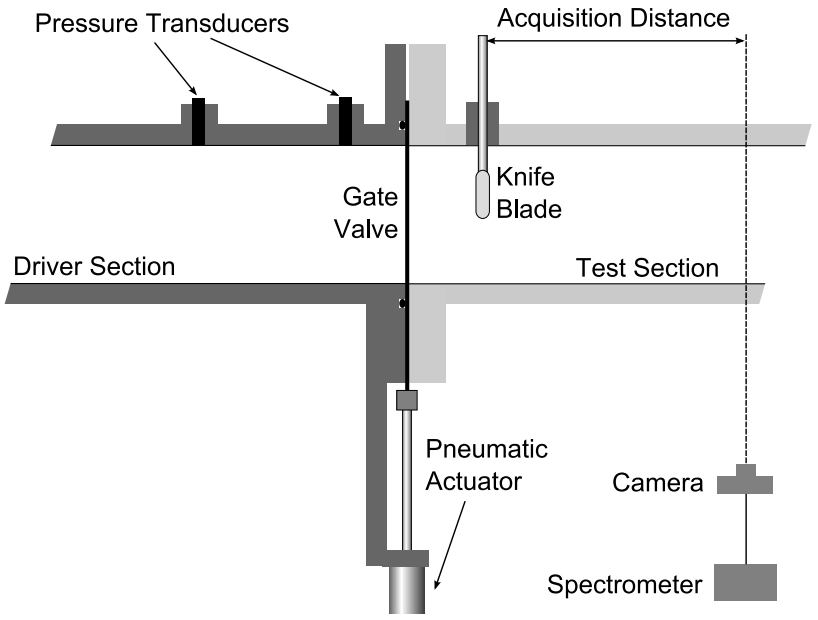

Figure 3.2. Sketch of experimental apparatus

(Omega Eng. Inc.). Metering valves that served as critical orifices allowed precise adjustment of the gas flow rates. The hydrogen and oxygen flows were mixed inside a 150 mL stainless steel cylinder filled with $\frac{1}{4}$ inch stainless steel balls. The quality of the flow control and mixing were verified by measuring oxygen concentration with a NOVA 370 (Nova Analytical Systems Inc., Hamilton, ON) oxygen analyzer. The gate valve was opened (the opening time is less than a second). Upon reaching its fully open position, the gate valve activated a micro switch that triggered the ignition system. After a short run distance, a detonation was formed and propagated through the driver section. Upon arrival of the detonation at the air interface, a blast wave was transmitted into the test section. The particles were introduced into the flow in one of two ways described below: knife edge loading and particle suspension and injection. The particles are entrained into the flow of detonation prod-

ucts and convected into the transparent test section, following the blast and air/products interface, where they can be observed via optical means. For these experiments, the particles do not leave the products, although they can achieve considerable momentum and, as a result, can locally exceed the flow velocity of the decelerating products. Eventually, the blast wave reaches the open end of the transparent tube, and an expansion wave is reflected back into tube, traversing the combustion products and particles.

3.1.1 Knife Edge Loading

In this case, a metal powder sample of approximately 50 mg was placed on a knife edge located near the central axis of the test section, 50 mm downstream of the gate valve. In these types of experiments, a single gate valve was used.

3.1.2 Particle Suspension and Injection

In this case, just prior to the opening of the gate valve, a suspension of the metal powder was injected in the tube. The apparatus was modified to include a double gate valve assembly (see Fig. 3.3). The two gate valves were located 25 mm apart and actuated simultaneously. The two gate valves created a relatively small enclosure in which the powder suspension was injected. This was done in order to have the initial sample of metal powder sufficiently small such that all particles would experience nearly identical flow conditions.

A small volume of pressurized air (approximately 3.5 atm) was used to create the particle suspension in the dispersion system. Upon opening of a solenoid valve, the pressurized air rushed in a small chamber (see Fig. 3.4)

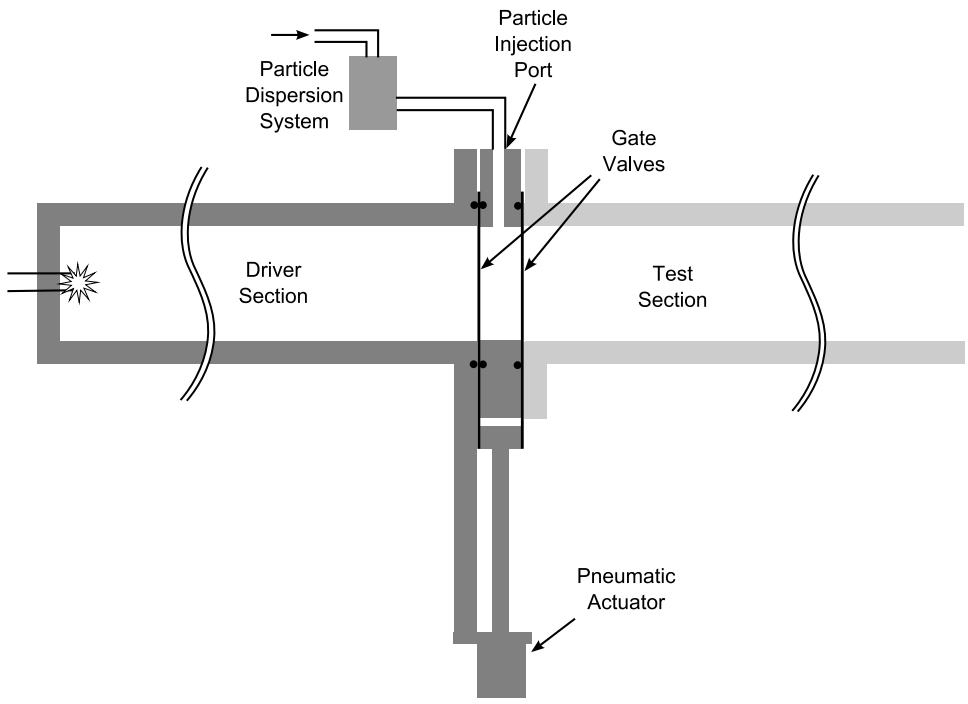

Figure 3.3. Sketch of double gate valve and particle dispersion system

containing the metal powder sample, thus generating the particle suspension. This suspension was then injected into the apparatus in the region confined by the two gate valves described above. After particle injection, both gate valves were opened simultaneously, which then triggered the initiation of the detonation wave.

This technique was developed to overcome the concerns associated with the knife edge loading. First, the presence of the knife edge affects the flow field by generating boundary layers and a wake. While these effects are confined to small regions of the flow field, this is precisely where the particles are injected in the flow. Therefore, it is likely that the particles are accelerated by the flow much more gradually because of the presence of the knife. Furthermore, it

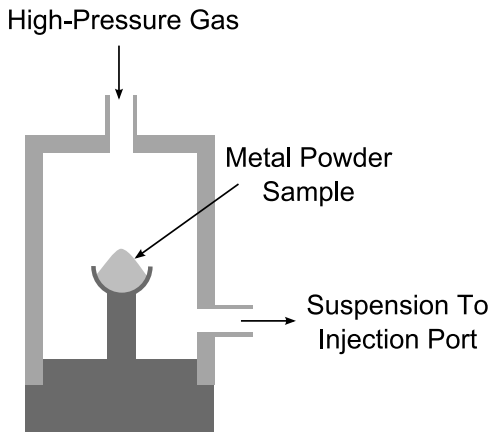

Figure 3.4. Sketch of particle dispersion system

is possible that not all particles leave the knife at the same time. The result may be a long cloud of particles exposed to different flow conditions. These issues make the experimental results difficult to interpret and the modeling much more difficult. By injecting a dispersed cloud of particles between the two gate valves, these problems are overcome. The particle cloud is small such that all particles are exposed to the same flow conditions and there is no knife edge to affect the flow field.

3.2 Metal Powders

Two different metals were investigated in the present study: aluminum and magnesium. The metal powders are described below.

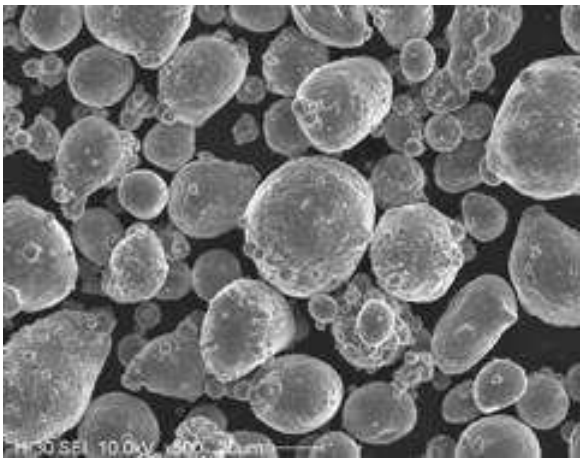

Figure 3.5. Typical Valimet Inc. powders (H50)

3.2.1 Aluminum

Five aluminum powders (from Valimet Inc.) of different particle sizes were investigated: H2, H10, H30, H50 and H95. The approximate mean particle diameters were 2.6, 10.2, 32.8, 49.7 and 109.3 μm for H2, H10, H30, H50 and H95, respectively. Figure 3.5 shows a typical aluminum powder sample (H50). The particles are nearly spherical. The particles have a size distribution, with standard deviation approximately equal to half of the mean diameter. In general, for 80% of the particles the diameter varies by a factor of three (for example, in the case of H10 the mean diameter is approximately 15 μm, and 80% of the particles have a diameter between 7 and 22 μm). Sample distributions are included for H50 and H95 (see Figs. 3.6 and 3.7, respectively).

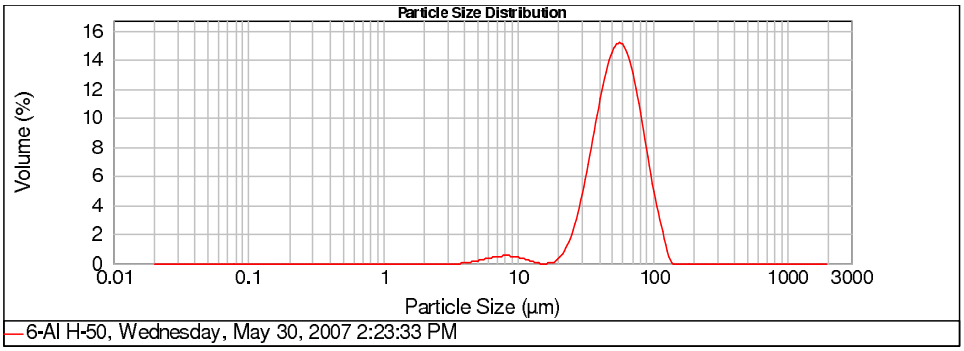

Figure 3.6. H50 particle size distribution

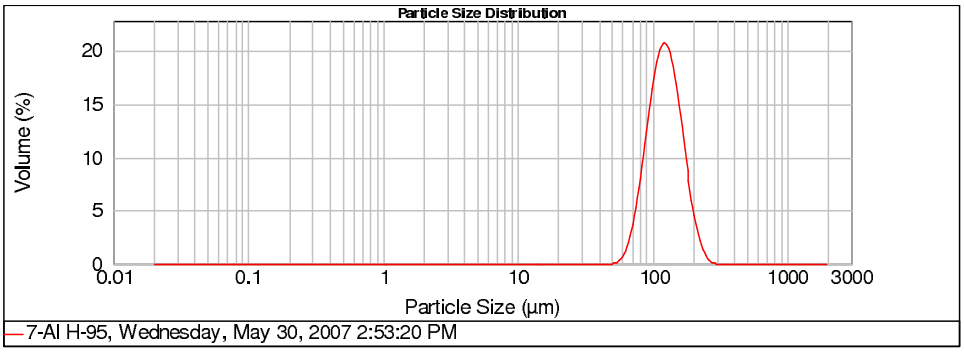

Figure 3.7. H95 particle size distribution

3.2.2 Magnesium

Three magnesium powders (from Reade Manufacturing Co.) of different particle sizes were investigated: GRAN 16, GRAN 12 and GRAN 17. The approximate mean particle diameters were 60, 85 and 240 μm for GRAN 16, GRAN 12 and GRAN 17, respectively. Figure 3.8 is a typical magnesium powder sample (GRAN 12) which shows nearly spherical particles.

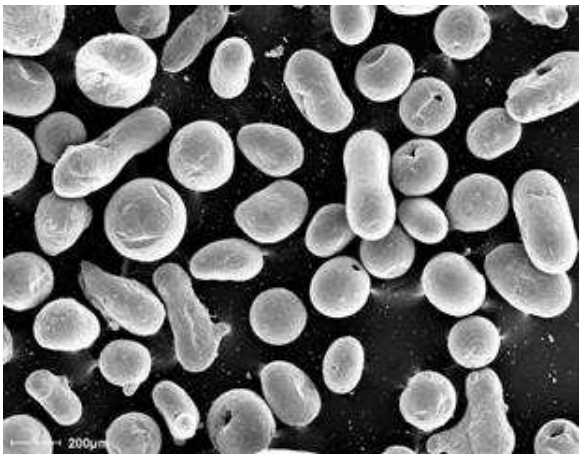

Figure 3.8. Typical Reade Manufacturing Co. powders (GRAN 12)

3.3 Time-Resolved Luminosity

A fast response Thorlabs PDA55 photodiode (12.5 MHz frequency response) was located approximately 2 m from the apparatus. The photodiode was used to obtain time-resolved luminosity history emitted by the reacting particles in the test section. the photodiode was placed sufficiently far from the apparatus such that its field of view was greater than the entire test section. Also, the spatial collection efficiency was verified by slowly translating a known light source along the entire length of the test section. Figure 3.9 shows the result of this test. In reality, the signal was obtained as a function of time (during translation of the light source). On this figure, the time axis has been converted to distance along the test section. Since the translation was not achieved at constant velocity, the distance on the abscissa cannot be considered to be linear. The figure shows that the light intensity signal was nearly constant along the entire length of the test section. The spatial variation was much less than 5%, which was considered sufficiently uniform not to influence the

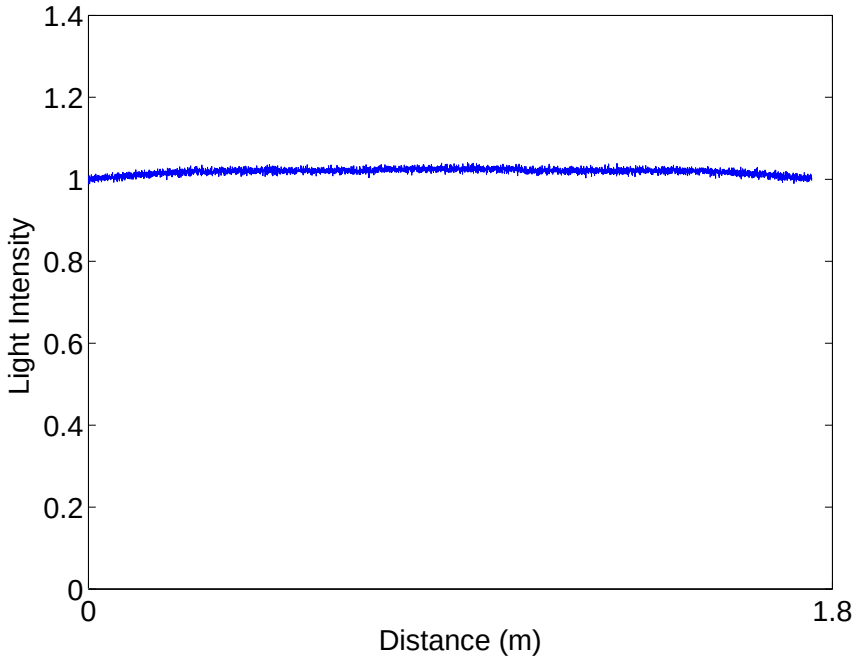

Figure 3.9. Intensity of a known light source as a function of location along the test section

results.

Although the global oxidation of aluminum produces condensed alumina (Al_2O_3), alumina does not exist in the vapour phase. It forms through the process of chemical condensation (condensation-oxidation) [52] of intermediate gaseous oxides, the most prominent of which is AlO. Thus the appearance of AlO molecular spectra can be used for the detection of Al combustion (see Roberts *et al.* [53]). The AlO molecular bands are located in a visible range of wavelengths and have a very sharp short-wave boundary. In the current experiments, a narrow band-pass (10 nm) interference filter with wavelength of approximately 486 nm that coincides with the strongest AlO molecular

band was mounted in front of the photodiode in order to detect aluminum combustion.

3.4 Emission Spectroscopy

In addition, emission spectroscopy was used to measure the temperature of reacting particles. Emitted light was collected by a Canon SLR camera that was focused on the test section located 120 cm away. The distance between the point of acquisition and the gate valve was varied in the study (see Acquisition Distance on Fig. 3.2). A 5-m long, 100-μm optical fibre mounted on the imaging plane of the SLR camera transferred the collected light to a miniature Ocean Optics USB-4000 spectrometer. The estimated spectral resolution of the spectrometer-fibre system was approximately 2 nm. The field of view of the optical system at 120 cm was approximately 3 mm. While the spectrometer's linear CCD array was sensitive in the range of 370-1100 nm, the practical spectral interval was limited to approximately 400-850 nm due to the strong absorption of the acrylic tube in the UV and near IR ranges. All experiments discussed in the present study were done with 100 ms electronic exposure time. This is essentially an open-shutter technique since the duration of the luminous event is approximately 3-5 ms.

The spectral sensitivities of the spectrometer's CCD and optical system are complex functions of wavelength. The cumulative sensitivity function was derived using the factory provided spectral emissivity of an Ocean Optics LS-CAL calibration lamp (tungsten halogen with Teflon diffuser). The spectral transparency of the acrylic tube was determined from the calibrated lamp

with and without the acrylic tube. All results were corrected for the spectral aberrations introduced by the acrylic tube.

Chapter 4

Experimental Results and Discussion

4.1 Luminosity

First, control experiments were performed with no powder and with aluminum oxide. Figure 4.1 shows the typical luminosity signals for these control experiments. Time zero corresponds to an estimate of the time at which the transmitted shock reaches the knife blade. The time it took for the detonation to reach the air interface was extrapolated from the velocity of the detonation measured by the pressure transducers. The time for the transmitted shock to reach the blade was estimated from the transmitted shock strength, which in turn, was calculated using the NASA CEA equilibrium code [54]. This time is on the order of 25-30 μs. The luminosity signals from the control experiments show a small amount of light emitted by the detonation products entering the clear test section. Note that the aluminum oxide and the no powder signals

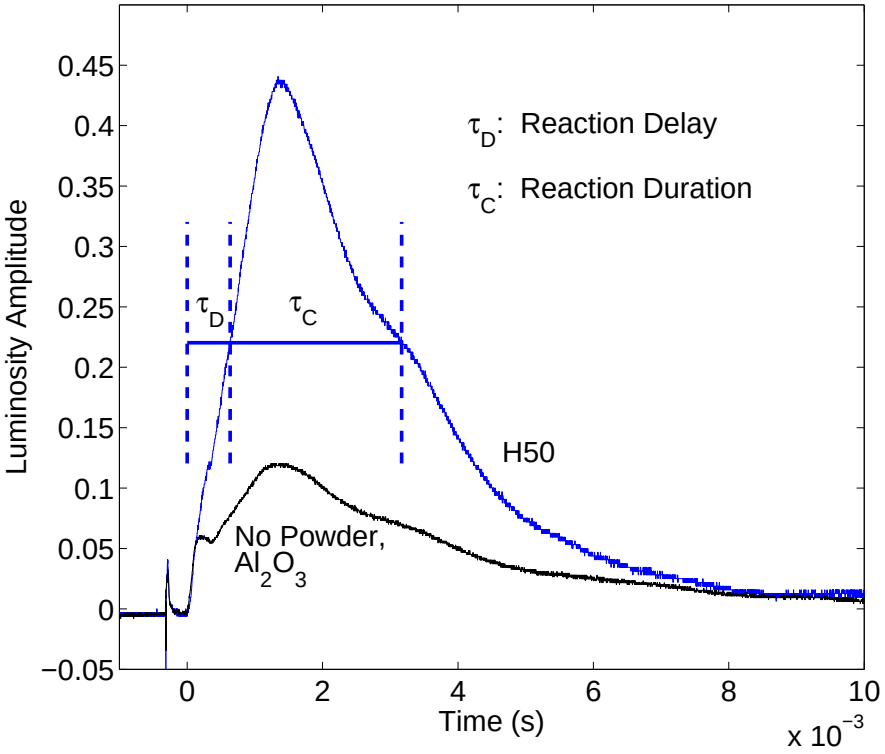

Figure 4.1. Typical luminosity signal of control experiment (no powder or alumina) and H50 sample; also illustrated are the definitions of reaction delay and duration used in the present study

are indistinguishable.

4.1.1 Aluminum

Figure 4.1 also shows a typical photodiode trace obtained with H50 powder. The light emitted by aluminum powder was much more intense than that from control experiments, which indicates chemical reaction of the aluminum with the detonation products (simple black body radiation of hot particles

can be ruled out because the aluminum oxide control did not show as much light). Luminosity was not observed instantaneously from the passage of the transmitted shock wave. However, the delay was quite short (on the order of hundreds of microseconds) depending on the particle size. The signal rise was rather continuous and slow, making it difficult to identify an ignition point and ignition delay. As was done by Roberts *et al.* [53], a reaction delay was defined as the time for the luminosity signal to reach half of its peak amplitude (see Fig. 4.1). Reaction duration was also difficult to identify from the signals and was therefore defined here as the total time during which the luminosity signal exceeds half of its peak value. Figure 4.2 shows a typical luminosity signal for H10, H30, H50 and H95 particles. It is found that all particle sizes investigated showed more luminosity than control experiments, indicating that particles of all sizes chemically react. The amplitude of the signals slightly decreases with increasing particle size (except for H10), presumably because smaller particles have higher specific surface area. All signals are qualitatively similar and do no exhibit signs of sharp ignition.

Figures 4.3 and 4.4 show the reaction delay and duration, respectively (the curves in Figure 4.3 are results of simulations that will be discussed in the next chapter). Both increase with particle size. Note that reaction duration increases approximately as $d^{0.5}$. This contrasts with typical aluminum combustion data from gas burners and reflected shock tubes where the combustion time usually obeys the d^2 law (Beckstead [14] calculates $d^{1.8}$). The small dependence on particle diameter suggests that the particles may be reacting in the kinetic regime. However, in the kinetic regime, one would expect a linear dependence on particle size. This discrepancy may be explained by agglomeration of smaller particles or in the difficulty in defining the reaction duration

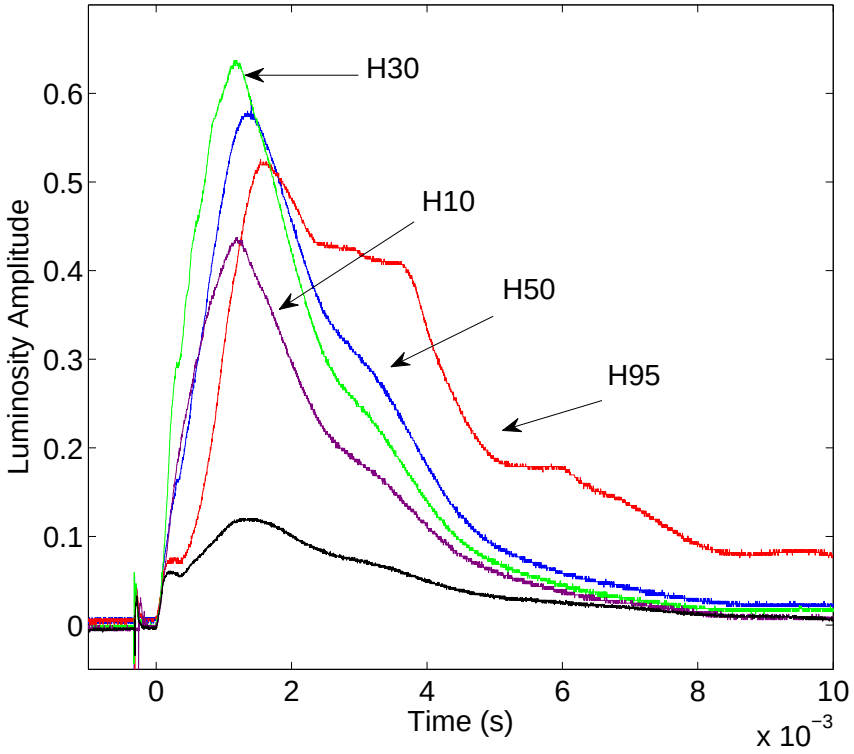

Figure 4.2. Typical luminosity signals of control experiment, H10, H30, H50 and H95

itself. The kinetic regime is also consistent with the fact that no clear ignition event is observed and luminosity shows a continuous increase from time zero (recall that ignition corresponds to the transition between kinetic and diffusive regimes).

Note that all experiments were repeated in test sections of various lengths (1.2-1.75 m). This was done to rule out the possibility that a rarefaction reflected from the open end of the test section was causing the particles to quench (see the x-t diagram on Fig. 3.1). If this were the case, a longer test

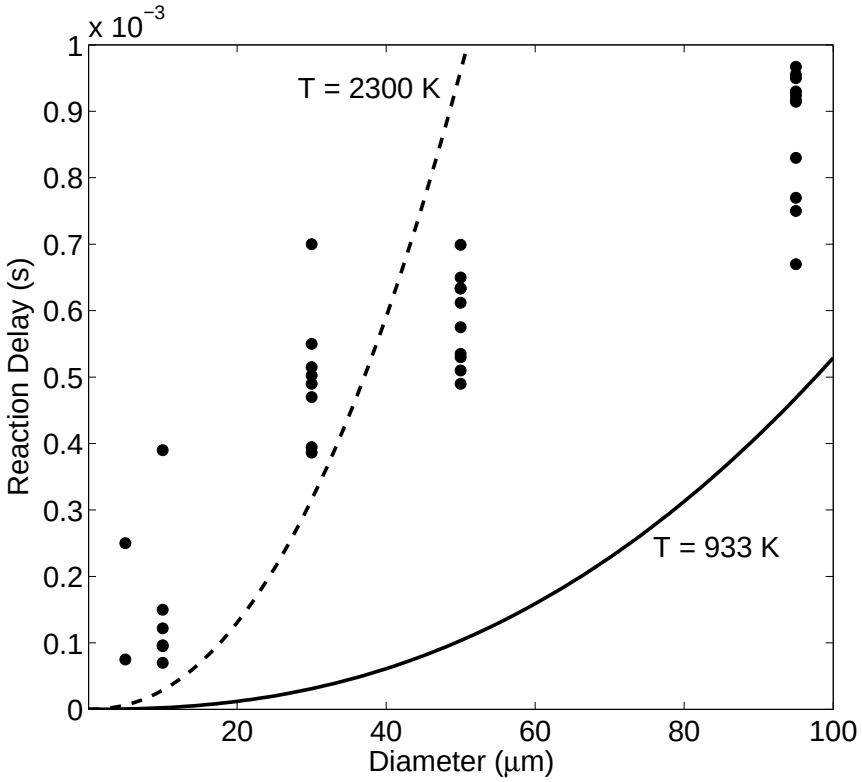

Figure 4.3. Reaction delay of aluminum particles as a function of particle diameter

section should delay the arrival of the rarefaction and increase the reaction duration. The results of both reaction delay and reaction duration were identical for the two test sections, indicating that the particles are not quenched by the rarefaction.

The quantity of metal powder that was used was varied from 25 to 100 mg. The results (reaction delay time and reaction duration) were independent of metal powder mass, at least within the range investigated. Presumably, at higher loadings, the results would show a dependence on concentration as particle - particle interactions become non-negligible. However, at these low

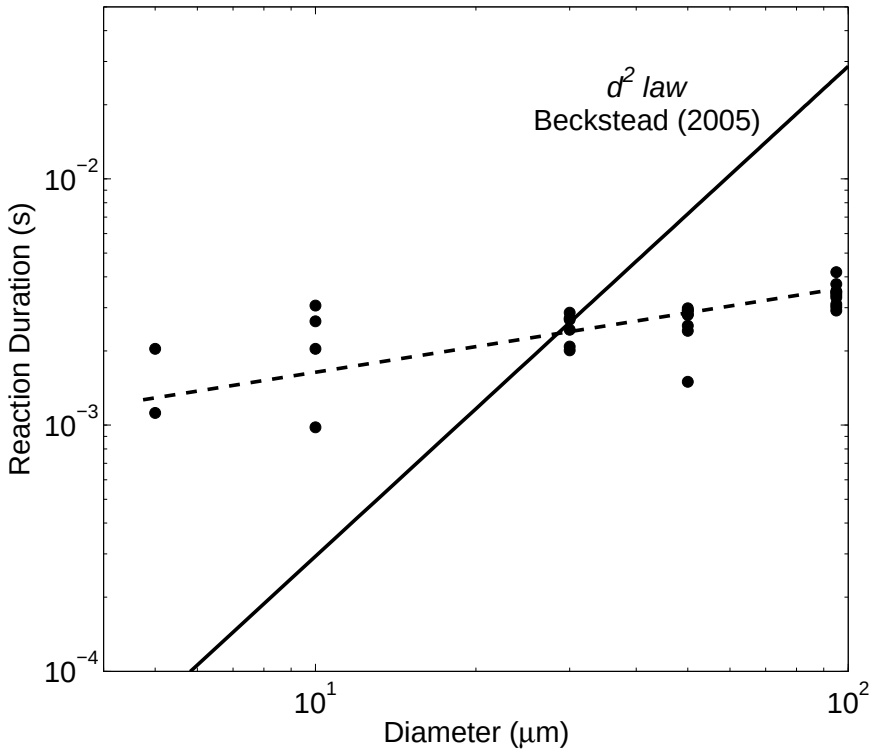

Figure 4.4. Reaction duration of aluminum particles as a function of particle diameter

concentrations, the results showed no such dependence. From this point a mass of 50 mg was used for every subsequent experiment.

As was mentioned in the previous chapter, two methods were used to introduce the metal powder sample in the flow: knife edge loading and particle dispersion and injection between the double gate valve assembly. These two techniques were used and their respective results were compared. Figure 4.5 shows typical luminosity signals obtained with the photodiode using the two techniques with H50 aluminum powder. The luminosity signals generated by

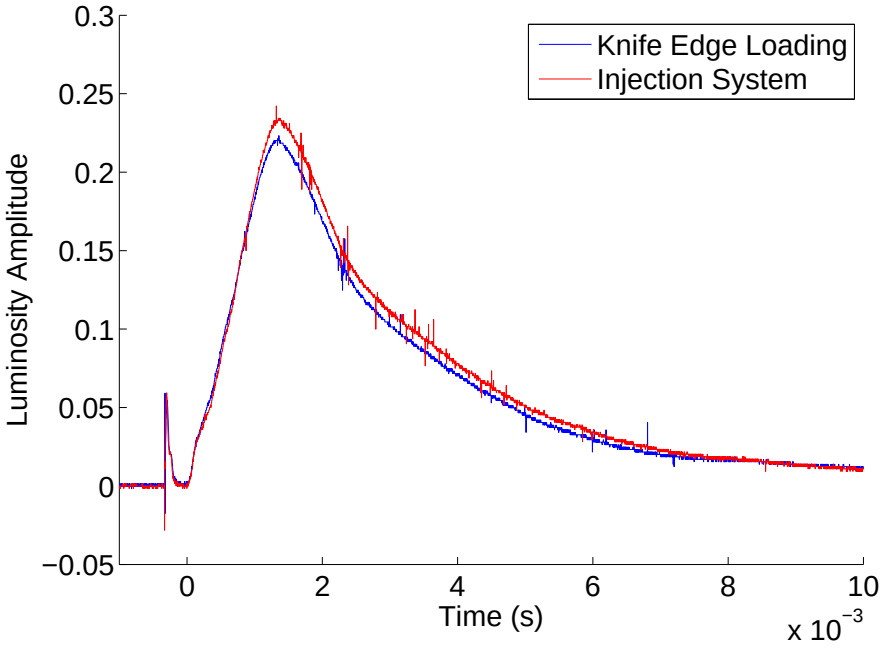

Figure 4.5. Comparison of knife edge particle loading and particle dispersion system for H50 aluminum samples

the two different techniques are nearly indistinguishable and result in nearly identical reaction delays and durations. The fact that the two methods produced such similar results suggested that the flaws of the knife edge loading of particles in the present experiment was not as important as was first suspected. It was therefore considered that the effect of the knife edge could be neglected. For this reason, some of the data that was obtained with the knife edge technique is included in the thesis. However, it should be noted that most of the presented data was obtained with the particle dispersion and injection system.

The length of the detonation driver section was varied. This was done to control the flow gradient behind the detonation. A longer driver section should

have a much shallower Taylor wave [28] (slow rate of expansion of the detonation products) than a short driver section (high rate of expansion). Although the driver was varied in length by more than a factor of three (66 vs. 219 cm), this change had a small effect on the results. The longer driver resulted in a slightly smaller reaction delay than the short driver. However, there was no effect of the driver length on the reaction time (see Figs. 4.6 and 4.7). It should be noted however that even though the Taylor wave is self-similar (its length increases linearly with the advancing detonation and therefore the gradient gets progressively shallower) in theory, it is not the case in practice. In reality, boundary layers become important when the detonation has progressed a sufficiently long distance. In fact, a "real" Taylor wave with boundary layers tends to a steady state. This means that whether the driver is 100 tube diameters or 1000 tube diameters long, the gradient in the Taylor wave is nearly the same. In the present experiment, the drivers are approximately 10 and 35 tube diameters. This may be long enough that boundary layers dominate the Taylor wave and could explain the fact that little difference is observed between the short and long drivers.

4.1.2 Magnesium

Figure 4.8 shows a typical luminosity signal from 85 μm (GRAN 12) magnesium powder. Also on this figure is a control experiment with no powder. The difference in luminosity between the control experiment and the magnesium powder leaves no doubt that the magnesium particles are chemically reacting with the flow. The signal is qualitatively very similar to those obtained with aluminum. It shows no clear ignition (sharp signal rise) or extinction (sharp

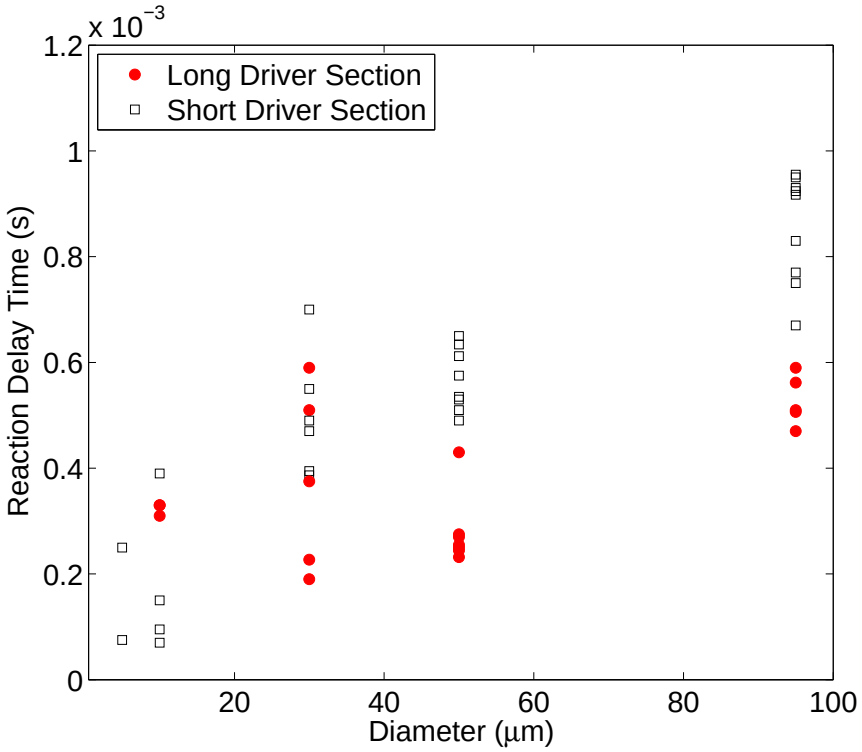

Figure 4.6. Effect of driver length on aluminum particles reaction delay

signal decay). Luminosity increases gradually and smoothly almost instantaneously.

Figure 4.9 shows typical signals for all magnesium powders investigated: 60, 85 and 240 μm. All powders produce significantly more light than the control experiment, indicating that all powders investigated chemically react with the flow. As was the case with aluminum, all traces look qualitatively similar. The only significant difference is the largest particle size (240 μm) which shows a double peak signal. The first peak appears at approximately the same time as those of smaller particle sizes (approximately 1-2 ms). The

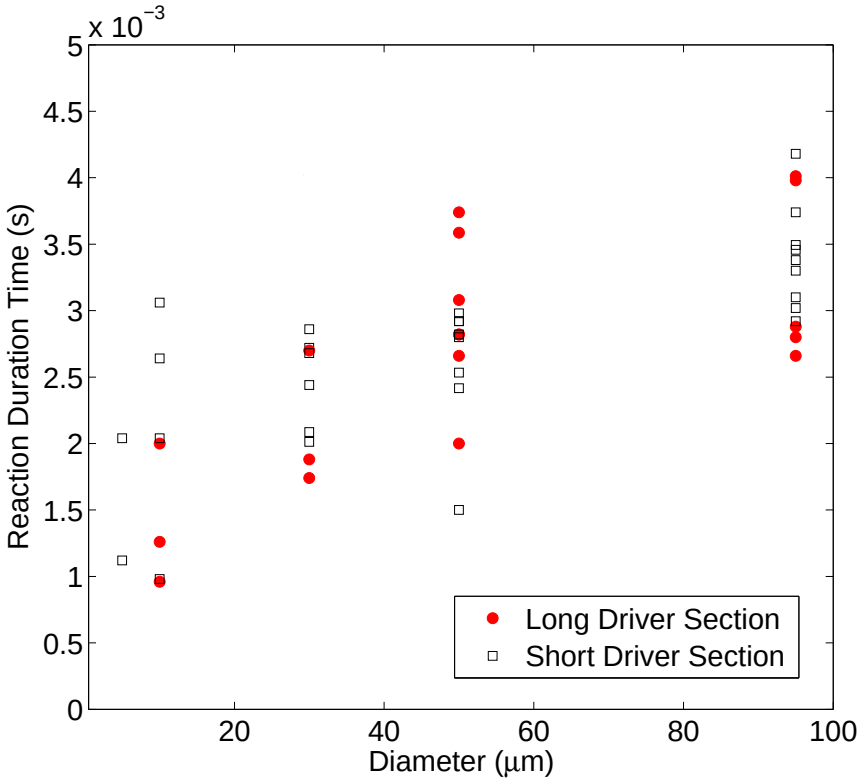

Figure 4.7. Effect of driver length on aluminum particles reaction duration

second peak occurs around 5 ms. This qualitative difference suggests that the particles may be reacting via a different combustion mechanism. Perhaps the smaller particle sizes react in the kinetic regime while the largest particles actually ignite and burn in a diffusively controlled regime. This may explain the difference in the qualitative behaviour of GRAN 17 (240 μm) powder.

The reaction delay and duration are plotted in Figs. 4.10 and 4.11 using the same definitions that were used for aluminum (the curves in Fig. 4.10 are the results of simulations that will be discussed in the next chapter). Both increase with particle size. While the reaction delay appears to increase lin-

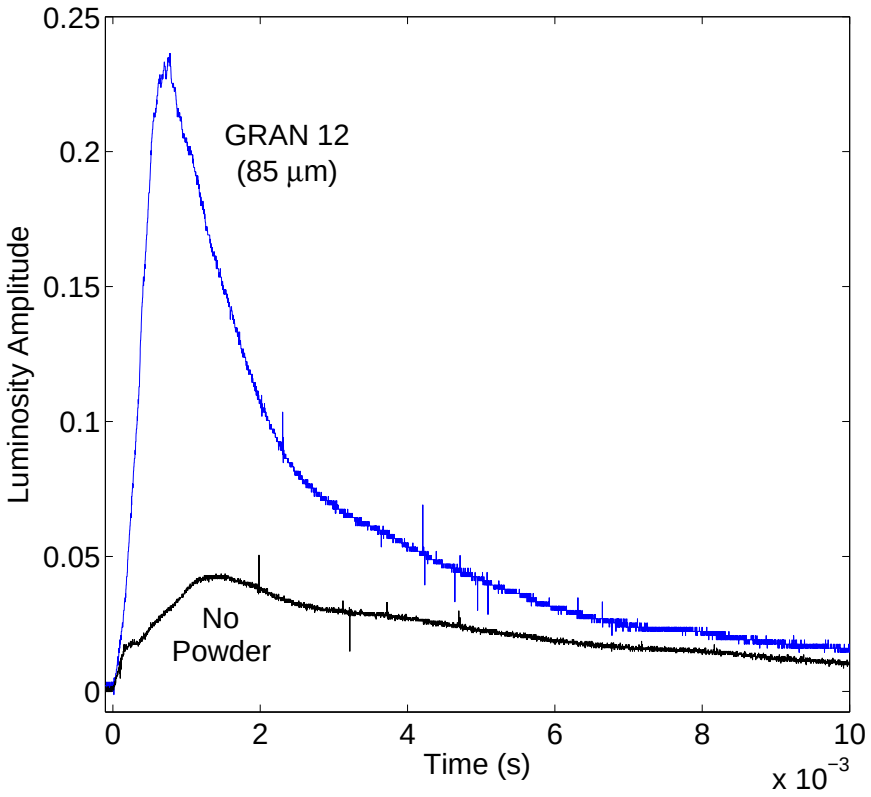

Figure 4.8. Typical magnesium luminosity signal obtained with GRAN 12 powder (85 μm)

early with particle diameter, the reaction duration appears to increase as d^n with n slightly larger than 1. Again, this is in contrast with the conventional diffusion-limited regime where the reaction time should increase with the square of particle diameter. The fact that n is only slightly larger than one suggests that a transition from kinetic to diffusive regimes may be taking place. This is consistent with the two qualitatively different luminosity signals for large and small particles.

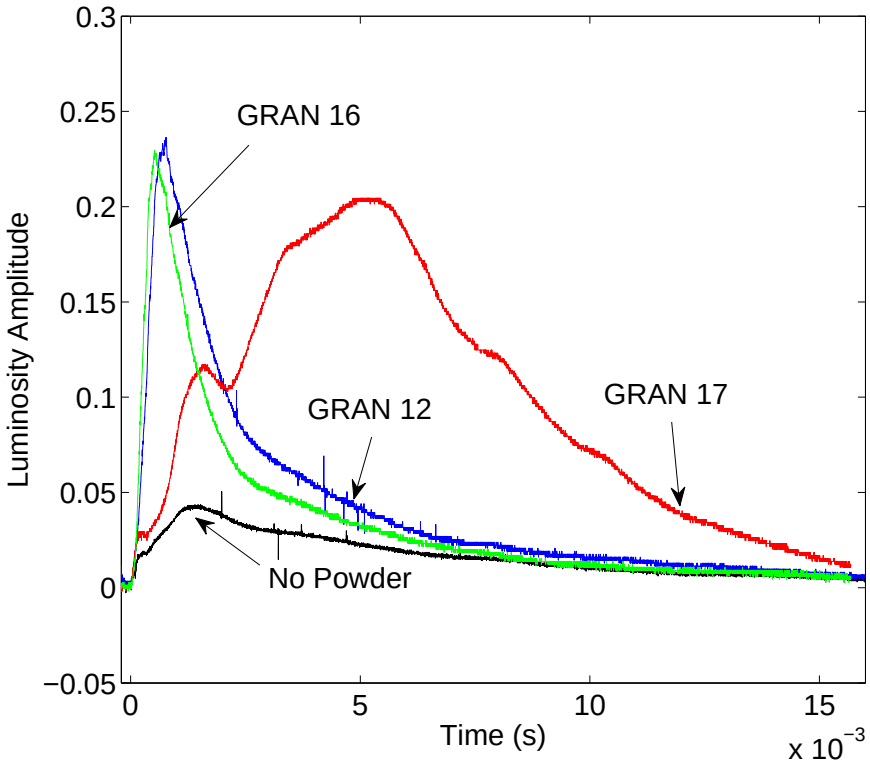

Figure 4.9. Typical magnesium luminosity signals of GRAN 16, GRAN 12 and GRAN 17 powder

4.2 Emission Spectroscopy

To determine the combustion regime of the aluminum particles, it is insightful to estimate the combustion temperature. This was done using emission spectroscopy. Figures 4.12 and 4.13 show the emission spectra of two control experiments: no powder and aluminum oxide (99.9% pure γAl_2O_3, $<$ 0.1 μm) powder, respectively. The "no powder" spectrum shows no continuous background. However, sodium and potassium lines are clearly visible. The aluminum oxide spectrum shows a weak continuous background that is difficult

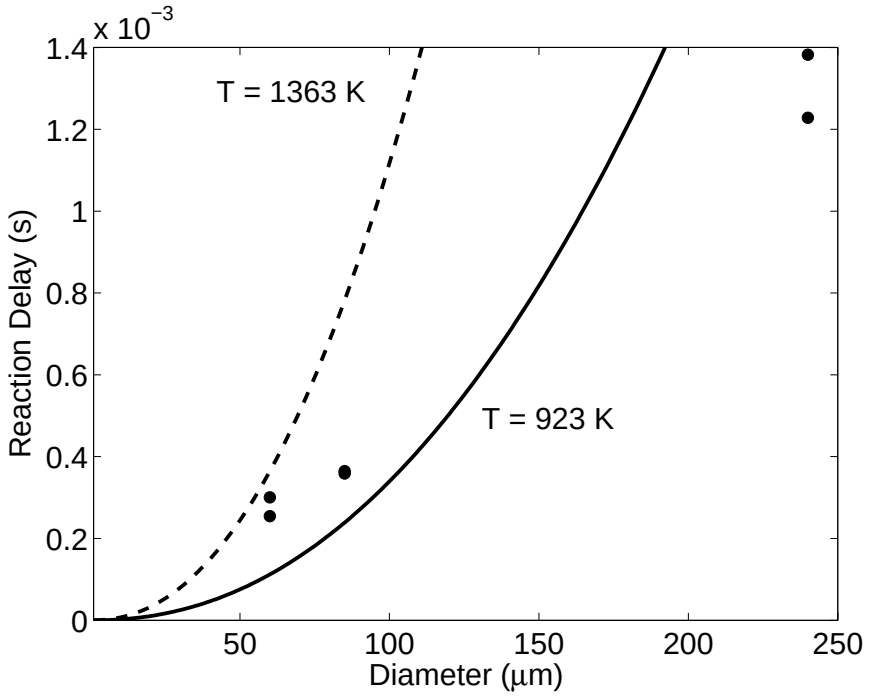

Figure 4.10. Reaction delay of magnesium particles as a function of particle diameter

to separate from a system of lines and bands. It is therefore not possible to estimate temperature from this spectrum.

Figure 4.14 shows a typical spectrum obtained with H50 aluminum powder. The spectrum shows a well developed system of AlO bands in the range of 450-550 nm, superimposed on a strong continuous background. Also visible on this spectrum are the unresolved sodium doublets (589.0 and 589.6 nm) and the partially resolved potassium lines (766.5 and 769.9 nm). Again, the important difference between this spectrum and those obtained from control experiments indicates aluminum combustion with detonation products. It is possible to estimate the temperature of condensed emitters using this spectrum

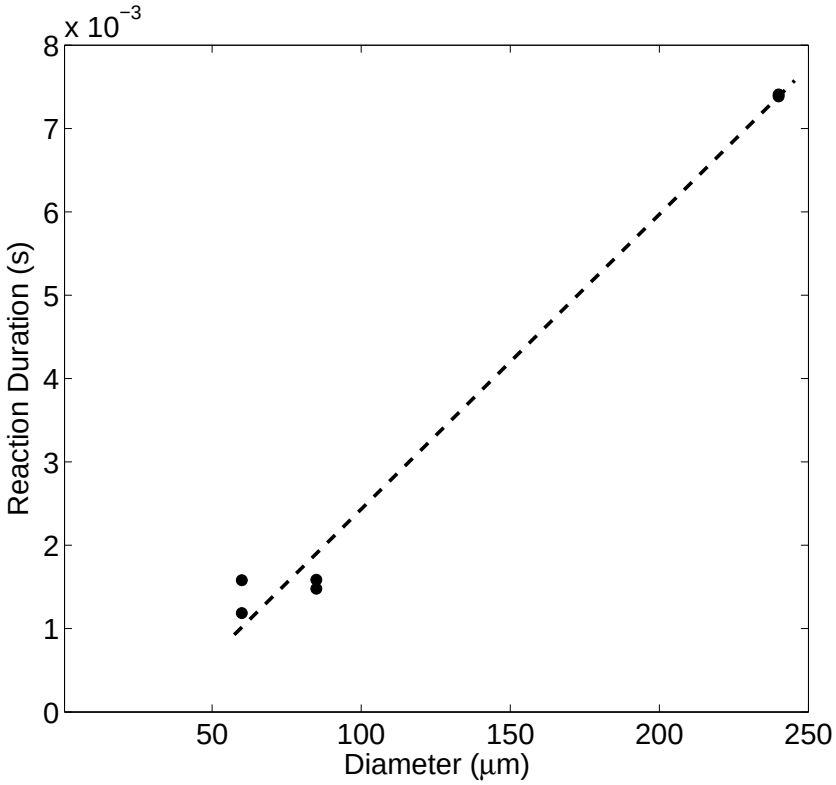

Figure 4.11. Reaction duration of magnesium particles as a function of particle diameter

by polychromatic fitting to Planck's law of black body radiation, which can be rearranged in the following form:

$$\ln\left[\frac{i(\lambda,T)\lambda^5}{\epsilon(\lambda,T)2hc^2}\right] = \frac{hc}{kT}\frac{1}{\lambda} \tag{4.1}$$

where i is the intensity, ϵ is the emissivity of the condensed emitter, λ is the wavelength, h is Planck's constant, k is Boltzmann's constant, c is the speed of light and T is temperature. In the case of aluminum combustion, the main condensed emitter is likely to be the nano-size ($\leq$ 100 nm) aluminum oxide formed as a result of further oxidation of gaseous aluminum suboxides (AlO,

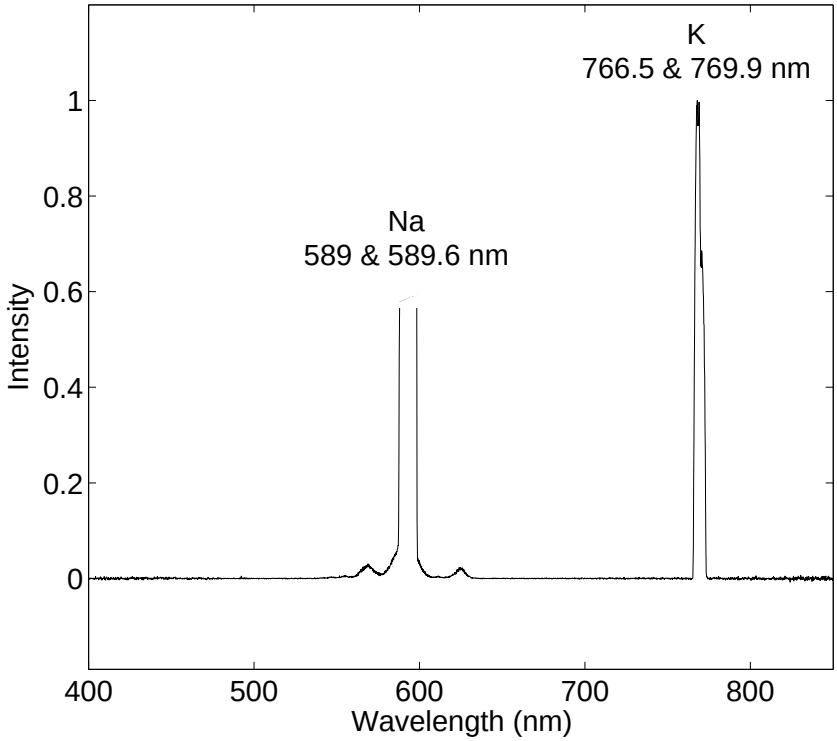

Figure 4.12. Emission spectrum of a control experiment with no metal powder

AlO_2, etc.). To obtain the temperature, one must know how the emissivity of the emitter varies with wavelength. Unfortunately, the emissivity has not been experimentally measured in the conditions of interest.

However, for such small particles (smaller than the wavelength), the emissivity is inversely proportional to the wavelength (Rayleigh limit [55]). Furthermore, according to Parry and Brewster [56] the absorption index of molten aluminum oxide is also inversely proportional to the wavelength in the 400-1000 nm range, suggesting that the spectral emissivity of the oxide particles is inversely proportional to λ^2, as is done by Goroshin *et al.* [15] and Bazyn [57].

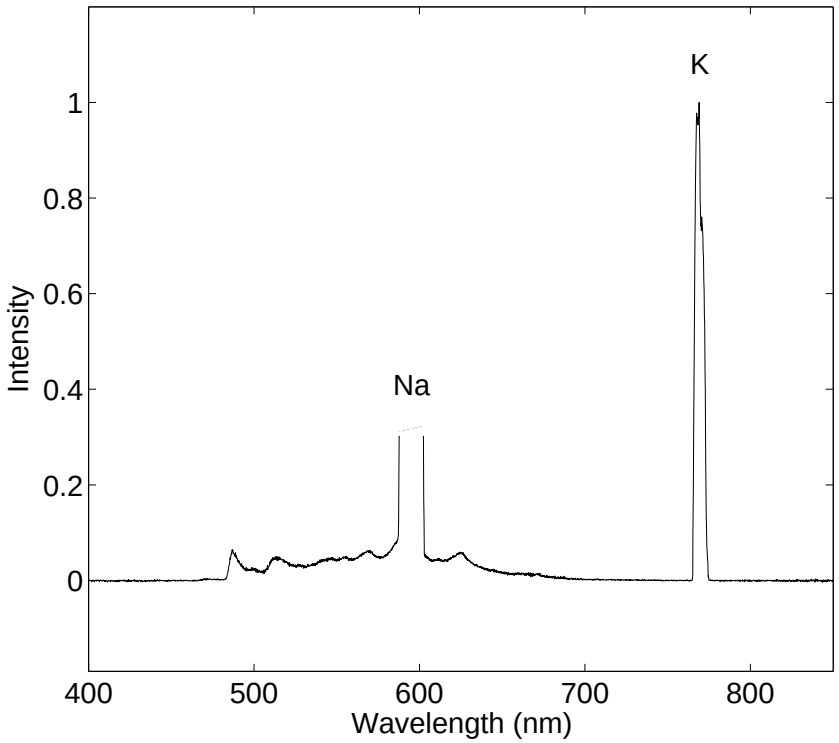

Figure 4.13. Emission spectrum of a control experiment with alumina (Al_2O_3)

If this is the case, a good linear fit should be obtained when plotting $\ln(i\lambda^7)$ as a function of $\frac{1}{\lambda}$. The slope of this straight line is inversely proportional to temperature. Unfortunately, with this technique, the temperature is fairly sensitive to the emissivity function, while the quality of the fit is not. In other words, the quality of the linear fit to the data is not an adequate means to verify the emissivity model (for example, the fit is almost as good for $\epsilon \sim \lambda^{-1}$ as it is for λ^{-2} while the resulting temperatures are significantly higher). For these reasons, the temperatures obtained with this technique should be considered as estimates. Since the objective here is not to determine the exact

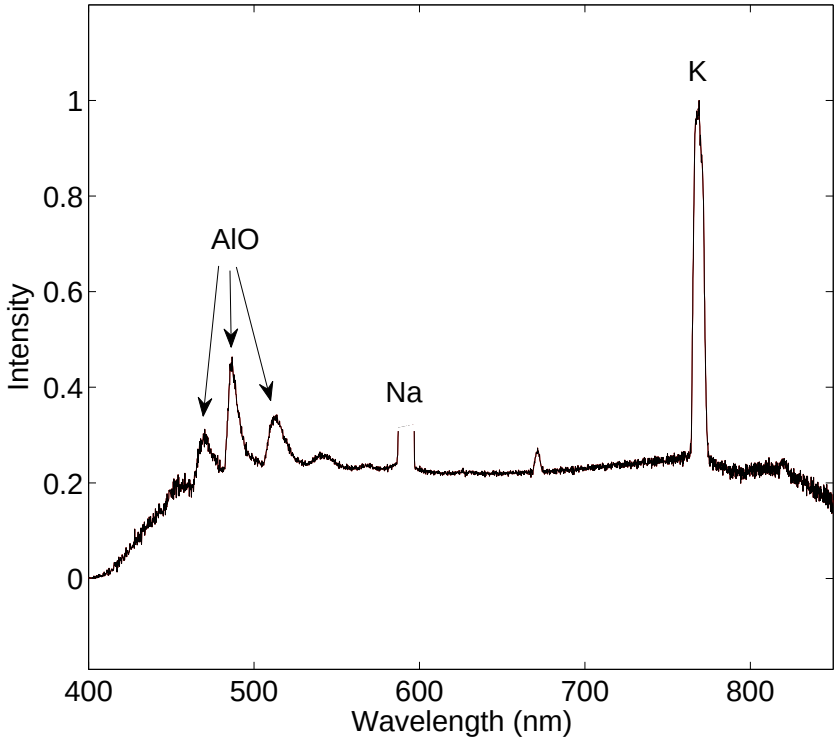

Figure 4.14. Emission spectra of a 50 mg sample of H50 aluminum powder

temperature but to determine if the temperature is much higher than, or approximately equal to the flow temperature the results are considered to be meaningful.

Indeed, it is found in all cases with aluminum powder that a good linear fit can be obtained in the range of 630 to 760 nm (region clean of lines and bands). Figures 4.15 and 4.16 is a typical spectrum fit to Planck's law. This procedure was done for every experiment with aluminum powder. Due to the strong dependence of the spectral intensity with temperature, the calculated temperature can be attributed to the maximum temperature of the condensed

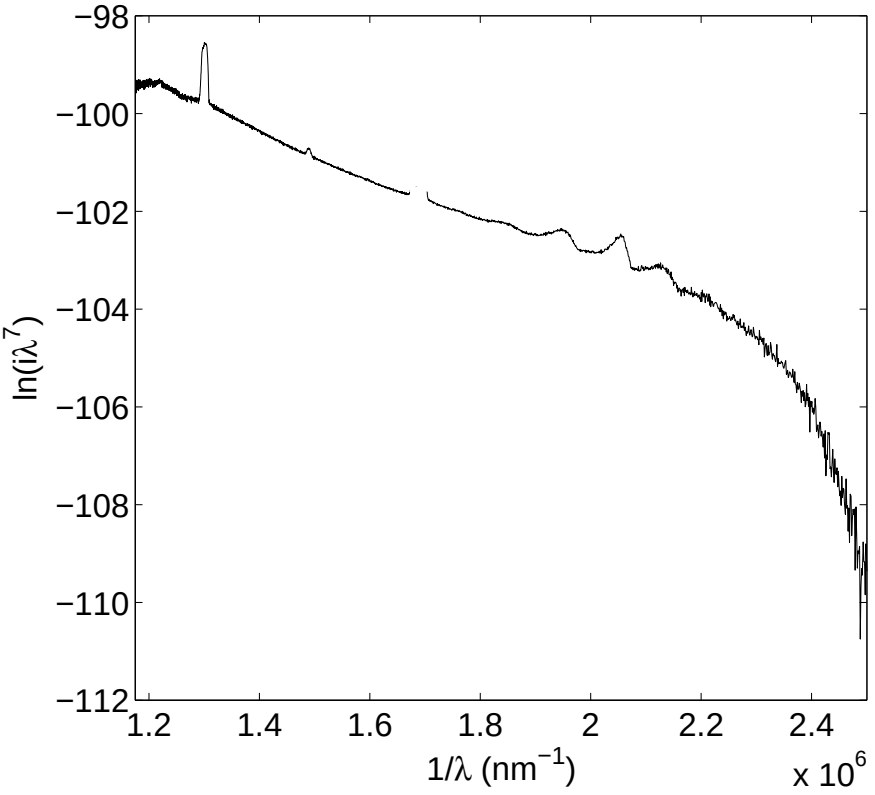

Figure 4.15. Polychromatic fitting of typical spectrum obtained with H50 aluminum powder

emitter during the time of acquisition of the spectrometer.

Emission spectra were obtained for all aluminum particle sizes at different distances along the test section. The temperature was calculated from each spectrum and is plotted in Fig. 4.17. While there is considerable scatter in the temperature estimates, most data points lie between 2200 and 2800 K with a trend slightly increasing with distance. Note that this temperature range is near the aluminum boiling point of 2792 K. There appears to be no difference between particle sizes as all the temperature measurements overlap. Also

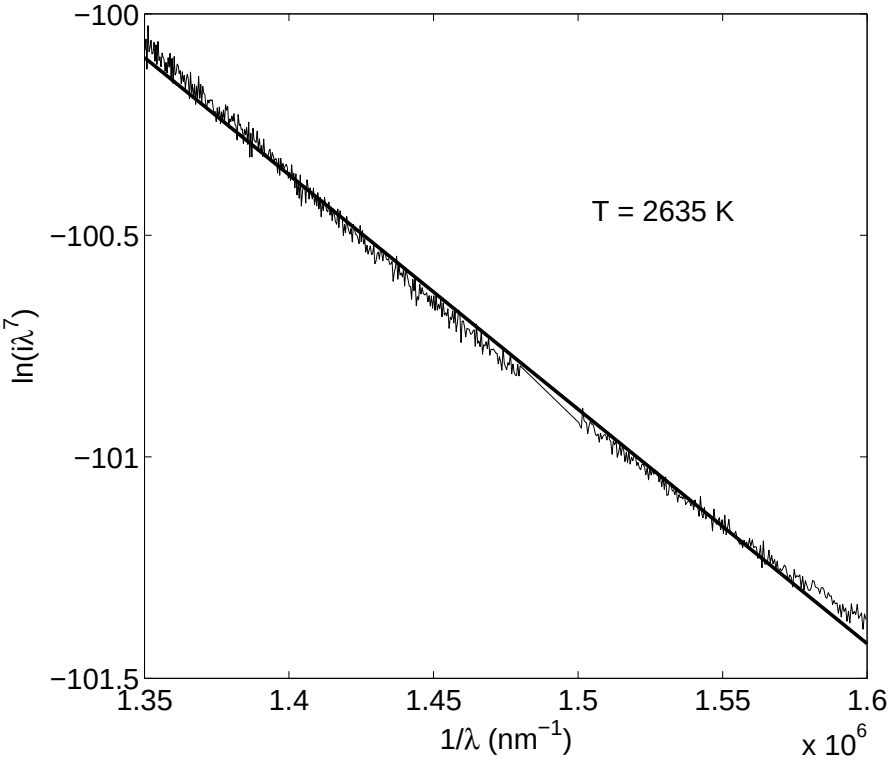

Figure 4.16. Polychromatic fitting of typical spectrum obtained with H50 aluminum powder in the region clear of lines and bands

shown on this figure is the flow temperature experienced by a 50-μm particle as it travels through the test section. This curve was obtained from numerical simulations using an Euler code that will be described in Chapter 5. Note that particles of different sizes are subjected to different flow temperatures but this difference is so small (less than 100 K difference for 2 and 100 μm particles) that only a single curve was included for clarity of the figure. Also plotted on Fig. 4.17 is the adiabatic flame temperature for a stoichiometric mixture of aluminum and water vapour at the flow temperature. The adiabatic flame temperature was calculated using NASA's CEA chemical equilibrium

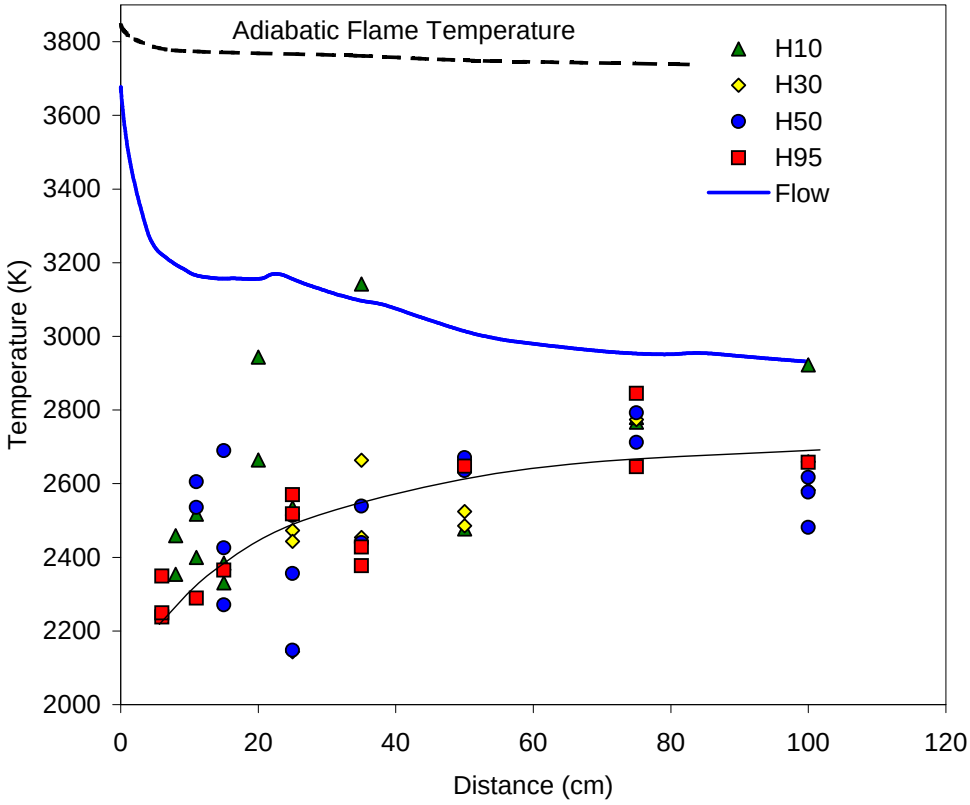

Figure 4.17. Temperature measurements obtained by emission spectroscopy as a function of distance along the test section for various aluminum powders

code [54]. Most temperature measurements lie well below both the adiabatic flame temperature and the flow temperature. One might expect that toward end of the test section, the temperatures should tend to the flow temperature, since chemical reaction is over and the particles have had sufficient time to thermally equilibrate with the flow. This may indicate that the $\epsilon \sim \lambda^{-2}$ may not be correct. It is found that $\epsilon \sim \lambda^{-1}$ results in temperatures that are approximately 350 K higher, much more consistent with the flow temperature. In both cases, the temperature estimates are not significantly above the flow temperature, and therefore suggest kinetically controlled combustion.

Chapter 5

Model for Gaseous Explosives

The following is an attempt to model the particle unsteady heating in the present experimental conditions. The flow field is computed with an Euler CFD code. Subsequently, particles are introduced in this flow field and their trajectories and heating histories can be calculated by solving ordinary differential equations. It is assumed here that the particle does not affect the flow field. This assumption is justified by the small particle loading in the experiments [27].

The objective of this modelling effort is to contribute to the interpretation of the experimental results. The simulations can be used to investigate some of the models and ignition criteria that were discussed in Chapter 2.

5.1 Model of the Flow Field

An Euler CFD code, Solver II [58], was used to model the detonation products' unsteady expansion flow field. The simulation was started when the detonation just reached the air interface. The initial conditions were calculated analytically by solving the self-similar Taylor wave [28]. The Euler code treated the products as perfect gases with constant specific heat capacities. It should be noted that these assumptions tend to overestimate the flow temperature.

5.2 Model of Particle Kinematics

A single particle was then introduced in this unsteady flow field. The small particle loading in these experiments justifies the assumptions that the particle does not affect the flow field and there are no particle-particle interactions. The simulation was stopped when the particle reached its boiling point. Thus, the particle diameter was kept constant throughout the simulation. Newton's second law governs the particle dynamics with aerodynamic drag as the only force considered (gravity and other components of the drag force such the carried-mass term, pressure gradient term and the Basset force can all be neglected [27]):

$$m\frac{\mathrm{d}v_p}{\mathrm{d}t} = \frac{1}{2}C_D A_{CS}\rho_f \left|u_f - v_p\right|\left(u_f - v_p\right) \tag{5.1}$$

The drag coefficient is generally a function of Reynolds number. In this study, the correlation by White [59] was used:

$$C_D = \frac{24}{\mathrm{Re}} + \frac{6}{1+\sqrt{\mathrm{Re}}} + 0.4 \tag{5.2}$$

5.3 Model of Particle Heating

The particle exchanges heat with the flow via convective and radiative heat transfer. Exothermic chemical reactions also contribute to the energy of the particle. In general, conduction of heat inside the particle must be considered. However, when the Biot number (ratio of convective heat transfer to the particle to conductive heat transfer within the particle) is small (Bi < 0.1), the temperature distribution inside the particle may be considered to be uniform; see Holman [60], for example. In this case, a lumped capacitance approach can be used and is an important simplification of the problem. The Biot number is defined as:

$$\mathrm{Bi} = \frac{hd}{6k_s} \tag{5.3}$$

The worst case scenario (Biot number is maximum) occurs when heat transfer is maximum and the particle is large. Convective heat transfer in the present problem will be maximum just behind the detonation front (temperature and relative flow velocity are maximum at this point). At this point, largest particles considered in this study had a Biot number of approximately 0.03. This means that temperature gradients in the particle were negligible and therefore, a lumped capacitance approach was used in this model. The resulting energy balance for a particle is given by the following:

$$m\frac{\mathrm{d}E_p}{\mathrm{d}t} = \pi d^2 \left[h(T - T_p) + \epsilon\sigma(T^4 - T_p^4) + kQ\right] \tag{5.4}$$

In the unsteady term, the particle internal energy was used rather than its temperature to account for phase changes. Temperature could then be computed

from the internal energy in the following manner:

$$T_p = \frac{E_p}{c_v} \tag{5.5}$$

$$\text{for } E_p < E_{mp} = c_v T_{mp} \tag{5.6}$$

$$T_p = T_{mp} \tag{5.7}$$

$$\text{for } E_{mp} < E_p < E_{mp} + \Delta h_f \tag{5.8}$$

$$T_p = T_{mp} + \frac{E_p - E_{mp}}{c_v} \tag{5.9}$$

$$\text{for } E_{mp} + \Delta h_f < E_p < E_{bp} = E_{mp} + c_v(T_{bp} - T_{mp}) \tag{5.10}$$

5.3.1 Convective Heat Transfer

The convective heat transfer coefficient can be obtained from the definition of the Nusselt number:

$$\text{Nu} = \frac{hd}{k_f} \tag{5.11}$$

Empirical heat transfer correlations relate the Nusselt number to the Reynolds number, Prandtl number, etc. Whitaker [36] gives the following correlation for spheres:

$$\text{Nu} = 2 + \left[0.4\text{Re}^{\frac{1}{2}} + 0.06\text{Re}^{\frac{2}{3}}\right] \text{Pr}^{0.4} \left[\frac{\mu_\infty}{\mu_w}\right]^{\frac{1}{4}} \tag{5.12}$$

It was assumed here that the viscosity ratio to the power of $\frac{1}{4}$ is equal to unity. It was not necessary to include compressibility effects in the convective heat transfer analysis. The Mach number of the flow relative to the particle is maximum just behind the detonation. Even though the flow of detonation products leaving the detonation is sonic in the detonation reference frame, the particle at rest in the fixed reference frame is exposed to subsonic flow.

Since the particle temperatures considered are relatively low, radiation was neglected.

5.3.2 Heterogeneous Surface Reaction

At a finite temperature, a metal particle in an oxidizing environment undergoes chemical reaction at its surface. Of course, the rate of reaction depends on the nature of the oxidizer and its pressure as well as the surface temperature (exponential dependence on temperature). In the problem of interest, the oxidizing environment is complex. Although the detonation products are mostly H_2O, important amounts of other species (H_2, OH, etc.) are also present (see Appendix A for the full equilibrium composition of the gas mixture). Nevertheless, an attempt is made here to assess its importance. The rate law was assumed to be Arrhenius in form:

$$k = k_o \exp\left[\frac{-E_a}{RT}\right] \tag{5.13}$$

As pointed out by Trunov *et al.* [20], the values of k_o and E_a vary considerably in the literature. In this study, the values selected for use in the model were taken from Roberts *et al.* [53]. These were fit to reflected shock tube experiments in pure oxygen and are presumably an order of magnitude estimate of heterogeneous surface reactions. While the oxidizing gas is different, Beckstead [14] suggests that there is only a factor of 2 in combustion time between pure oxygen and water vapour. The heat of reaction was also taken from Roberts *et al.* [53].

5.4 Model Results

5.4.1 Aluminum

Figure 5.1 is an x-t diagram that shows the trajectories of the blast wave, the contact surface and 30, 50 and 100 μm particles. As anticipated, smaller particles get entrained in the flow more quickly than larger particles. The particle trajectories stop when the particles reach the boiling point. Naturally, this occurs faster for smaller particles. Figure 5.2 shows the temperature of four particles as a function of time. All particles are first heated to the melting point, take a certain time to melt completely, before being heated to the boiling point. This figure clearly shows that smaller particles are heated at a much higher rate than larger particles. Finally, Fig. 5.3 shows the relative velocity between the flow and the particle as a function of time. This velocity starts out at nearly 1200 m/s and quickly drops off and oscillates between $\pm$200 m/s. Larger particles take a longer time to come to mechanical equilibrium with the flow.

Figure 4.3 showed experimental results of reaction delay as a function of particle size. Also illustrated on this figure are two curves obtained from the model, representing the time at which the particles reached the melting points of aluminum and aluminum oxide. In the case of small particles, the experimental delay was longer than that predicted by either model. This may be due to particle agglomeration or wake effects downstream of the blade which may be more important for small particles. For large particle sizes, these two curves essentially bracket the experimental data, suggesting that most of the chemical reaction occurs before the oxide layer melts. It is interesting to

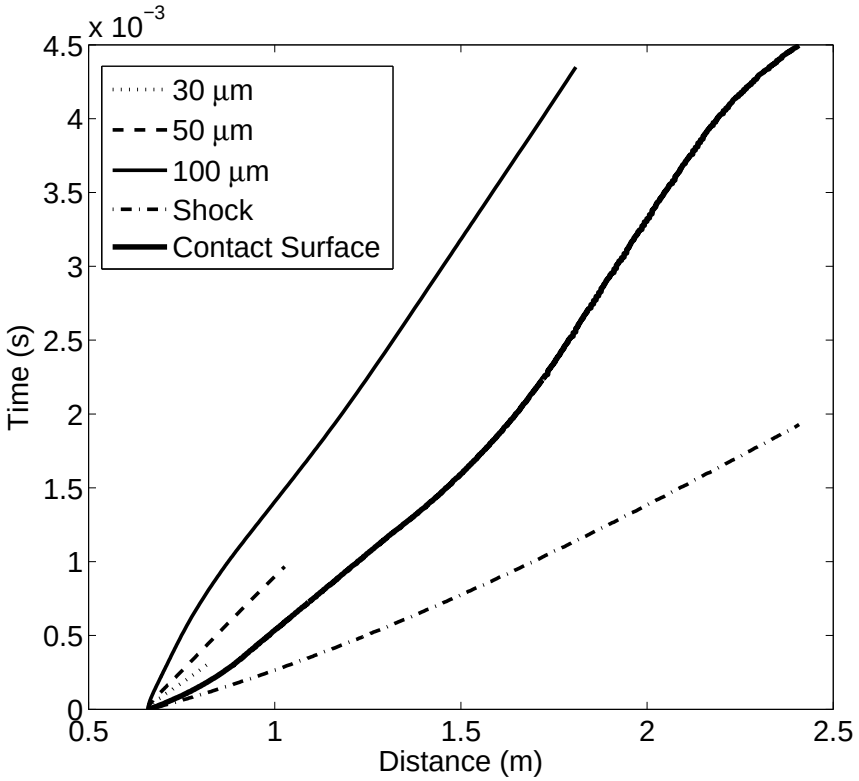

Figure 5.1. x-t diagram showing calculated trajectories of 10, 30, 50 and 100 μm aluminum particles

note that while the experimental data appears to be more or less linear, the model predicts that the heating time to reach any given temperature should be proportional to d^2. However, it is recognized that there is significant scatter in the experimental data.

Finally, the model does predict the heating time within one order of magnitude. It should be noted that the modeling includes estimates of some important parameters such as the drag coefficient in a highly transient flow and transport properties of the detonation products. Unfortunately, the results

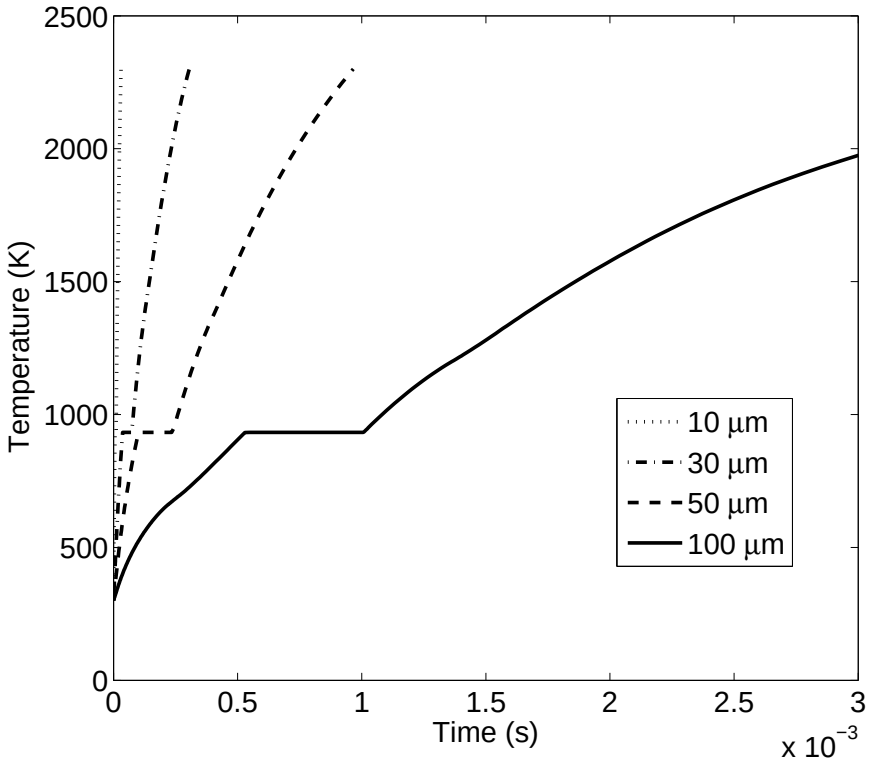

Figure 5.2. Calculated particle temperature as a function of time for 10, 30, 50 and 100 μm aluminum particles

are quite sensitive to many of these parameters and therefore, quantitative uncertainty also exists with the results.

5.4.2 Magnesium

Figure 5.4 is an x-t diagram that shows the trajectories of the blast wave, the contact surface and 60, 85 and 240 μm particles. As was the case for aluminum, the particle trajectories stop when the temperature reached the boiling point

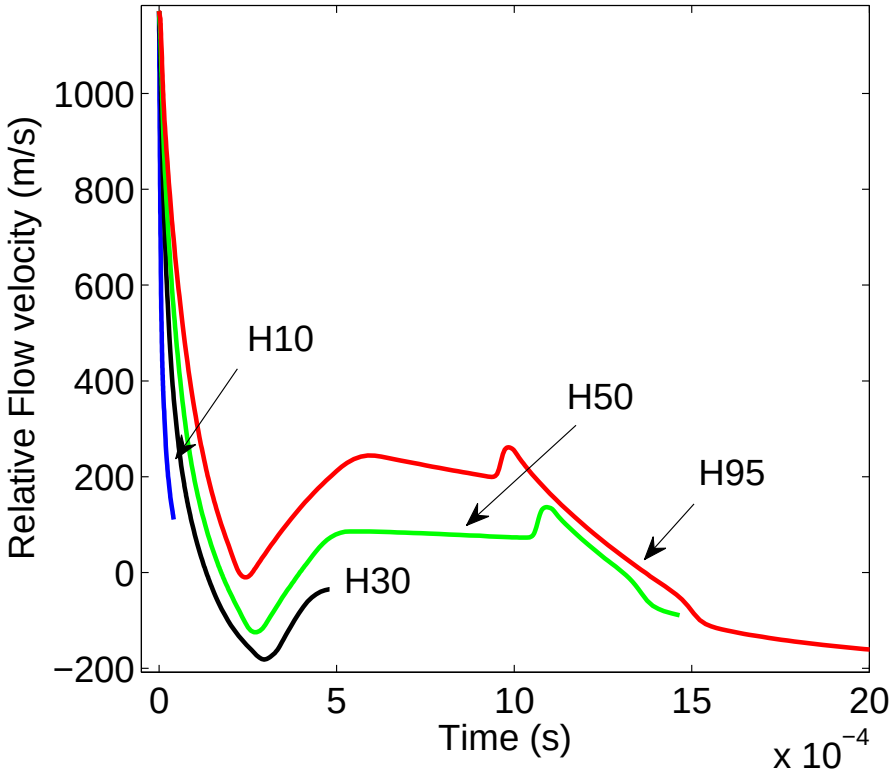

Figure 5.3. Calculated relative flow velocity as a function of time for 10, 30, 50 and 100 μm aluminum particles

of magnesium. Figure 5.5 shows the temperature of the four particles as a function of time. Finally, Fig. 5.6 shows the relative velocity between the flow and the magnesium particles. This is very similar to the results obtained for aluminum.

Figure 4.10 showed experimental results of reaction delay as a function of particle size. Also illustrated on this figure are two curves obtained from the model, representing the time at which the particles reach the melting and boiling points of magnesium. In the case of small particles, the experimental

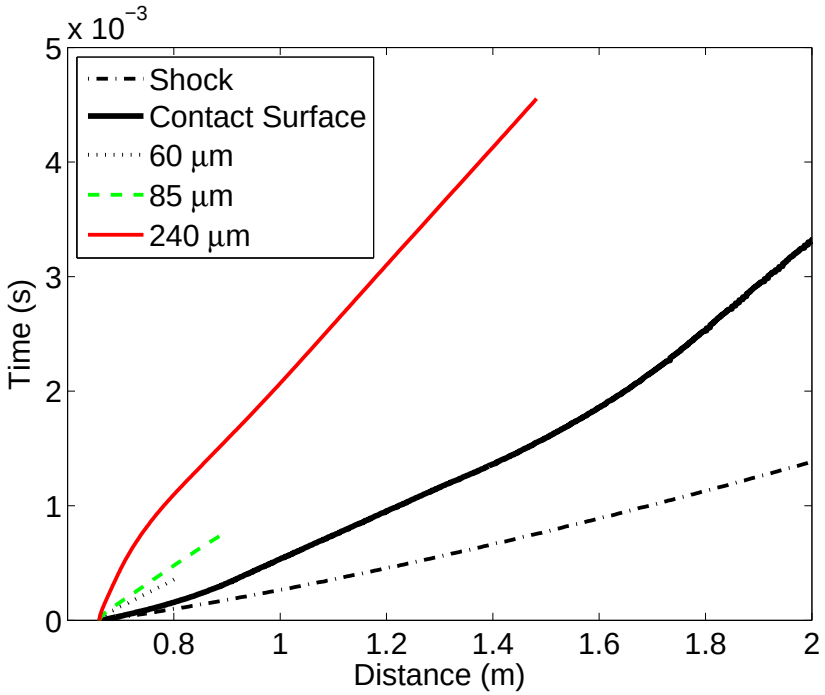

Figure 5.4. x-t diagram showing calculated trajectories of 44, 60, 85 and 240 μm magnesium particles

delay is bound by both criteria. For large particle sizes, the experimental data lies below the melting point curve. It is interesting to note that while the experimental data appears to be more or less linear, the model predicts that the heating time to reach any given temperature should be proportional to d^2. Finally, it is difficult to measure the reaction delay time or define a sharp criterion for it.

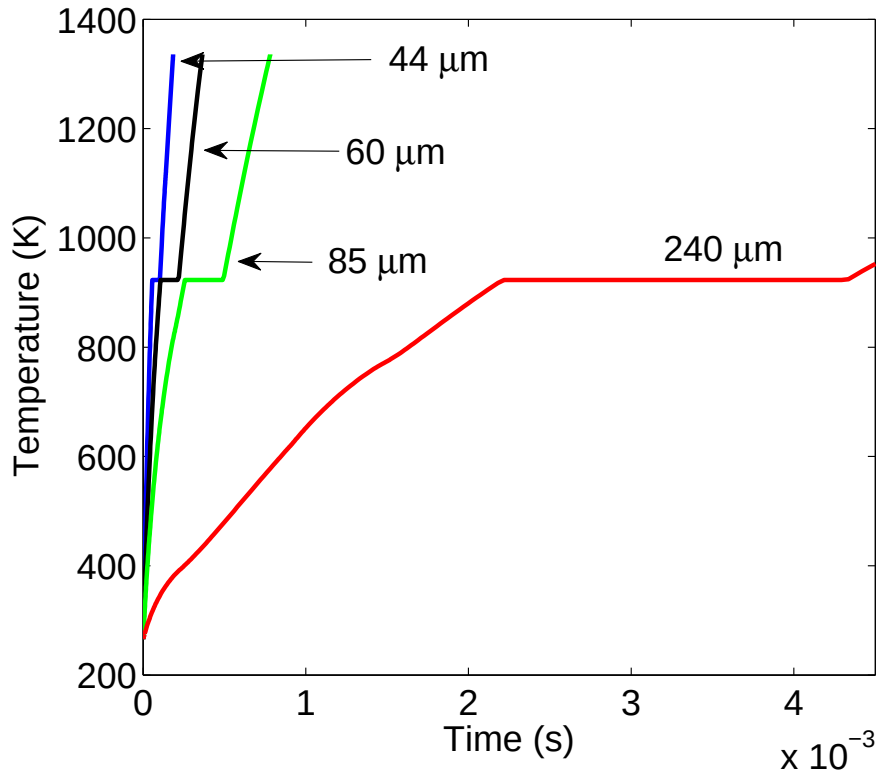

Figure 5.5. Calculated particle temperature as a function of time for 44, 60, 85 and 240 μm magnesium particles

5.5 Discussion

An Euler CFD code was used to calculate the unsteady flow field of expanding detonation products. Particles were then introduced in this flow field and their trajectories and heating histories were calculated. The model first shows that the delay to reach any temperature approximately scales as d^2. However, experimentally, the reaction delay was found to be proportional to d^n, with n approximately equal to 1 for magnesium and slightly less than 1 for aluminum. However, the magnitude of the delays appeared to be approximately in the

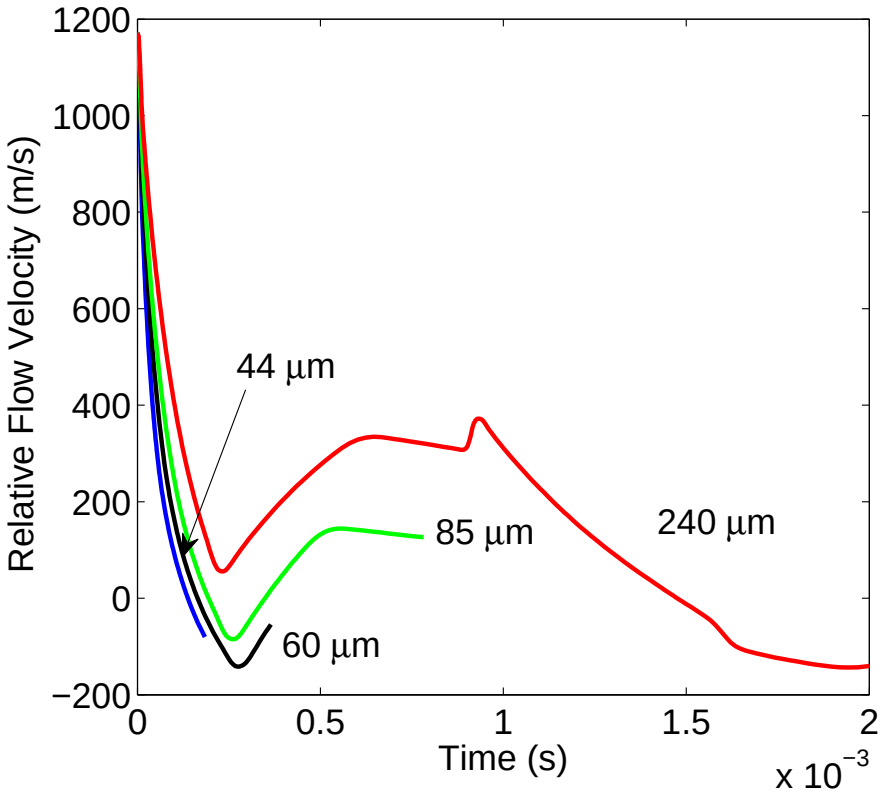

Figure 5.6. Calculated relative flow velocity as a function of time for 44, 60, 85 and 240 μm magnesium particles

right order of magnitude with the different criteria for ignition (melting and boiling points). The fact that the trends agree so poorly with experiments suggests that an effective ignition temperature may not be an appropriate criterion. In fact, it is possible that ignition is not taking place at all. In other words, the poor agreement with experiment is consistent with the hypothesis of particle combustion in the kinetically-controlled regime. Recall that in this regime, there is no ignition because there is no transition to a diffusion-limited regime. Furthermore, in the absence of an ignition event, the arbitrary

definitions of reaction delay and duration (for experimental results) have little significance. It is not surprising that these quantities do not behave exactly as the calculated values.

Recall from Section 2.3 that this model was used to investigate the film stripping mechanism. In this mechanism, the reaction delay should be the time to reach the metal melting point. This criterion was already investigated and found to agree poorly with experiment. However, the film stripping simulations also provided a reaction duration. The reaction duration for this mechanism was found to be proportional to d^2 (again in poor agreement with experimental results). Furthermore, the magnitude of the duration was much lower than experimental reaction duration (particularly for small particles). It is therefore concluded that this mechanism is not responsible for the observed experimental results.

Chapter 6

Model for High-Explosives

As was mentioned in the Introduction, the addition of reactive metals to high-explosives in order to increase the total energy release of the explosive is now common practice. In principle, the total energy output can be increased by the combustion of the metal particles.

Recall the recent experimental results by Frost *et al.* [2], [3], [4] conducted with packed beds of aluminum and magnesium particles saturated with sensitized liquid nitromethane. This work has shown that there exists a critical charge diameter for "prompt" reaction of the expanding metal particle cloud. If the charge is smaller than this critical diameter, then "delayed" reaction is observed (defined by the authors as being of a timescale too long to contribute to the blast wave, typically above 1 ms). With even smaller charges, particles remain completely inert (non-reactive). Sub-critical (delayed reaction) charges produce blast waves approximately one order of magnitude weaker than super-critical charges with prompt uniform reaction throughout the particle cloud. Between the super-critical and sub-critical reaction regime, there

exists a transition regime in which prompt reaction occurs at discrete locations of the particle cloud, while the blast strength varies between the two limits. For both spherical and cylindrical charges, the critical diameter for particle ignition (CDPI) is found to depend on the particle size, morphology, mass fraction and material. For spherical magnesium particles the CDPI increases with increasing particle size (Frost *et al.* [2]). The phenomenon is more complex for spherical aluminum particles and therefore, the present model will mainly focus on magnesium particles. Aluminum will only briefly be addressed in Section 6.2.2.

To date, multi-phase computational fluid dynamics (CFD) models have been used (Frost *et al.* [3], [4], Zhang *et al.* [5], Ripley *et al.* [6], Milne *et al.* [7], Cooper *et al.* [8], Massoni *et al.* [9], Kim *et al.* [10], etc.) to predict the conditions for metal particle reaction in explosives. Mesoscale modelling with hydrocodes is also widely used (Frost *et al.* [11], Ripley *et al.* [12], Zhang *et al.* [13], Milne *et al.* [7], etc.). While such models can, in principle, model a great amount of detail in the phenomena of interest, it would be highly desirable to develop an analytic model that captures the key elements of the problem in a way that makes the dominant features easily discernible.

Therefore, the objective of the present study is to adopt an alternative approach to develop a highly simplified analytical model. This model should incorporate the minimum details necessary to capture the governing physical processes that determine the basic concept of critical charge diameter for ignition and reaction of the particle cloud in a given explosive dispersal event and elucidate the essential phenomena that determine the CDPI. Unlike the model described in the previous chapter for products of gaseous detonations, the following model is for metal particles in the detonation products of con-

densed phase explosives. Therefore, the approach taken is different and does not involve CFD simulations.

First the flow field generated by the high-explosive detonation products is modelled in a highly idealized manner: the products are treated as a perfect gas (with $\gamma = 3$) expanding into a vacuum, in a planar geometry. Due to these approximations, the flow field can be solved completely analytically (see Stanyukovich [26]). Much insight can be gained into the phenomenon of the problem in this manner. Metal particles are then introduced in this flow field and their trajectories and convective heating histories can be calculated by solving simple ODE's. The model assumes that the particles do not affect the flow field. This one-way coupling assumption is valid for a small particle loading in the high-explosive (see Rudinger [27] for example). The particles could be viewed as a small perturbation to the flow field that would exist in the case of a homogeneous charge (i.e., a charge without particles). This is not the case for the experimental data obtained by Frost *et al.* [3], [4] used for comparison with this model, which used packed beds of particles. Nevertheless, the simplicity of the model makes the exercise worthwhile.

Subsequently, more realistic models are developed for the Taylor wave [28] region: spherical geometry, Jones - Wilkins - Lee (JWL) [29] equation of state, etc. Of course, with these more realistic features, a smaller portion of the flow field solution can be computed analytically. Finally, the analytical model results suggest further simplifications of the problem in order to obtain a fully analytical scaling law for the CDPI as a function of particle size. The analytical scaling law will be derived in the next chapter.

The present model has a number of shortcomings due to the simplify-

ing nature of the assumptions made. Further, considerable uncertainty exists in a number of parameters invoked in developing the model (e.g., transport properties of high-pressure, high-temperature detonation products). Yet, the very simplicity of the model (straightforward integration of ordinary differential equations) permits the sensitivity of the results to these assumptions and other features of the model to be quickly and easily assessed.

6.1 The Model

Consider the schematic picture of a reactive particle contained in a spherical high-explosive during an explosive dispersal event (see Fig. 6.1). First, the detonation front interacts with the particle, perhaps raising its temperature and imparting momentum. Then, the particle is further accelerated and heated in the Taylor wave and in the subsequent non-simple wave regions. Large and/or dense particles may have sufficient inertia to penetrate the rapidly decelerating contact surface (product - air interface). In fact, in some cases, the particles may even penetrate the blast wave. At any time, particles are subject to a drag force due to their relative velocity with respect to the flow. Particles also experience heat exchange with the flow through both convection and radiation and are also heated by exothermic heterogeneous chemical reaction taking place on their surface. At some point, the particles may ignite (thermal run-away) at which point the reaction rate is governed by diffusion of oxidizer to the particle surface. The manner in which these various phenomena are dealt with and incorporated in the present model is described in detail in the following sections.

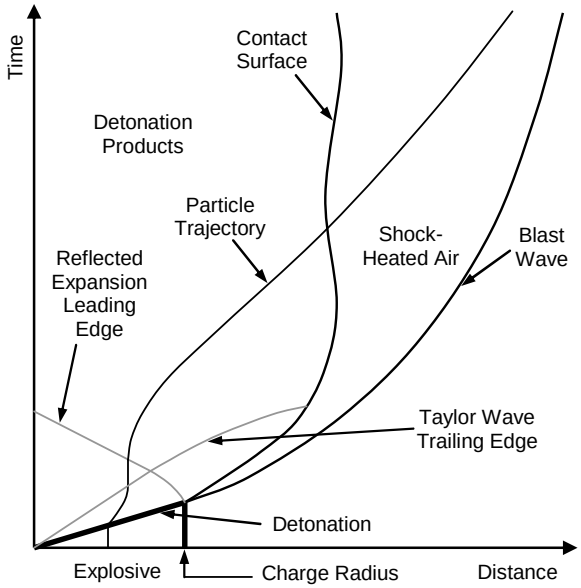

Figure 6.1. Sketch of x-t diagram showing metallized explosive detonation flow field

It should be noted that the objective for the model is to predict whether particle ignition will occur given a particular particle and charge size. No consideration is made here as to the effect of this extra energy release on the blast wave. It is hoped that this model will provide insight into the scaling laws that govern the particle ignition phenomenon and lead to a better understanding of enhanced blast explosives.

6.1.1 Model of Particle - Detonation Interaction

The propagation of a detonation through a packed bed of particles saturated with a liquid explosive is non-ideal, due to losses of heat and momentum to the solid particles (Lee *et al.* [61], Lee *et al.* [62], Milne [63], etc.). In the present model, however, a single particle is considered. In other words, it is assumed

Table 6.1. Chapman-Jouguet properties of nitromethane detonation

Property	Value
V_{CJ}	6150 m/s
u_{CJ}	1667 m/s
c_{CJ}	4483 m/s
T_{CJ}	3580 K
ρ_{CJ}	1591 kg/m^3
A	249.28 GPa
B	5.05 GPa
C	1.29 GPa
R_1	4.72
R_2	1.11
ω	0.38

that the particle has no effect on the flow field. Therefore, the detonation is considered to be an ideal discontinuous Chapman - Jouguet (CJ) detonation (see Fickett and Davis [29] for example) in pure nitromethane. The CJ state of the products is obtained with a chemical equilibrium code, Cheetah 2.0 [64] and is included in Table 6.1.

Detailed modelling of shock/detonation interaction with solid particles (Milne [63], Zhang *et al.* [65]) has shown that significant momentum transfer to the particle occurs during this interaction. For light metals such as aluminum and magnesium, considerable velocity is imparted to the particle immediately behind the shock front, such that its velocity may be 60-100% of the post-detonation flow velocity. During the shock/detonation interaction, considerable particle temperature is also achieved up to 25-30% of the post-detonation flow temperature (Ripley *et al.* [12]). In the present model, the particle will be prescribed an arbitrary initial velocity upon crossing the detonation front. This velocity will be varied to assess the importance of this

momentum transfer to the overall phenomenon.

The detonation front is a compression wave that raises the pressure on the order of 10 GPa. At this pressure, metal particles cannot be considered as rigid bodies. In fact, Zhang *et al.* [65], Ripley *et al.* [12] and Milne [63] have done detailed numerical simulation of the interaction of a detonation with metal particles which shows that particles undergo severe plastic deformation during the passage of the detonation wave and can fragment under certain failure criteria. This can have important consequences on the phenomenon. For example, it can affect the kinematics of the particle by changing the drag coefficient. It can also affect particle heating and combustion by increasing the surface area and compromising the physical integrity of a protective oxide shell on the particle. Gilev [46] and Gilev and Anisichkin [47] conclude that the passage of the detonation destroys the oxide film on aluminium particles by observing an increase in electrical conductivity of the detonation products. This protective oxide film has an important effect on ignition properties. In the present model, however, the particle will be assumed to remain spherical. As for any effect on the oxide layer, it will be accounted for by the choice of ignition temperature (see Section 6.1.8).

6.1.2 Model of Detonation Products Expansion Flow Field

The flow of the expanding detonation products is in general a highly complex problem. While the Taylor wave (Taylor [28]) immediately behind the detonation is a self-similar, simple wave region, the flow subsequent to the detonation reaching the edge of the charge is a non-simple wave region. This

flow depends on the blast wave decay and the region of shock-heated air, which is not homentropic (there are spatial entropy gradients) because of the decaying blast wave. For these reasons, the flow, in general, must be solved using computational fluid dynamics (CFD) methods.

However, there exists a special case for which an analytical solution can be obtained. This case corresponds to planar geometry with detonation products expanding in a vacuum with $\gamma = 3$. In this case, the conservation laws are decoupled and can be solved analytically (Stanyukovich [26]). The characteristics are straight lines, which means a solution can be obtained all the way to infinity. Using the method of characteristics for planar homentropic flow, one can show that along a right-running characteristic, the Riemann invariant is:

$$\frac{2}{\gamma - 1}c + u = \text{constant} \tag{6.1}$$

When $\gamma = 3$, $u + c = \text{constant}$. Therefore, the right-running wave has a constant slope:

$$\frac{\mathrm{d}r}{\mathrm{d}t} = u + c = \text{constant} \tag{6.2}$$

The same can be shown for left-running characteristics. This flow is illustrated on an x-t diagram in Fig. 6.2. The flow properties in the different regions are given in Appendix B.

6.1.3 Model of Taylor Wave

The results obtained with the $\gamma = 3$ model described above will demonstrate that the dominant particle heating occurs in the Taylor wave and quiescent flow region following the Taylor wave (see Results in Section 6.2). This result

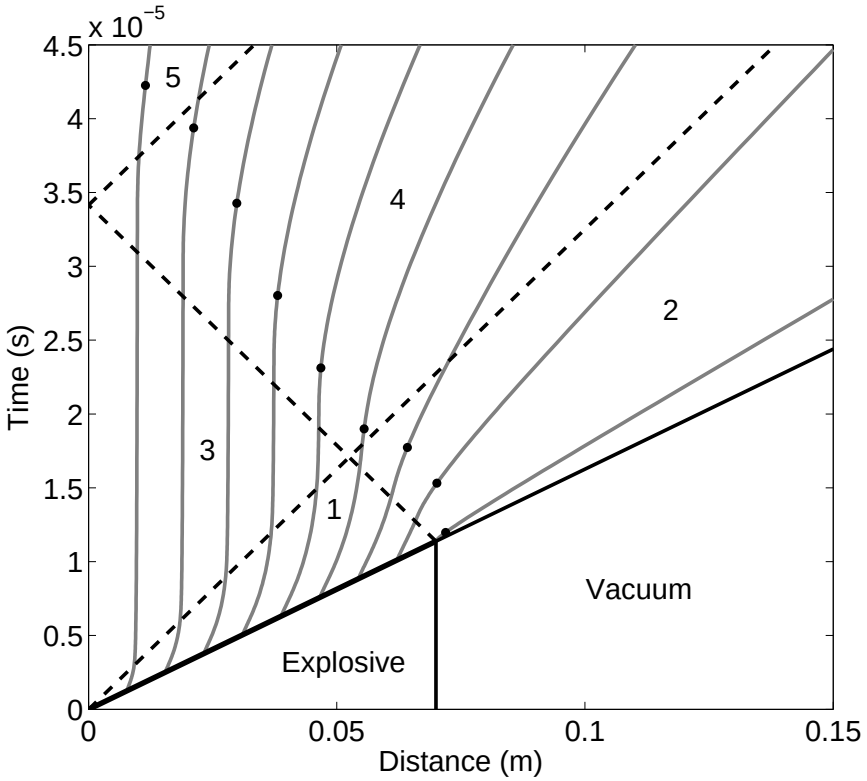

Figure 6.2. x-t diagram of a planar detonation expanding in a vacuum with $\gamma = 3$ - dots indicate time and position of maximum particle temperature along particle trajectory

means that we can limit our attention to just the Taylor wave, which means that more sophisticated analytic solutions are available, since the entire non-simple wave region shown in Fig. 6.2 does not need to be solved. This section discusses solutions of the Taylor wave in non-planar geometries and using more realistic equations of state.

The flow behind a discontinuous detonation wave is self-similar. As a result of this, the conservation laws are reduced to a set of ordinary differential equations, which can easily be solved (Taylor [28]). This can be done for planar,

cylindrical or spherical geometries and for any equation of state. In this study, the Taylor wave will be solved using two different equations of state: 1) perfect gas - constant γ and 2) Jones - Wilkins - Lee (JWL) equation of state [29]. The following ordinary differential equations are the conservation of mass and momentum equations expressed in similarity variables and coordinates:

$$(\phi - \zeta)\frac{\mathrm{d}\psi}{\mathrm{d}\zeta} + \psi\frac{\mathrm{d}\phi}{\mathrm{d}\zeta} + \frac{j\psi\phi}{\zeta} = 0 \tag{6.3}$$

$$(\phi - \zeta)\frac{\mathrm{d}\phi}{\mathrm{d}\zeta} + \frac{1}{\psi}\frac{\mathrm{d}f}{\mathrm{d}\zeta} = 0 \tag{6.4}$$

where

$$\zeta = \frac{r}{R_s} \tag{6.5}$$

$$\psi = \frac{\rho}{\rho_o} \tag{6.6}$$

$$\phi = \frac{u}{\dot{R}_s} \tag{6.7}$$

$$f = \frac{p}{\rho_o \dot{R}_s} \tag{6.8}$$

and $j = 0$, 1 or 2 for planar, cylindrical or spherical geometries. All that is needed to integrate the above conservation laws is an equation of state of the form $f = f(\psi)$ and boundary conditions.

Perfect Gas - Constant γ

As a first approximation, the products will be treated as a perfect gas with constant γ. With this equation of state, the isentrope can be represented by the following equation:

$$\frac{p}{\rho^\gamma} = \text{constant} \tag{6.9}$$

In order to solve the complete flow field analytically, γ must be 3 (see Section 6.1.2). However, if only the Taylor wave is considered, γ can be of any arbitrary value, which means a more realistic value can be used. A value of γ can be obtained from Cheetah 2.0 at the CJ state (see Table 6.1). However, in reality, this value is not constant, but decreases as the products expand. Cheetah also outputs state variables along the CJ isentrope. An even more realistic value of γ can be obtained by fitting to this isentrope in an appropriate pressure range. However, while γ can be chosen to obtain a reasonable fit for any two of the three state variables (pressure, density and temperature), it is difficult (perhaps impossible) to have a good fit for all three.

JWL Equation of State

A common, more realistic equation of state for detonation products is the JWL equation of state [29]. This equation of state is given by the following equation:

$$p = A\exp\left[-\frac{R_1\rho_o}{\rho}\right] + B\exp\left[-\frac{R_2\rho_o}{\rho}\right] + C\left[\frac{\rho}{\rho_o}\right]^{\omega+1} \tag{6.10}$$

This equation of state contains six parameters which can also be obtained from Cheetah: they are tabulated in Table 6.1 for nitromethane detonation products.

Boundary Conditions

It should be noted that integration of the equations is done from the boundary conditions just behind the detonation front - the CJ conditions. However, in the case of cylindrically or spherically propagating detonations, this point is

singular as the gradients are infinite at the front. In special cases (such as for a perfect gas) an approximate solution can be obtained near the front to start the integration (see Taylor [28]). For the JWL equation of state, this approximate solution is too involved and therefore, the integration was started at an arbitrary point where the initial conditions were varied until the result of the integration at the front satisfied the boundary conditions. Figures 6.3 to 6.5 illustrate the flow velocity, density and temperature in the Taylor wave in the various cases investigated. One can see that the quite crude perfect gas - constant γ approximation is very reasonable to describe the flow in the Taylor wave. While the value of 2.7 gives the best results for flow velocity and density, the value of 1.9 is also very close and best captures the flow temperature. $\gamma = 1.9$ is considered to give results closest to the JWL equation of state.

6.1.4 Transport properties

Little is known about the transport properties of condensed phase detonation products. This is no doubt due to the difficulty in achieving the high-pressure and high-temperature of detonation products in the laboratory. Kopyshev *et al.* [66] have developed a model based on a modified van der Waals equation of state that predicts the viscosity of detonation products of PETN, HMX and nitromethane along the CJ isentrope. The model shows that the viscosity is approximately the same for all three explosives at a given pressure. The viscosity decreases significantly with decreasing pressure (as the products expand). Bastea [67] used the Enskog theory and molecular dynamics simulations to predict the viscosity and thermal conductivity of HMX detonation products.

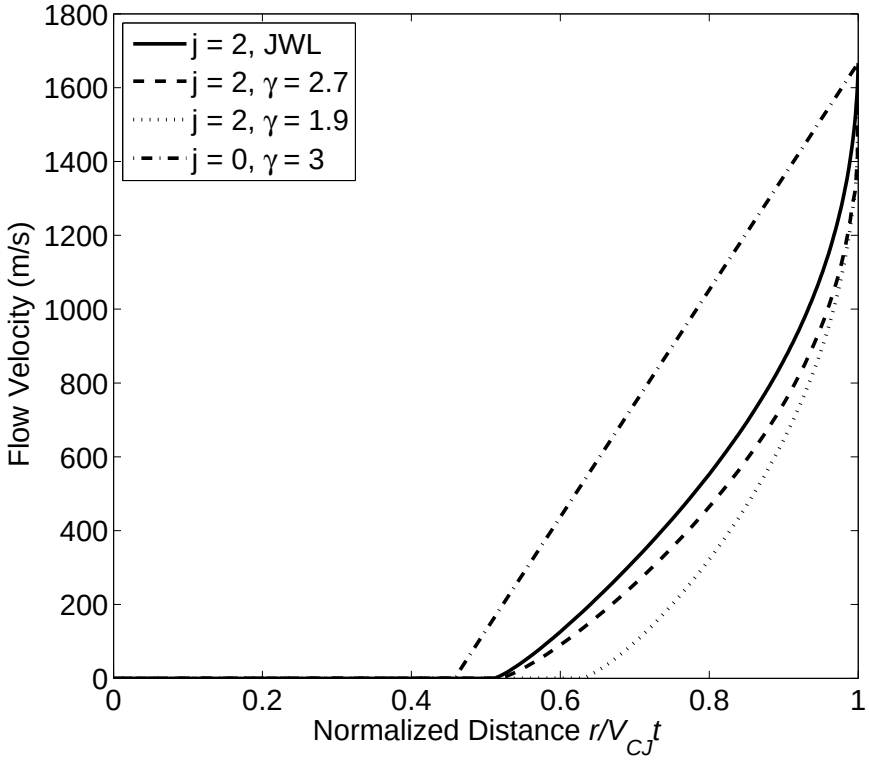

Figure 6.3. Flow velocity distribution in Taylor wave for various cases

A chemical equilibrium code can also predict transport properties (the NASA code CEA [54] for example). However, CEA uses the perfect gas equation of state (which is clearly not applicable in the case of high-explosive detonation products). These different values are listed in Table 6.2 along with transport properties of air at 3500 K [68].

Due to the considerable uncertainty in the transport properties of nitromethane detonation products, it does not seem worthwhile to incorporate a temperature dependent model. Instead, they will be considered to be constant (the values are listed in Table 6.2).

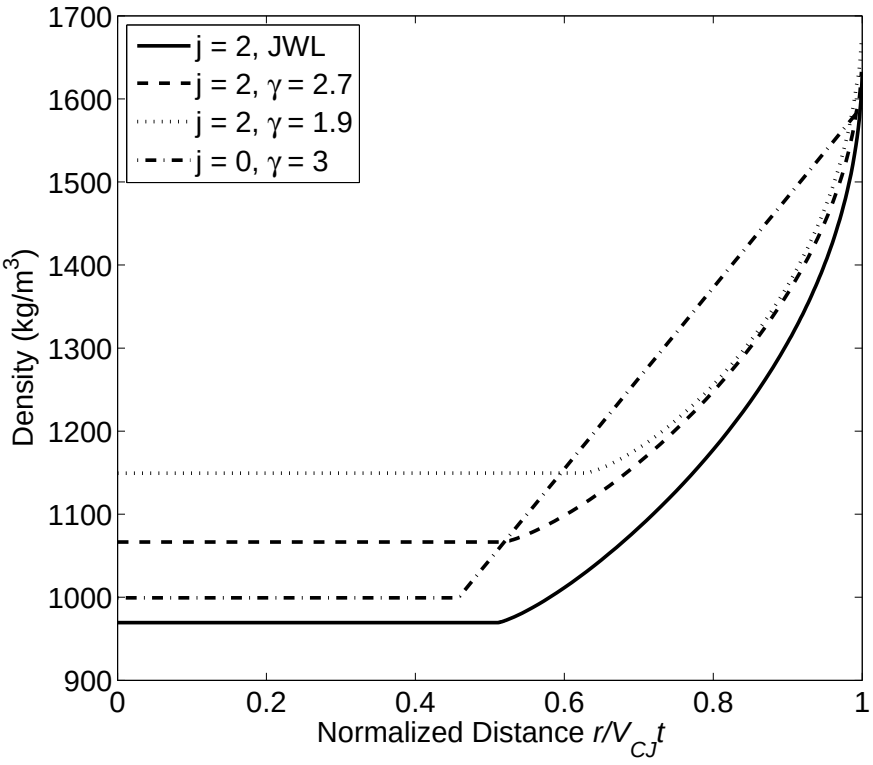

Figure 6.4. Flow density distribution in Taylor wave for various cases

6.1.5 Model of Blast Wave

Since the products were assumed to expand in a vacuum, no blast wave is produced. The front of the detonation products moves at the escape velocity

Source	Viscosity (kg/ms)
Kopyshev et al.	0.001
Bastea	0.0007
CEA	0.00011
Air at 3500 K	0.000086
Present Model	0.00005

Table 6.2. Viscosity of nitromethane detonation products at the CJ state according to various sources

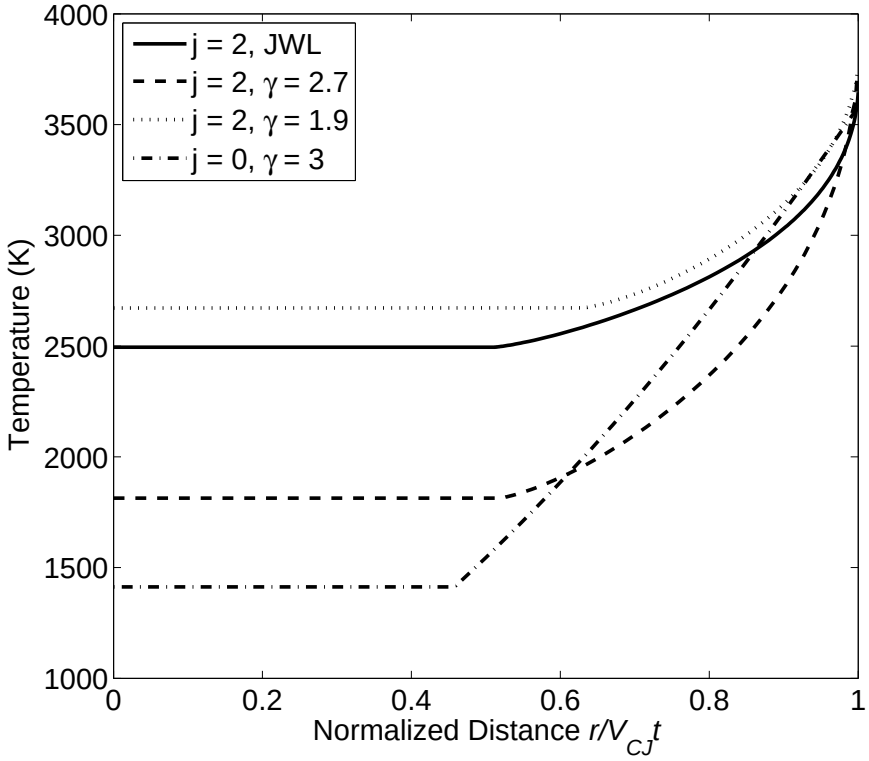

Figure 6.5. Flow temperature distribution in Taylor wave for various cases

and no particle will ever leave the detonation products. The implication is that the model can only be expected to be valid if particle ignition occurs in the detonation products. Note that no restriction is made as to where most of the particle combustion energy is released. As long as particles ignite in the products, they may continue to react after they penetrate the contact surface even if most of the combustion process occurs in shock-heated air. Recall that the aim of the present model is only to predict particle ignition, not its subsequent effect on the blast wave.

6.1.6 Model of Particle Kinematics

The one-dimensional dynamics of the particle are governed by Newton's second law. Neglecting body forces such as gravity, a particle in the detonation products is only subject to a drag force. In general, the drag contains extra terms (carried-mass, pressure gradient and Basset force) that can usually be neglected for small solid particles in gas (see Rudinger [27]). These terms are probably not negligible since the density of the detonation products is comparable to the particle density. Nevertheless, for sake of simplicity, these terms are neglected here. It should be noted however that the uncertainty in viscosity translates to the Reynolds number and thus, to the drag coefficient as well. Therefore, it does not seem worthwhile to include these terms considering the uncertainty in the drag coefficient. Newton's second law then gives:

$$m\frac{\mathrm{d}v_p}{\mathrm{d}t} = \frac{1}{2}C_D A_{CS}\rho_f \left|u_f - v_p\right|\left(u_f - v_p\right) \tag{6.11}$$

Initial conditions must be specified in order to integrate this differential equation. A number of particles are tracked in the flow field. These are distributed evenly in space within the initial explosive. The simulation starts as the detonation reaches the particle. Mathematically, this is expressed as:

$$t_o = \frac{r_o}{V_{CJ}} \tag{6.12}$$

As was mentioned above, the initial velocity will be specified arbitrarily to account for the particle-detonation interaction.

Of course, the fluid density and velocity are obtained from the flow field solution described previously. The drag coefficient is needed in order to integrate the above equation. The drag coefficient is generally a function of Reynolds number. It is straightforward to implement an empirical correlation

to account for this dependence. In this study, the correlation by White [59] will be used:

$$C_D = \frac{24}{\mathrm{Re}} + \frac{6}{1+\sqrt{\mathrm{Re}}} + 0.4 \tag{6.13}$$

It should be noted that the uncertainty in the viscosity affects the drag coefficient via the Reynold's number.

6.1.7 Model of Particle Heating

A particle in the flow of detonation products exchanges heat with its environment via convective and radiative heat transfer. Exothermic chemical reactions at the surface of the particle can also contribute energy to the particle. In general, heat conduction inside the particle must also be considered. However, when the Biot number (ratio of convective heat transfer to the particle to conductive heat transfer within the particle) is small ($\mathrm{Bi} < 0.1$), the temperature distribution inside the particle may be considered to be uniform (see Holman [60], for example). In this case, a lumped capacitance approach can be used and is an important simplification of the problem. The Biot nuber is defined as:

$$\mathrm{Bi} = \frac{hd}{6k_s} \tag{6.14}$$

The worst case scenario (Biot number is maximum) occurs when heat transfer is maximum and the particle is large. Convective heat transfer in the present problem will be maximum just behind the detonation front (temperature and relative flow velocity are maximum at this point). At this point, large particles considered in this study have a Biot number greater than 0.1 (it can be on

the order of 1). This means that temperature gradients in the particle may be small but not negligible. It should be noted that as the particle is accelerated by the flow, and the relative velocity drops, the convective heat transfer drops significantly, thereby reducing the Biot number. For most of the problem, the Biot number is small and therefore, a lumped capacitance approach is used in this model. The resulting energy balance for a particle is given by the following:

$$m\frac{\mathrm{d}E_p}{\mathrm{d}t} = \pi d^2 \left[h(T - T_p) + \epsilon\sigma(T^4 - T_p^4) + kQ\right] \tag{6.15}$$

In the unsteady term, the particle internal energy is used rather than its temperature to account for phase changes. Temperature can then be computed from the internal energy in the following manner:

$$T_p = \frac{E_p}{c_v} \tag{6.16}$$

$$\text{for } E_p < E_{mp} = c_v T_{mp} \tag{6.17}$$

$$T_p = T_{mp} \tag{6.18}$$

$$\text{for } E_{mp} < E_p < E_{mp} + \Delta h_f \tag{6.19}$$

$$T_p = T_{mp} + \frac{E_p - E_{mp}}{c_v} \tag{6.20}$$

$$\text{for } E_{mp} + \Delta h_f < E_p < E_{bp} = E_{mp} + c_v(T_{bp} - T_{mp}) \tag{6.21}$$

Convective Heat Transfer

The convective heat transfer coefficient can be obtained from the definition of the Nusselt number:

$$\mathrm{Nu} = \frac{hd}{k_f} \tag{6.22}$$

The Nusselt number is obtained from empirical heat transfer correlations with Reynolds number, Prandtl number, etc. Whitaker [36] gives the following correlation for spheres:

$$\mathrm{Nu} = 2 + \left[0.4\mathrm{Re}^{\frac{1}{2}} + 0.06\mathrm{Re}^{\frac{2}{3}}\right] \mathrm{Pr}^{0.4} \left[\frac{\mu_\infty}{\mu_w}\right]^{\frac{1}{4}} \tag{6.23}$$

Due to the uncertainty in viscosity, it will be assumed here that the viscosity ratio to the power of $\frac{1}{4}$ is equal to unity. It is not necessary to include high-speed flow effects in the convective heat transfer analysis. The Mach number of the flow relative to the particle is maximum just behind the detonation. Even though the flow of detonation products leaving the detonation is sonic in the detonation reference frame, the particle at rest in the fixed reference frame is exposed to subsonic flow. The flow velocity in the fixed frame is approximately 1670 m/s while the sound speed is approximately 4500 m/s. This results in a Mach number of approximately 0.37, which is sufficiently subsonic and compressibility effects are therefore small.

Radiative Heat Transfer

In general, for low temperatures, radiative heat transfer can be neglected. However, in this case the detonation products start out above 3500 K. Of course, this temperature rapidly drops as the products expand. To assess the importance of radiation, a worst case scenario will be considered. The detonation products and the particle will be considered as black bodies with emissivity/absorptivity equal to 1. These results will be compared to a case where radiation is neglected.

Heterogeneous Surface Reaction

At a finite temperature, a metal particle in an oxidizing environment undergoes chemical reaction at its surface. Of course, the rate of reaction depends on the nature of the oxidizer and its pressure as well as the surface temperature (exponential dependence on temperature). In the problem of interest, the oxidizing environment is complex. It is a mixture of CO_2, CO, H_2O, etc. (see Appendix A for the equilibrium composition given by Cheetah 2.0. Furthermore, the pressure is much higher than what can be achieved in controlled laboratory experiments. For this reason, considerable uncertainty exists in the reaction rate. Nevertheless, an attempt is made here to assess its importance. The rate law is assumed to be Arrhenius in form:

$$k = k_o \exp\left[\frac{-E_a}{RT}\right] \tag{6.24}$$

The values of k_o and E_a vary considerably in the literature [20]. In this study, the values selected for use in the model are taken from Roberts *et al.* [53]. These were fit to reflected shock tube experiments in pure oxygen and are presumably an order of magnitude estimate of heterogeneous surface reactions.

6.1.8 Model of Particle Ignition

In the explosive dispersal of metal particles, the local thermal ignition in the expanding aluminum particle cloud strongly depends on the interplay between the heterogeneous surface reaction and convective heat transfer during the unsteady expansion of detonation products. Behind the detonation front, convective heating increases the particle temperature toward a threshold above which the heterogeneous reaction accelerates significantly to initiate the vapour

phase reaction and combustion propagation in the particle cloud. However, if the products expansion rate is too high such that its temperature becomes less than that of the particles before the threshold is reached, the growth rate of the heterogeneous energy release rate cannot compete with the heat loss rate from the particles to the gas and therefore the ignition of the particle cloud does not occur. Furthermore, even when local ignition occurs, the combustion propagation in the particle cloud can be quenched when the rate of heterogeneous and vapour reaction fails to overcome the rate of convective heat transfer loss due to rapid products expansion. This has been observed in experiments by Frost *et al.* [3] and [4] between the sub-critical and transition particle reaction regimes. Thus, the ignition of the particle cloud occurs when the chemical energy release rates of particles overcome the loss rates and result in rapid temperature increase followed by prompt reaction throughout the cloud. For a single particle in the unsteady expansion of explosive detonation products, the chemical energy release rate of the particle could be too little to compete with the heat transfer rate caused by the rapid expansion of the products. In this case, the ignition of the particle is likely to be dominated by the convective heat transfer from the unsteady expanding products.

As was discussed in Chapter 2, particle combustion occurs in two distinct regimes depending on what limits the reaction rate. In the kinetic regime, the reaction rate is limited by the reaction kinetics which depends on temperature. This means there is sufficient oxidizer for the particle to react but the temperature is relatively low such that the reaction rate is small. In the diffusive regime, the reaction rate is limited by diffusion or transport of oxidizer to the surface of the particle. In this regime, the temperature is high and therefore the kinetics of the reaction is fast. However, since the reaction rate is so fast,

the concentration of oxidizer at the surface of the particle is depleted and the rate at which it diffuses to the surface is what limits the reaction rate. Particle ignition refers to the transition from the kinetic regime to the diffusive regime. In principle, the ignition temperature is not a fundamental property of a fuel because it depends on the particle size and concentration as well as flow boundary conditions. Ignition can occur at different temperatures depending on particle size, flow velocity and so on. In practice, however, physical phenomena such as phase changes may lead to an effective ignition temperature (within a certain range of parameters). For example, it is often considered that the ignition temperatures of aluminum and magnesium are the melting point of the protective oxide layer and the metal boiling point, respectively (see Boiko *et al.* [69] and Roberts *et al.* [53] for example). However, in both cases, there is also evidence that ignition can occur near the metal melting point (see Breiter *et al.* [49] , Fox *et al.* [31], Cassel and Liebman [51], Lokenbakh *et al.* [70], Boiko *et al.* [69] and Rozenband and Vaganova [39]). In the case of aluminum, this is usually attributed to failure of the protective oxide layer (perhaps due to mechanical stresses). This approach (use of critical ignition temperature) is also used in this study for simplicity. If a particle reaches this temperature, it will be considered as being ignited. For both aluminum and magnesium, the metal melting points will be used as critical ignition temperatures. Note that the aluminium melting point is quite low compared to the more "traditional" oxide melting point criterion. However, this choice can be justified by the assumption that the oxide layer is compromised by the detonation wave (see Gilev [46] and Gilev and Anisichkin [47]).

To determine if particle ignition occurs or not, its heating history is computed by integrating Eq. 6.15 subject to the flow field and Eq. 6.11. The

maximum particle temperature is then compared to the ignition temperature. If the maximum particle temperature exceeds the ignition temperature, the particle is considered to have ignited. Of course, particles at different locations, r_o, inside the initial explosive charge experience a different flow field and hence a different heating history. It is possible that in the same configuration, only a fraction of particles ignite. In experiments however, one cannot discern this continuous phenomenon. Therefore, in order to compare with experiments, a number of particles are placed inside the explosive charge at varying locations. Overall, the particles are considered to ignite if a fraction of them larger than some arbitrary threshold ignite. This threshold will be varied to determine the sensitivity of the overall prediction to this parameter. Note that for cylindrical and spherical geometries, the calculation of the fraction of particles that ignite is weighted with r_o and r_o^2, respectively, to account for the fact that there are initially more particles at larger radii.

6.2 Results

The above-described model was first used to compute the flow and magnesium particle heating in a planar nitromethane charge using the perfect gas ($\gamma = 3$) equation of state (particle diameter 100 μm and half-charge length 7 cm). Figure 6.2 is an x-t diagram that shows the 5 different flow field regions and the trajectories of 9 particles equally spaced in the initial explosive charge. The particles are accelerated in the Taylor wave region, then decelerated in the quiescent region behind it and accelerated again by the reflected expansion. On each of these trajectories, a dot indicates the time and place at which the particle temperature reaches a maximum value. Beyond this point, the particle

cools. It is very interesting to note that the particle temperature peaks very shortly upon crossing the leading edge of the reflected expansion. This means that most of the particle heating occurs in the Taylor wave region and in the quiescent region behind it, while the flow is decelerating and the particle velocity exceeds the flow velocity (most of the particle heating occurs during particle deceleration rather than acceleration). This finding suggests that the non-simple wave region can be neglected. This is a very convenient result, since the Taylor wave can be solved analytically for any equation of state and for cylindrical and spherical geometries as well (these are more practical geometries that can be investigated experimentally).

Figure 6.6 shows the Biot number as a function of time for five particles uniformly distributed in the explosive charge. It is generally accepted that the lumped capacitance assumption is valid for Biot numbers less than approximately 0.1. The results show that the Biot number starts out at approximately 1 (well above 0.1) and therefore, at very early times, this approximation is not justified. However, the Biot number very rapidly (in less than 1 μs) decreases as the relative velocity between the flow and the particle decreases. Most of the particle heating occurs while the Biot number is below or near 0.2. This means that the temperature gradients inside the particle are finite but small and neglecting them with a lumped capacitance assumption is reasonable for most of the particle heating process (particularly when considering the uncertainty in the heat transfer coefficient).

Next, the effect of initial velocity is investigated. Upon crossing the detonation, the particle may have momentum imparted to it by the shock front. This effect is modelled here by giving the particle an arbitrary initial velocity. Zhang *et al.* [13] have shown that the particle velocity could reach as much as

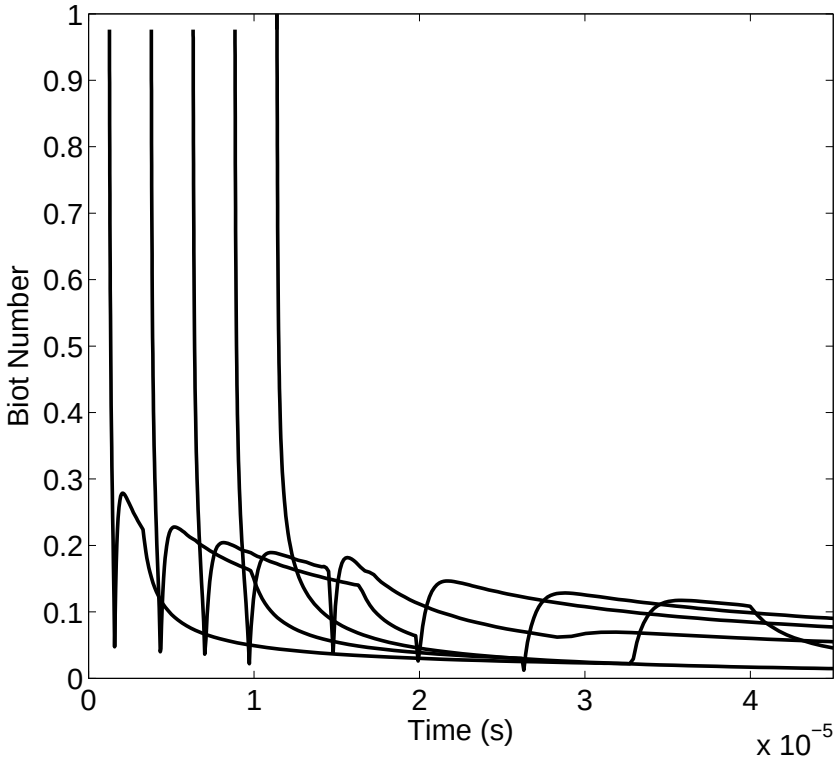

Figure 6.6. Biot number of 100 μm aluminum particles in a 7-cm half-length charge as a function of time

60-100% of the flow velocity simply crossing the shock. Therefore, simulations were done in which the initial particle velocity was varied: 0, 500, 1000 and 1500 m/s. Figure 6.7 shows the velocity of a particle as a function of time for these 4 different cases. Despite the large variation in initial particle velocity, the velocity evolution very quickly converges. In fact, after a very short time, the velocity history curves almost converge to the same answer. The implications of this are that on the timescale of interest, the initial particle velocity does not affect the problem. One can estimate the timescale required for the particle to come into mechanical equilibrium with the flow by considering a

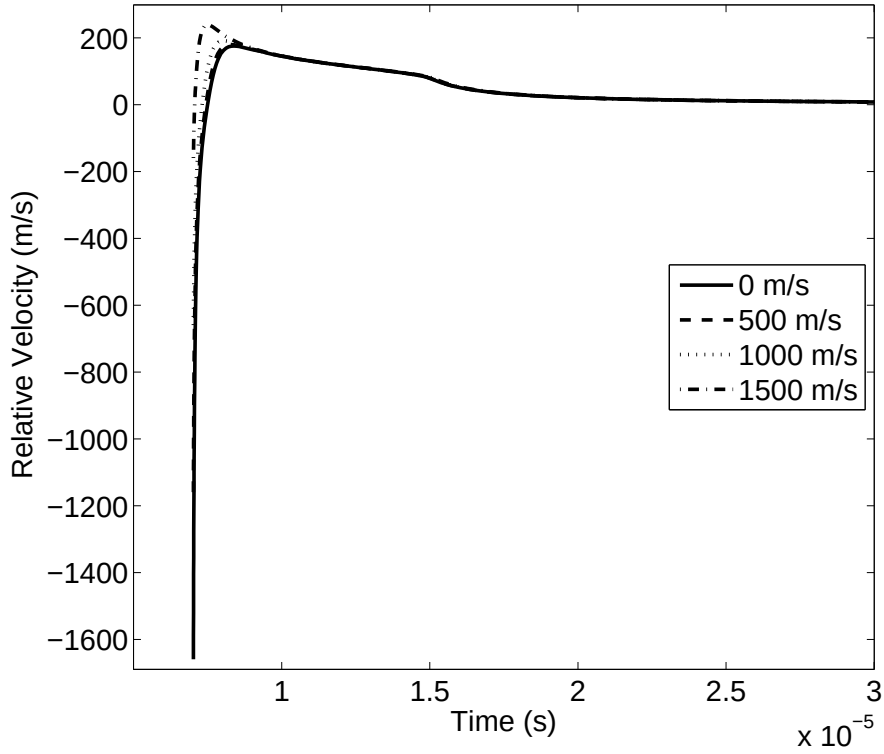

Figure 6.7. Relative flow velocity as a function of time for various initial velocities

particle initially at rest in a uniform flow with velocity v_o. The time for the particle to reach

$$\left[1 - \frac{1}{\mathrm{e}}\right] v_o \tag{6.25}$$

(approximately 63% of vo) is given by:

$$\tau_{eq} = \frac{4\rho_p(\mathrm{e}-1)d}{3\rho_f C_D v_o} \tag{6.26}$$

The mechanical equilibration time scale is approximately 0.17 μs for a 100 μm particle in a flow of detonation products at 1500 m/s. While this

timescale is approximately tenfold the timescale for the detonation to cross the particle, it is approximately 300 times less than the timescale of particle heating in expanding detonation products (for a charge radius of 10 cm). Therefore, on the timescale of interest (expanding detonation products), it is unnecessary to consider momentum transfer to the particle by the detonation wave as the mechanical equilibration time is negligibly small (drag is sufficiently large that the particle rapidly comes into mechanical equilibrium with the flow). Of course, the particle never comes in complete mechanical equilibrium with the flow since it is unsteady. Therefore, convection continues to be important but far less than it is near the CJ point. For sake of simplicity, then, the particle will be considered to be at rest upon the passage of the detonation, rather than include an initial momentum transfer that may actually occur. It is found that changing the initial velocity from 0 to 1500 m/s changes the total amount of energy transferred to the particle (from the time of detonation arrival to the reflected expansion) by less than 4%. Therefore, it can clearly be concluded that initial momentum transfer during the detonation - particle interaction has a negligible effect on the overall phenomenon.

The contribution of radiation on overall particle heating can also be investigated. By setting the absorptivity of the particle to 1, an upper bound for the relative contribution of radiation is obtained. On the contrary, setting the absorptivity of the particle to 0, radiation is neglected. Comparing these two results allows one to assess the importance of radiation with respect to particle heating. It is found that radiation contributes approximately 0.2% of the total energy transferred to the particle and can therefore be neglected.

Furthermore, the effect of heterogeneous surface reaction can be investigated by switching on and off the reaction rate law. In this case as well,

surface reactions can be neglected. It is found that even using a kinetic rate ten times greater than that used by Roberts *et al.* [53], the contribution of chemical reaction is less than 0.01% of the energy transferred to the particle. This is also convenient as it allows the problem to be simplified further with negligible loss of accuracy.

6.2.1 Concept of CDPI

Figure 6.8 shows time histories of a 100 μm magnesium particle in the expanding detonation products for three different diameter spherical charges (D_1 = 20, D_2 = 15 and D_3 = 8 cm. For all the charge diameters, the expanding detonation products first heat up the particle to a peak temperature and then cool the particle as the products further expand. An increase in the charge diameter results in an increase in particle peak temperature. Particle ignition is assumed to occur when the peak temperature exceeds the ignition temperature. Hence, for a given particle size, there is a minimum charge diameter (termed critical diameter for particle ignition (CDPI) by Frost *et al.* [2] for which the peak temperature of a sufficient fraction of particles equals or exceeds the ignition temperature.

6.2.2 Comparison with Experiments

Magnesium

As was mentioned above, the model results can be compared to experimental results. For a given charge and particle size, the model can be integrated and

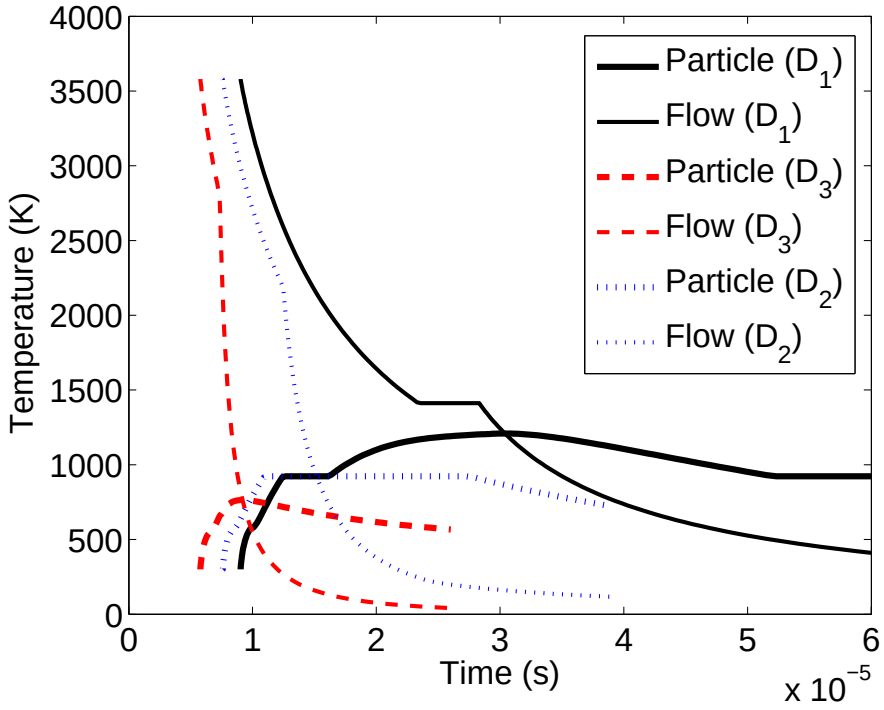

Figure 6.8. Particle (100 μm) and flow temperatures for three different charge sizes

the peak particle temperatures can be obtained and compared to the ignition temperature. If a sufficient fraction of the particles exceeds the ignition temperature, the particles are considered to be ignited. For a given particle size, an iterative procedure was used to determine CDPI. Figure 6.9 shows how the CDPI varies with particle size. As is the case in experiments by Frost *et al.* [2], [3] with magnesium particles, the CDPI is found to increase with particle size. The reason for this is relatively simple: larger particles need to be heated for a longer time to reach the ignition temperature. Larger charges provide this longer residence time for particles within the detonation products. Different cases are illustrated on this figure. The first case is the

planar geometry with $\gamma = 3$. Considering only the Taylor wave and the quiescent region behind it, the model can be integrated in a spherical geometry. This is also represented on the figure for various equations of state, along with experimental data from [2] and [3] for nitromethane spheres saturated with magnesium particles. Solid symbols represent prompt particle ignition (blast is reinforced by particle combustion energy release) whereas open symbols and X's represent delayed ignition and no ignition, respectively (blast is not reinforced in these cases). Note that the prediction is higher than the experimental results, presumably in part due to the assumption of very small particle loading (while the experiments were conducted under a packed bed of granular material condition). Furthermore, the particle temperature increase during the shock and detonation interaction is not considered in the current model. Also, particles may leave the detonation products and interact with shock heated air, which is not considered in the present model. These factors all tend to over-predict experimental results. However, the model does capture the basic physical trend of the CDPI phenomenon, thus indicating the fundamental role of the unsteady expansion of the detonation products in determining the particle ignition during the explosive dispersal process.

It should be noted that the critical fraction of particles that must reach the ignition temperature to be considered successful initiation has a very small effect on the overall result. Changing this critical fraction from 25 to 75% changes the coefficient and exponent of a power law fit to the results by less than 2%. The effect is so small because the peak temperature is a weak function of particle initial position, i.e., all particles reach approximately the same peak temperature. This is certainly true near critical conditions, presumably in part because the ignition temperature corresponds to the metal melting

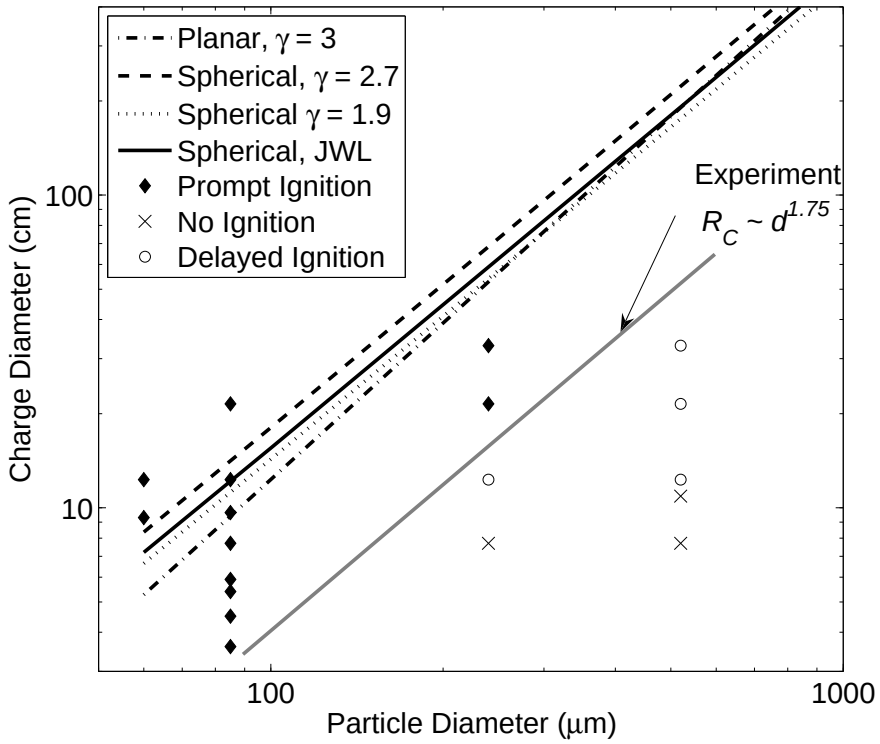

Figure 6.9. Critical charge diameter for particle ignition (CDPI) as a function of particle diameter for magnesium

point. The particle temperature remains constant during phase change. Figure 6.10 shows the peak internal energy as a function of initial position of the particle inside the explosive charge. The peak particle internal energy is maximum at an intermediate radius and decreases both toward the charge centre and edge. At the very edge, the peak temperature goes to zero because the time for particle heating is zero. Except for particles near the edge of the charge, the particle heating is rather uniform for most particles. This has interesting implications in terms of modelling. One can consider a single particle to be representative of most particles (see Chapter 7). Note that all results

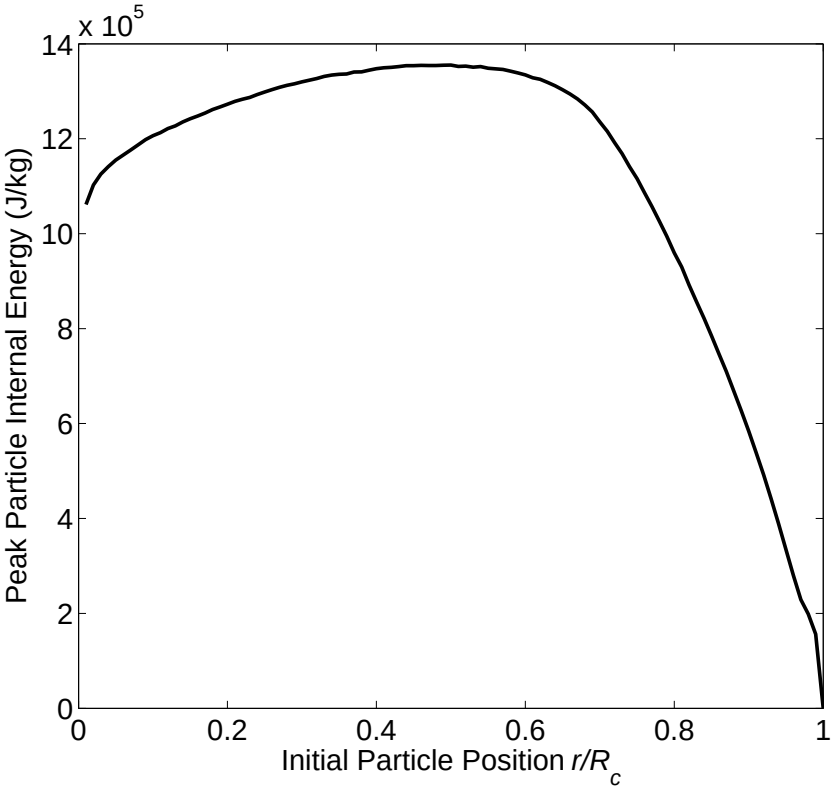

Figure 6.10. Peak particle temperature as a function of initial particle location (r_o) inside inside the charge

shown in this chapter have been obtained with a critical fraction of 50%.

As expected, with a similar equation of state ($\gamma = 2.7$ instead of 3), the CDPI is higher for the spherical case than for the planar case. This is due to the more severe expansion of the products in the spherical geometry. Decreasing γ, however, increases the flow temperature, which results in a decrease in CDPI. Comparison with the state along the CJ isentrope given by Cheetah, it is found that values of γ of 2.7 (Cheetah fit at the CJ point) or 3 considerably under predict the temperature of the detonation products. While a value of

1.9 gives a much more accurate temperature, they over predict the density and flow velocity. For this reason, the Taylor wave was also solved with the JWL equation of state. This equation of state is considered to be quite accurate for detonation products [29]. The result obtained with the JWL equation of state is also plotted on Fig. 6.9. It is found to be in quite good agreement with the $\gamma = 1.9$ solution. It is reasonable to think that this is the case because this value of γ is the one that best reproduces flow temperature and that temperature plays the dominant role in the particle heating problem.

Aluminum

The same model can be used to predict the CDPI for aluminum particles. The results are found to be very similar to the case of magnesium particles. The CDPI increases with the particle size as d^n with n approximately equal to 1.75. Experimental results by Frost *et al.* [3] and [4] with aluminum particles, however, are much more complicated than those obtained with magnesium. The behaviour is found to be very different in cylindrical and spherical geometries. In cylindrical charges, the CDPI appears to be minimum between 30 and 50 μm. Spherical charges are even more complex and show a much more gradual behaviour. While it is difficult to identify a CDPI in this case, large particles/large charges and small particles/small charges appear to ignite more readily. All these complex phenomena are not captured by the present model. This suggests that the ignition criterion that was chosen is not suitable for aluminum particles. In fact, the experimental results suggest that there is no ignition temperature for aluminum in high-explosive detonation products and that another mechanism is at play (possibly several mechanisms). Thus, the experimental results of Frost *et al.* [3] are not included in the present study.

6.3 Discussion

The problem of particle heating in expanding detonation products reduces to the solution of a set of ordinary differential equations if the products are assumed to be perfect gases with $\gamma = 3$ expanding to vacuum in a planar geometry. It is found that most of the particle heating occurs in the Taylor wave and in the quiescent flow region behind it. It is interesting that the flow field in those two regions is the same whether the products expand in a vacuum or in ambient air (with a blast wave). Furthermore, the flow in these regions can be solved in other geometries (cylindrical or spherical) and with more realistic equations of state (γ different from 3 or JWL).

The model predictions of critical charge diameter for particle ignition agree quite well with experimental results for magnesium particles. This suggests that the model captures the appropriate governing mechanisms for particle ignition, i.e., convective heating of the magnesium particles in the Taylor wave and in the quiescent region. The model also suggests that in the case of magnesium particles, an ignition temperature can be defined. It appears that the melting point is an appropriate ignition temperature.

In the case of aluminum particles, the model predicts a trend similar to that of magnesium: the CDPI should increase monotonically with the particle diameter. However, experimental results are much more complex and ambiguous, suggesting that in the case of aluminum, other phenomena should be considered. For example, aluminum particles typically have a protective oxide shell which may affect the results. Mechanically compromising this oxide layer may be a better criterion for particle ignition than an ignition temperature. Furthermore, it is possible that in experiments, aluminum particles ignite (at

least in some cases) in shock-heated air rather than in the detonation products.

The model shows that velocity imparted to the particle by the detonation itself is not important to the overall phenomenon within the assumptions made. The timescale for mechanical equilibration with the flow, while much longer than the timescale of the particle-detonation interaction, is more than two orders of magnitude less than the particle heating timescale. Therefore, regardless of the velocity imparted to the particle during the detonation passage, the particle's velocity quickly approaches the flow velocity.

It is found that radiative heat transfer is negligible compared to convective heat transfer. This is also the case for heterogeneous surface reaction, although in this case, considerable uncertainty exists in the chemical kinetic rate of the reaction.

It was also found that particles located near mid-radius reached a higher peak temperature than particles near the centre or the edge of the charge. Nevertheless, near critical conditions, the peak temperature variation with initial position was relatively small (presumably, the fact that the ignition temperature is the melting point contributes to this: the particle temperature remains constant during melting). This finding leads to an even more simplified approach (see Chapter 7) where a single particle near the centre of the charge is considered to be representative of all particles. This particle is accelerated by the Taylor wave (where negligible heating occurs) and is then decelerated and heated in the quiescent flow region. This problem is solved analytically and results in a scaling law for charge diameter and particle diameter:

$$R_c \sim d_p^n \tag{6.27}$$

where n is bound by 1.5 for small particles and 2 for large particles (see Chap-

ter 7). This is in excellent agreement with experimental results (neither small nor large particles) where n is found to be approximately 1.75.

Chapter 7

Analytical Scaling Law

In light of the results of Chapter 6, an even more simplified approach can be used to determine analytically the scaling law, or the functional dependence of the CDPI to the particle diameter. It was found that the peak particle temperature occurs shortly after the passage of the leading edge of the reflected expansion. In other words, only the Taylor wave and the quiescent flow regions need be considered. It was also found that the peak particle temperature varied only slightly with initial position of the particle: all particles reach approximately the same peak temperature (within 100 K). Therefore, any initial position may be considered to be representative of all particles. This fact allows the model to be simplified by analyzing a particle near the centre of the charge. For such a particle, the Taylor wave is of very short duration. During this time, negligible particle heating occurs. However, the Taylor wave may accelerate the particle such that it enters the quiescent flow region with some finite velocity. Suppose this velocity is known. Then, it is straightforward to solve the particle dynamics and heating in quiescent gas at

a known temperature. Solving Newton's second law with initial conditions: $v = v_o$, @$t = 0$, gives the following expression for particle velocity:

$$v = \frac{v_o}{1 + \frac{\omega t}{d}} \tag{7.1}$$

where

$$\omega = \frac{3}{4}\frac{\rho_f}{\rho_p}C_D \tag{7.2}$$

The particle energy balance considering only convective heat transfer is given by:

$$mc_v\frac{\mathrm{d}T}{\mathrm{d}t} = \pi d^2 h(T_\infty - T) \tag{7.3}$$

The heat transfer coefficient h is obtained from the definition of the Nusselt number:

$$h = \frac{\mathrm{Nu}k_f}{d} \tag{7.4}$$

The Nusselt number is correlated to the Reynolds number. For sufficiently large Reynolds number, a simplified correlation can be used:

$$\mathrm{Nu} = C\mathrm{Re}^n \tag{7.5}$$

Combining Eqs. 7.1, 7.3 and 7.4 for the particle velocity gives:

$$\frac{\mathrm{d}T}{\mathrm{d}t} = \frac{\omega v_o}{d^{2-n}}\sigma(1-n)\left[1 + \frac{\omega v_o t}{d}\right]^{-n}(T_\infty - T) \tag{7.6}$$

where

$$\sigma = \frac{6k_f C}{(1-n)\omega v_o \rho_p c_v}\left[\frac{\rho_f v_o}{\mu}\right]^n \tag{7.7}$$

Integrating and solving for time required to reach the ignition temperature:

$$t = \frac{d}{\omega v_o}\left\{\left[1 + \frac{d^{1-n}}{\sigma}\ln\left(\frac{T_\infty - T_o}{T_\infty - T_{ign}}\right)\right]^{\frac{1}{1-n}} - 1\right\} \tag{7.8}$$

At critical conditions, the time it takes for the particle to heat up is related to the charge size:

$$t \sim \frac{R_c}{V_{CJ}} \tag{7.9}$$

Therefore, a relationship between charge size and particle size is obtained:

$$R_c \sim \frac{dV_{CJ}}{\omega v_o}\left\{\left[1 + \frac{d^{1-n}}{\sigma}\ln\left(\frac{T_\infty - T_o}{T_\infty - T_{ign}}\right)\right]^{\frac{1}{1-n}} - 1\right\} \tag{7.10}$$

There are two limiting cases for this expression: 1) very small particles and 2) very large particles.

7.1 Small Particles

When the particle size is small enough such that

$$1 >> \frac{d^{1-n}}{\sigma}\ln\left[\frac{T_\infty - T_o}{T_\infty - T_{ign}}\right] \tag{7.11}$$

the charge size can be approximated as:

$$R_c \sim \frac{V_{CJ}}{\sigma\omega v_o}\left[\frac{1}{1-n}\right]\ln\left[\frac{T_\infty - T_o}{T_\infty - T_{ign}}\right] d^{2-n} \tag{7.12}$$

or

$$R_c \sim d^{2-n} \tag{7.13}$$

For $n = 0.5$, $R_c \sim d^{1.5}$.

7.2 Large Particles

When the particle size is large enough such that

$$1 << \frac{d^{1-n}}{\sigma} \ln \left[\frac{T_\infty - T_o}{T_\infty - T_{ign}} \right] \tag{7.14}$$

then,

$$R_c \sim \frac{V_{CJ} d^2}{\omega v_o} \left[\frac{1}{\sigma} \ln \left(\frac{T_\infty - T_o}{T_\infty - T_{ign}} \right) \right]^{\frac{1}{1-n}} \tag{7.15}$$

or,

$$R_c \sim d^2 \tag{7.16}$$

Therefore, the dependence of the critical charge size for particle ignition on particle diameter can be approximated as a power law. With $n = 0.5$, the exponent is bound between 1.5 and 2 for small and large particles, respectively. Experiments conducted by Frost *et al.* [2] and [3] also show a power law dependence with exponent approximately equal to 1.75. It is interesting to note that in these experiments, the particles are neither small nor large (with respect to Eqs. 7.11 and 7.14). Therefore, one would expect the exponent to be between 1.5 and 2, which it is at 1.75. This agreement suggests validity of the model.

Chapter 8

Conclusions

The various models for metal particle evaporation, combustion and breakup reviewed in Chapter 2 are all consistent with the d^2 law. Most of these models, while developed for a quiescent atmosphere can be extended to a convective environment. In this case, the models suggest a reaction time proportional to approximately $d^{1.5}$. The only exception to this is for particle combustion in a kinetic-limited regime, as opposed to the "traditional" diffusion-limited regime. In the kinetic regime, the reaction duration is expected to be linear with the initial particle size. It was also shown that small particle sizes and high-speed flow promote the kinetic regime by increasing the diffusion of heat and oxidizer to the particle to a point where the chemical kinetic rates become the limiting process.

Experiments were conducted in the present study in which particles were placed in the detonation products of a hydrogen - oxygen mixture. Time-resolved particle reaction was monitored with the use of a photodiode. The signals obtained were very different from those that are observed in typical

metal particle combustion experiments in quiescent or low-speed flow. Luminosity was observed almost instantaneously. There were no clear ignition or extinction events that could be observed from these traces. While chemical reaction was no doubt taking place, the particles did not appear to ignite. Nevertheless, an attempt was made to estimate a reaction delay and duration from the signals. In the case of aluminum particles, the reaction duration appeared to scale approximately with $d^{0.5}$. While this is inconsistent with diffusion-limited reaction, it may indicate that the particles react in the kinetic regime. Even though the measured dependence was not linear, the agreement is reasonable, considering the difficulty in defining the reaction duration. In the case of magnesium particles, the reaction duration was found to be closer to a linear dependence with the particle size. Only the largest magnesium particles (GRAN 17, 240 μm) was there an indication that the particles may have ignited.

In order to confirm the combustion regime of the particles, the combustion temperature of the particles was measured using emission spectroscopy. Recall that the kinetic - diffusive model of Section 2.4 showed that in the diffusive regime, the particle temperature is significantly higher than the flow temperature because there must be large gradients in the oxidizer concentration and temperature around the particle for diffusion to be the limiting rate. In contrast, in the kinetic regime, the particle temperature approaches the flow temperature. The temperature measurements obtained from spectroscopy were lower than the flow temperature by approximately 400-500 K (note that the flow temperature that was calculated using CFD is probably an over-estimate of the actual temperature). The measured temperature, 2400-2700 K is just below the boiling point of aluminum. The results also suggest reaction in the

kinetic regime.

An attempt was made to model the experimental results. The flow field was modelled using an Euler CFD code. A single particle's trajectory and heating history was then integrated. The modelling had limited success in predicting the reaction delay. While the results were in the right order of magnitude, the model predicts that the reaction delay should scale with the square of diameter. Instead, the experimental reaction delay appeared to be linear with the particle diameter. It is concluded that the definition that was used for the reaction delay (in experiments) may be unappropriate given that the particles probably react in the kinetic regime.

The second part of this study consisted of developing a simple analytical model for metal particle ignition in the detonation products of high-explosives. Even though this model is highly idealized and contains many approximations, it does fulfill its goal of providing insight into the governing mechanisms and identifying a scaling law for particle ignition. By making important assumptions (treating the products as a perfect gas with $\gamma = 3$, expansion into a vacuum and a planar geometry), the entire flow field was solved analytically. Particle trajectories and heating histories could then be calculated by integrating simple ODE's.

It was found that most of the particle heating occurs in the Taylor wave and in the quiescent region behind it. Indeed most particles would see their temperatures peak just after the passage of the reflected expansion. This expansion cools the products so rapidly that the products quickly become cooler than the particles. This result is very convenient as it allows one to simplify the problem and only consider the Taylor wave and the quiescent region. Since

the Taylor wave is self-similar, it can be solved analytically for more sophisticated equations of state and more practical geometries. Therefore, the model was used with a JWL equation of state in a spherical geometry, which allows comparison with experiments by Frost *et al.* [2], [3], [4].

These experiments with packed beds of particles saturated with nitromethane showed a critical charge diameter for particle ignition (CDPI). The metal particles only ignite if the charge is made larger than the CDPI. With magnesium particles, the CDPI was found to increase with particle size according to $d^{1.75}$. The model results were in excellent agreement with this scaling law although the CDPI was found to be significantly higher than in experiments (particles appear to ignite more readily in experiments than predicted by the model).

A further simplification of the model led to the derivation of an analytical scaling law (in the original model, ODE's need to be solved for every charge diameter - particle diameter combination). By only considering a particle near the centre of the charge and the quiescent region behind the Taylor wave, an algebraic expression was obtained for the critical charge diameter as a function of particle diameter. In the limit of small particles the CDPI increases as $d^{1.5}$, while in the limit of large particles, the CDPI increases with d^2. Experimental results with particles neither small nor large showed a CDPI proportional to $d^{1.75}$, which is excellent agreement with the model.

8.1 Original Contributions to Knowledge

The objective of the present study was to investigate the combustion of metal particles in the flow of detonation products of gaseous and high-explosives. While the combustion of metal particles has been studied in a number of experimental conditions (gas burners, shock tubes, constant volume explosion vessels, etc.) it had never been systematically studied in the flow of a gaseous detonation. The study has shown that the reaction delay and duration of aluminum and magnesium particles increase approximately linearly with particle diameter. This is in contrast to more typical experimental conditions with little or no relative flow velocity where the combustion time follows the classical d^2 law. Temperature measurements made have shown a combustion temperature below the flow temperature (near the boiling point of aluminum). This is also different from typical results where combustion in the thin diffusion flame surrounding the particle occurs well above the flow temperature. These findings are all consistent with a combustion regime limited by chemical kinetic rates rather than diffusion of oxidizer.

Furthermore, a simple analytical model was developed to study the ignition of metal particles in high-explosive detonation products. While many multiphase CFD codes have been developed to study this phenomenon, this model proves to be quite insightful due to its analytical nature and simplicity. The model has shown that most of the particle heating leading to ignition occurs in the Taylor wave and in the quiescent flow region behind it while the flow decelerates and the particle velocity exceeds the flow velocity. Most of the energy acquired by the particle is due to convective heat transfer. Radiation and heterogeneous surface reactions appear to be negligible. It is also found that

the momentum imparted to the particle by the passage of the detonation front is irrelevant to the phenomenon because the timescale for mechanical equilibration between the flow and the particle is much smaller than the timescale of particle heating to ignition. Finally, the model suggests an analytical scaling law for the critical charge diameter for particle ignition (CDPI) which is in good agreement with previous experimental results with magnesium particles. This suggests validity of the model and that the phenomenon of CDPI is simply a competition between particle heating and detonation products cooling via adiabatic expansion.

It should be noted that the model for particles in detonation products of high-explosives assumes an ignition temperature.

References

[1] P. J. Haskins, M. D. Cook, and R. I. Briggs. The effect of additives on the detonation characteristics of a liquid explosive. In *Proceedings 12th APS Topical Group Meeting on Shock Compression of Condensed Matter*, Atlanta, 24-29 June 2001.

[2] D. L. Frost, F. Zhang, S. B. Murray, and S. McCahan. Critical conditions for ignition of metal particles in a condensed explosive. In *12th International Detonation Symposium*, San Diego, 11-16 August 2002.

[3] D. L. Frost, S. Goroshin, R. Ripley, and F. Zhang. Effect of scale on the blast wave from a metalized explosive. In *13th International Detonation Symposium*, Norfolk, VA, 23-28 July 2006.

[4] D. L. Frost, S. Goroshin, J. Levine, R. Ripley, and F. Zhang. Critical conditions for ignition of aluminum particles in cylindrical explosive charges. In *AIP Conference Proceedings - Shock Compression of Condensed Matter*, pages 972–975, 2005.

[5] F. Zhang, A. Yoshinaka, D. Frost, R. Ripley, K. Kim, and W. Wilson. Casing influence on ignition and reaction of aluminum particles in an explosive. In *13th International Detonation Symposium*, Norfolk, VA, 23-28 July 2006.

[6] R. C. Ripley, L. Donahue, T. E. Dunbar, and F. Zhang. Explosion performance of aluminized TNT in a chamber. In *19th International Symposium on Military Aspects of Blast and Shock*, Calgary, AB, October 1-6 2006.

[7] A. M. Milne, S. Cargill, K. Bennett, and A. W. Longbottom. Modelling of enhanced blast and heterogeneous explosives. In *19th International*

Symposium on Military Aspects of Blast and Shock, Calgary, AB, October 1-6 2006.

[8] M. A. Cooper, M. R. Baer, R. G. Schmitt, M. J. Kaneshige, R. J. Pahl, and P. E. DesJardin. Understanding enhanced blast explosives: A multi-scale challenge. In *19th International Symposium on Military Aspects of Blast and Shock*, Calgary, AB, October 1-6 2006.

[9] J. Massoni, R. Saurel, A. Lefrancois, and G. Baudin. Modeling spherical explosions with luminized eneretic materials. *Shock Waves*, 16(1):75–92, 2006.

[10] K. Kim, W. Wilson, S. Peiris, C. Needham, C. Watry, D. J. Ortley, and F. Zhang. Effects of particle damage during detonation of thermobarics on subsequent reactions. In *21st International Colloquium on the Dynamics of Explosions and Reactive Systems*, Poitiers, France, July 23-27 2007.

[11] D. L. Frost, T. Aslam, and L. G. Hill. Application of detonation shock dynamics to the propagation of a detonation in nitromethane in a packed inert particle bed. In *AIP Conference Proceedings - Shock Compression of Condensed Matter*, pages 821–824, 2000.

[12] R. C. Ripley, F. Zhang, and F.-S. Lien. Detonation interaction with metal particles in explosives. In *13th Symposium (International) on Detonation*, pages 214–223, Norfolk, VA, July 23-28 2006.

[13] F. Zhang, P. Thibault, and R. Link. Shock interaction with solid particles in condensed matter and related momentum transfer. *Proceedings Royal Society, London A*, 459(2031):705–726, 2003.

[14] M.W. Beckstead. Correlating aluminum burning times. *Combustion, Explosion, and Shock Waves*, 41(5):533–546, 2005.

[15] S. Goroshin, J. Mamen, A. J. Higgins, T. Bazyn, N. Glumac, and H. Krier. Emission spectroscopy of flame fronts in aluminum suspensions. *Proceedings of the Combustion Institute*, 31(2):2011–2019, 2007.

[16] S. R. Turns. *An Introduction to Combustion.* McGraw Hill, Boston, 2000.

[17] I. Glassman. *Combustion.* Academic Press Inc., Orlando, 1987.

[18] T. Bazyn, H. Krier, and N. Glumac. Evidence for the transition from the diffusion-limit in aluminum particle combustion. *Proceedings of the Combustion Institute*, 31(2):2021–2028, 2007.

[19] L. A. Vulis. *Thermal Regimes of Combustion*. McGraw Hill Book Company, New York, 1961.

[20] M. A. Trunov, M. Schoenitz, and E. L. Dreizin. Ignition of aluminum under different experimental conditions. *Propellants, Explosives and Pyrotechnics*, 30(1):36–43, 2005.

[21] V. Tanguay, A. J. Higgins, and F. Zhang. A simple analytical model for reactive particle ignition in explosives. *Propellants, Explosives and Pyrotechnics*, 32(5):371–384, 2007.

[22] K. Ramadan and P. B. Butler. Analysis of particle dynamics and heat transfer in detonation spraying systems. *Journal of Thermal Spray Technology*, 13(2):248–264, 2004.

[23] P. Fauchais, A. Vardelle, and B. Dussoubs. Quo vadis thermal sparaying. *Journal of Thermal Spray Technology*, 10(1):44–66, 2001.

[24] M. K. Alkam and P. B. Butler. Analysis of a pulsed detonation thermal spray applicator. *Combustion Science and Technology*, 159:17–37, 2000.

[25] K. Ramadan and P. B. Butler. A two-dimensional axisymmetric flow model for the analysis of pulsed detonation thermal spraying. *Combustion Science and Technology*, 175:1649–1677, 2003.

[26] K. P. Stanyukovich. *Unsteady Motion of Continuous Media*. Pergamon Press, London, 1960.

[27] G. Rudinger. *Fundamentals of gas-particle flow*. Elsevier, Amsterdam, 1980.

[28] G. Taylor. The dynamics of the combustion products behind plane and spherical detonation fronts in explosives. *Proc. R.. Soc. Lond. A*, 200(1061):235–247, 1950.

[29] W. Fickett and W. C. Davis. *Detonation Theory and Experiment*. Dover Publications, Inc., Mineola, New York, 1979.

[30] L. W. Connell. Aerothermoballistics of pyrophoric metal shrapnel in high speed, high Weber number flows. In *AIAA 22nd Aerospace Sciences Meeting*, number AIAA-84-0209, Reno, NV, January 9-12 1984.

[31] T. W. Fox, J. A. TeVelde, and J. A. Nicholls. Shock wave ignition of metal powders. In *Proceeedings of the 1976 Heat Transfer and Fluid Mechanics Institute*, pages 241–256, Stanford, 1976. Stanford University Press.

[32] T. W. Fox, C. W. Rackett, and J. A. Nicholls. Shock wave ignition of magnesium powders. In *Proceedings of the Eleventh International Symposium*, Seattle, WA, July 11-14.

[33] M. Pilch and C. A. Erdman. Use of breakup time data and velocity history data to predict the maximum size of stable fragments for accelerated-induced breakup of a liquid drop. *Journal of Multiphase Flow*, 13(6):741–757, 1987.

[34] A. A. Ranger and J. A. Nicholls. Aerodynamic shattering of liquid drops. *AIAA Journal*, 7(2):285–290, 1969.

[35] L. Lees. Similarity parameters for surface melting of a blunt nosed body in a high velocity gas stream. *ARS Journal*, 29:345–354, 1959.

[36] S. Whitaker. Forced convection heat transfer correlations for flow in pipes, past flat plates, single cylinders, single spheres, and for flow in packed beds and tube bundles. *AIChE Journal*, 18(2):361–371, 1972.

[37] D. A. Frank-Kamenetskii. *Diffusion and Heat Transfer in Chemical Kinetics*. Princeton University Press, Princeton, 1955.

[38] B. M. Henry, F. Dinelli, K.-Y. Zhao, C. R. M. Grovernor, O. V. Kolosov, G. A. D. Briggs, A. P. Roberts, R. S. Kumar, and R. P. Howson. Microstructural study of transparent metal oxide gas barrier films. *Thin Solid Films*, 355:500–505, 1999.

[39] V. I. Rozenband and N. I. Vaganova. A strength model of heterogeneous ignition of metal particles. *Combustion and Flame*, 88(1):113–118, 1992.

[40] V. Rosenband, A. Gany, and Y. M. Timnat. A model for low temperature ignition of magnesium particles. *Combustion Science and Technology*, 105:279–294, 1995.

[41] V. Rosenband. Thermo-mechanical aspects of the heterogeneous ignition of metals. *Combustion and Flame*, 137(3):366–375, 2004.

[42] M. A. Gurevich, K. I. Lapkina, and E. S. Ozerov. *Fizika Goreniya i Vzryva*, 6(2):172, 1970.

[43] Yu. V. Frolov, P. F. Pokhil, and V. S. Logachev. Ignition and combustion of powdered aluminum in high-temperature gaseous media and in a composition of heterogeneous condensed systems. *Fizika Goreniya i Vzryva*, 8(2):213–236, 1972.

[44] M. A. Gurevich, E. S. Ozerov, and A. A. Yurinov. Effect of an oxide film on the inflammation characteristics of aluminum. *Fizika Goreniya i Vzryva*, 14(4):50–55, 1978.

[45] M. A. Trunov, M. Schoenitz, and E. L. Dreizin. Effect of polymorphic phase transformations in alumina layer on ignition of aluminum particles. *Combustion Theory and Modelling*, 10(4):603–623, 2006.

[46] S. D. Gilev. Electrical conductivity of metal powders under shock compression. *Combustion, Explosion and Shock Waves*, 41(5):599–609, 2005.

[47] S. D. Gilev and V. F. Anisichkin. Interaction of aluminum with detonation products. *Combustion, Explosion and Shock Waves*, 42(1):107–115, 2006.

[48] J. Crepeau. SHAMRC second-order hydrodynamic automatic mesh refinement code. Technical Report User's manual, Applied Research Associates, Inc., Albuquerque, NM, 1998.

[49] A. L. Breiter, V. M. Mal'tsev, and E. I. Popov. Models of metal ignition. *Combustion, Explosion and Shock Waves*, 13(4):475–485, 1977.

[50] G. H. Markstein. Combustion of metals. *AIAA Journal*, 1(3):550–562, 1963.

[51] H. M. Cassel and I. Liebman. Combustion of magnesium particles II - ignition temperatures and thermal conductivities of ambient gas. *Combustion and Flame*, 7:79, 1963.

[52] A. Fontijin and W. Felder. HTFFR kinetics studies of $Al + CO_2 \rightarrow AlO + CO$, a non-Arrhenius reaction. *Journal of Chemical Physics*, 67(4):1561–1569, 1977.

[53] T. A. Roberts, R. L. Burton, and H. Krier. Ignition and combustion of aluminum/magnesium alloy particles in O_2 at high pressures. *Combustion and Flame*, 92(1):125–143, 1993.

[54] S. Gordon and B. J. McBride. Computer program for calculation of complex equilibrium compositions and applications. Technical Report NASA RP-1311, NASA Lewis Research Center, Cleveland, OH, 1994.

[55] C. F. Bohren and D. R. Huffman. *Absorption and scattering of light by small particles*. Wiley, New York, 1983.

[56] D.L. Parry and M.Q. Brewster. Optical constants of Al_2O_3 smoke in propellant flames. *Journal of Thermophysics and Heat Transfer*, 5:142–149, 1990.

[57] T. Bazyn. *Spectroscopic Measurements of the Combustion of Aluminum and Aluminum-Based Energetic Material Particles Using a Heterogeneous Shock Tube*. PhD Thesis, Univeristy of Illinois at Urbana-Champaign, Urbana, IL, 2006.

[58] P. Voinovich R. Tahir and E. Timofeev. *Solver II - Two-Dimensional, Multi-Block, Multi-Gas, Adaptive, Unstructured, Time-Dependent CFD Application for MSWindows*, 1993-2007.

[59] F. M. White. *Viscous Fluid Flow*. McGraw Hill, New York, 1974.

[60] J. P. Holman. *Heat Transfer*. McGraw Hill, New York, 1997.

[61] J. J. Lee, D. L. Frost, J. H. S. Lee, and A. Dremin. Propagation of nitromethane detonation in porous media. *Shock Waves*, 5(1):115–119, 1995.

[62] J. J. Lee, M. Brouillette, D. L. Frost, and J. H. S. Lee. Effect of diethylenetriamine sensitization on detonation of nitromethane in porous media. *Combustion and Flame*, 100(1):292–300, 1995.

[63] A. M. Milne. Detonation in heterogeneous mixtures of liquids and particles. *Shock Waves*, 10(5):351–362, 2000.

[64] L. E. Fried, W. M. Howers, and P. C. Souers. Cheetah 2.0 user's manual. Technical Report UCLR-MA-117541 Rev. 5, Lawrence Livermore National Laboratory, Livermore, CA, 1998.

[65] F. Zhang, D. L. Frost, P. A. Thibault, and S. B. Murray. Explosive dispersal of solid particles. *Shock Waves*, 10(6):431–443, 2001.

[66] V. P. Kopyshev, A. B. Medvedev, and V. V. Khrustalev. Model estimation of the viscosity of explosion products of condensed explosives. *Combustion, Explosion and Shock Waves*, 40(2):200–208, 2004.

[67] S. Bastea. Transport properties of fluid mixtures at high pressures and temperatures. application to the detonation products of HMX. In *12th Symposium (International) on Detonation*, pages 576–583, San Diego, CA, August 11-16 2002.

[68] C. F. Hansen. Thermodynamic and transport properties of high-temperature air. Technical Report NASA-TR-R-50, 1959.

[69] V. M. Boiko, V. V. Lotov, and A. N. Papyrin. Ignition of gas suspensions of metallic powders in reflected shock waves. *Combustion Explosion and Shock Waves*, 25(2):193–199, 1989.

[70] A. K. Lokenbakh, N. A. Zaporina, A. Z. Knipele, V. V. Strod, and L. K. Lepin. Effects of heating conditions on the agglomeration of aluminum powder in air. *Combustion, Explosion and Shock Waves*, 21(1):69–77, 1985.

Appendix A

Equilibrium Calculations

A.1 Hydrogen - Oxygen Detonation

The following is the output file from NASA's CEA[54] equilibrium code for a hydrogen - oxygen detonation.

UNBURNED GAS

P1, BAR 1.0000
T1, K 300.00
H1, KJ/KG 4.47
M1, (1/n) 12.010
GAMMA1 1.4014
SON VEL1,M/SEC 539.5

BURNED GAS

P, BAR 18.648
T, K 3673.33
RHO, KG/CU M 8.8518-1
H, KJ/KG 2834.01
U, KJ/KG 727.29
G, KJ/KG -61191.3
S, KJ/(KG)(K) 17.4298

M, (1/n) 14.497
(dLV/dLP)t -1.08202
(dLV/dLT)p 2.3596
Cp, KJ/(KG)(K) 16.2840
GAMMAs 1.1288
SON VEL,M/SEC 1542.1

TRANSPORT PROPERTIES (GASES ONLY) CONDUCTIVITY IN UNITS OF MILLIWATTS/(CM)(K)

VISC,MILLIPOISE 1.1409

WITH EQUILIBRIUM REACTIONS

Cp, KJ/(KG)(K) 16.2840
CONDUCTIVITY 38.1301
PRANDTL NUMBER 0.4873

WITH FROZEN REACTIONS

Cp, KJ/(KG)(K) 3.2567
CONDUCTIVITY 5.3982
PRANDTL NUMBER 0.6883

DETONATION PARAMETERS

P/P1 18.648
T/T1 12.244
M/M1 1.2071
RHO/RHO1 1.8384
DET MACH NUMBER 5.2548
DET VEL,M/SEC 2834.9

MOLE FRACTIONS

*H 0.08019
HO2 0.00018
*H2 0.16216
H2O 0.53163
H2O2 0.00002
*O 0.03748
*OH 0.14145
*O2 0.04688

A.2 Nitromethane Detonation

The following is the output file from the Cheetah 2.0 [64] equilibrium code for a nitromethane detonation.

The C-J condition: The pressure = 11.89 GPa
The volume = 0.628 cc/g
The density = 1.591 g/cc
The energy = 1.61 kJ/cc explosive
The temperature = 3669 K
The shock velocity = 6.149 mm/us
The particle velocity = 1.667 mm/us
The speed of sound = 4.483 mm/us
Gamma = 2.690

Freezing occurred at T = 2145.0 K and relative V = 1.592
The mechanical energy of detonation = -5.637 kJ/cc
The thermal energy of detonation = -0.000 kJ/cc
The total energy of detonation = -5.637 kJ/cc

JWL Fit results:
E0 = -5.939 kJ/cc A = 249.28 GPa, B = 5.05 GPa , C = 1.29 GPa
R[1] = 4.72, R[2] = 1.11, omega = 0.38
RMS fitting error = 0.70 %

Product concentrations

Name		(mol/kg)	(mol gas/mol explosive)
h2o	Gas	2.308e+001	1.409e+000
n2	Gas	8.178e+000	4.992e-001
co	Gas	5.610e+000	3.425e-001
co2	Gas	1.996e+000	1.218e-001
ch4	Gas	4.644e-001	2.835e-002
c2h4	Gas	1.548e-001	9.446e-003
h2	Gas	1.535e-001	9.368e-003
ch2o2	Gas	3.033e-002	1.851e-003
h3n	Gas	2.440e-002	1.489e-003
ch3oh	Gas	1.405e-002	8.574e-004
no	Gas	1.486e-003	9.069e-005
ch2o	Gas	1.402e-003	8.558e-005
ch3	Gas	6.566e-005	4.008e-006
o2	Gas	3.315e-005	2.023e-006
c2h6	Gas	2.788e-005	1.702e-006
no2	Gas	1.392e-011	8.495e-013
*c	solid	7.956e+000	4.857e-001
Total Gas		3.971e+001	2.424e+000
Total Cond.		7.956e+000	4.857e-001

Appendix B

Flow Field of Detonation Products

The following expressions give the sound speed and flow velocity as a function of particle position and time in each of the five regions of Fig. 6.2.

B.1 Taylor Wave Simple Region 1

$$c = \frac{1}{2}\left[c_{CJ} - u_{CJ} + \frac{x}{t}\right] \tag{B.1}$$

$$u = \frac{1}{2}\left[u_{CJ} - c_{CJ} + \frac{x}{t}\right] \tag{B.2}$$

B.2 Taylor Wave and Expansion Non-Simple Region 2

$$c = \frac{1}{2}\left[\frac{x}{t} - \frac{x - R_c}{t - \frac{R_c}{V_{CJ}}}\right] \tag{B.3}$$

$$u = \frac{1}{2}\left[\frac{x}{t} + \frac{x - R_c}{t - \frac{R_c}{V_{CJ}}}\right] \tag{B.4}$$

B.3 Quiescent Flow Region 3

$$c = c_{CJ} - u_{CJ} \tag{B.5}$$

$$u = 0 \tag{B.6}$$

B.4 Expansion Simple Wave Region 4

$$c = \frac{1}{2}\left[c_{CJ} - u_{CJ} - \frac{x - R_c}{t - \frac{R_c}{V_{CJ}}}\right] \tag{B.7}$$

$$u = \frac{1}{2}\left[c_{CJ} - u_{CJ} + \frac{x - R_c}{t - \frac{R_c}{V_{CJ}}}\right] \tag{B.8}$$

B.5 Expansion and Reflected Expansion Non-Simple Region 5

$$c = \frac{R_c}{t - \frac{R_c}{V_{CJ}}} \tag{B.9}$$

$$c = \frac{x}{t - \frac{R_c}{V_{CJ}}} \tag{B.10}$$